



저작자표시-비영리-변경금지 2.0 대한민국

이용자는 아래의 조건을 따르는 경우에 한하여 자유롭게

- 이 저작물을 복제, 배포, 전송, 전시, 공연 및 방송할 수 있습니다.

다음과 같은 조건을 따라야 합니다:



저작자표시. 귀하는 원저작자를 표시하여야 합니다.



비영리. 귀하는 이 저작물을 영리 목적으로 이용할 수 없습니다.



변경금지. 귀하는 이 저작물을 개작, 변형 또는 가공할 수 없습니다.

- 귀하는, 이 저작물의 재이용이나 배포의 경우, 이 저작물에 적용된 이용허락조건을 명확하게 나타내어야 합니다.
- 저작권자로부터 별도의 허가를 받으면 이러한 조건들은 적용되지 않습니다.

저작권법에 따른 이용자의 권리는 위의 내용에 의하여 영향을 받지 않습니다.

이것은 [이용허락규약\(Legal Code\)](#)을 이해하기 쉽게 요약한 것입니다.

[Disclaimer](#)

Doctor of Philosophy

**Theoretical study on structural stability and ion transport
in crystalline and amorphous phases
of antiperovskite electrolyte Na₃OCl**

The Graduate School
of the University of Ulsan
Department of Physics
Pham Thi Thanh Tan Lien

**Theoretical study on structural stability and ion transport
in crystalline and amorphous phases
of antiperovskite electrolyte Na_3OCl**

Supervisor: Prof. Young-Han Shin

A Dissertation Submitted to the Graduate School of the University of Ulsan in
partial Fulfillment of the Requirements for the Degree of

Doctor of Philosophy

by

Pham Thi Thanh Tan Lien

Department of Physics

University of Ulsan, Republic of Korea

June 2023

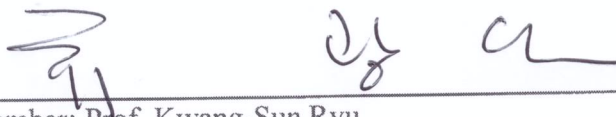
**Theoretical study on structural stability and ion transport
in crystalline and amorphous phases
of antiperovskite electrolyte Na₃OCl**

This is to declare that the dissertation
submitted by Pham Thi Thanh Tan Lien is approved officially.



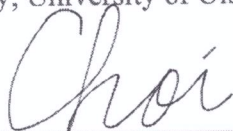
Committee Chair: Prof. Sang-Mok Choo

Department of Mathematics, University of Ulsan



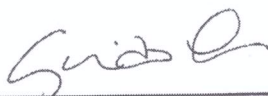
Committee Member: Prof. Kwang-Sun Ryu

Department of Chemistry, University of Ulsan



Committee Member: Dr. Wooni Choi

Innovation Center, Samsung Electronics



Committee Member: Dr. Guido Ori

Institut de Physique et Chimie des Matériaux de Strasbourg,

Université de Strasbourg, CNRS, France



Committee Member and Supervisor: Prof. Young-Han Shin

Department of Physics, University of Ulsan

Dedicated to my loving parents

Declaration

I hereby declare that except where specific reference is made to the work of others, the contents of this dissertation are original and have not been submitted in whole or in part for consideration for any other degree or qualification in this, or any other university.

Pham Thi Thanh Tan Lien

June 26, 2023

Acknowledgements

To my supervisor, friends, and family.

Abstract

The current Li-ion battery risks battery damage such as swelling caused by temperature change or leakage caused by external force since it uses a liquid electrolyte solution. There has been a resurgence of research interest in Na-ion battery chemistries in recent years because of its potential cost advantages. The main advantages of solid-state electrolytes (SSEs) are that they do not corrode, combust, leak or cause short internal circuit-like their liquid counterparts. Moreover, solid electrolytes are inert toward metallic Li and act as a separator, helping resist dendrite growth. Different classes of electrolytes with different microstructures and characteristics exhibit specific advantages, so we cannot identify whether crystalline or amorphous electrolytes are preferable to inorganic solid electrolytes. We provide an overview of structure and electrochemical properties of Na_3OCl , highlighting its unique antiperovskite structural stability and the key factors that contribute to its excellent ion transport property. The structural phase transition of the high-symmetry cubic phase of antiperovskite Na_3OCl is investigated by computing the phonon band structures of 14 different polymorphs with distinct types of ONa_6 octahedral tilting. The resulting P-T phase diagram shows that, at high temperature and low pressure, the high-symmetry cubic structure with $\text{Pm}\bar{3}\text{m}$ symmetry is the most stable phase. At low temperature and high pressure, on the other hand, the monoclinic structure with $\text{P}2_1/\text{m}$ symmetry becomes the most stable phase. The energy barriers falling in the range from 0.30 to 0.34 eV are not much different in phases. While the crystalline structure and ion dynamics of sodium oxyhalide and hydroxyhalide systems have been well-studied, the lack of precise characterization of their amorphous counterparts hinders understanding their atomic-scale properties. In this research, molecular dynamics simulations were conducted using first-principles within the Car-Parrinello scheme to investigate the structure and ion dynamics of amorphous $\text{Na}_{3-x}\text{OH}_x\text{Cl}$ ($x= 0, 0.5, 1$) antiperovskites. The results showed that the amorphous Na_3OCl structure is significantly different from its crystalline form, with limited intermediate-range order and short-range order dominated by four-fold Na atoms. However, the amorphous Na_3OCl did not show evidence of phase separation unlike previous models of glassy Li_3OCl . Remarkable Na ion dynamics and high ionic conductivity were observed in the amorphous Na_3OCl , indicating its potential as a promising SSE that rivals those of defective crystalline phases. Hydroxyl OH^- anions played a crucial role in enhancing

ion mobility and efficient transport in the amorphous $\text{Na}_{3-x}\text{OH}_x\text{Cl}$ systems. Overall, this study provides a better understanding of the interplay between structure, bonding, and ion transport in amorphous sodium-rich oxyhalide and hydroxyhalide antiperovskites, which may lead to their practical use in next-generation SSEs.

Contents

Contents	xi
List of Figures	xv
List of Tables	xxi
1 Introduction	1
1.1 Motivation	1
1.2 Brief review on perovskite- and antiperovskite-based batteries	3
1.3 The potential of antiperovskite electrolytes: a pathway towards high-performance SSE	5
1.4 The glassy state of matter	10
1.5 Experiment and modelling state of art of Li_3OCl and Na_3OCl as electrolyte material	11
1.6 Project ambition, positioning and objectives	12
2 Computational Methods and Models	15
2.1 Lattice dynamics, Gibbs free energy	15
2.1.1 Harmonic approximation	15
2.1.2 Pertubative and nonpertubative approximation	16
2.2 Density functional theory	23
2.2.1 Schrödinger equation	25
2.2.2 Born-Oppenheimer approximation	26
2.2.3 Independent electron approximation	26
2.2.4 Thomas-Fermi-Dirac approximation	28
2.2.5 Hohenberg-Kohn theorems	28
2.2.6 The Kohn-Sham Equation	29
2.2.7 The Exchange-Correlation Term	31
2.2.8 Pseudopotential method	32

2.2.9	Plane wave basis set	33
2.2.10	Total energy	34
2.3	Molecular dynamics	35
2.3.1	First principles molecular dynamics	35
2.3.2	Classical MD	37
2.4	Machine learning interatomic potentials	38
2.4.1	General overview	38
2.4.2	Gaussian Approximation Potential methodology	40
3	Structural stability and ionic transport of crystalline antiperovskite Na_3OCl	43
3.1	Introduction	43
3.2	Computational methods	46
3.2.1	Harmonic phonon calculations	46
3.2.2	Quasi-harmonic approximation	47
3.2.3	Self-consistent phonon approach	48
3.3	Result and discussion	50
3.3.1	Structural stability	50
3.3.2	Electronic structure and ionic transport properties	64
3.4	Summary	65
4	Unveiling the structure and ions dynamics of amorphous $\text{Na}_{3-x}\text{OH}_x\text{Cl}$ antiperovskite electrolytes	67
4.1	Motivation	67
4.2	Calculation methodology and models	69
4.2.1	Producing $\text{Na}_{3-x}\text{OH}_x\text{Cl}$ amorphous models at 300 K	69
4.2.2	Dynamical simulations at finite temperatures	70
4.3	Result and discussion	74
4.3.1	Structural properties	74
4.3.2	Dynamical properties	84
4.4	Summary	93
5	First quantitative assessment of the structure of amorphous antiperovskite Na_3OCl by first-principles and machine learning molecular dynamics	95
5.1	Introduction	95
5.2	Computational methodology and models	97
5.2.1	First-principles molecular dynamic simulations	97
5.2.2	DFT-FPMD database composition	98

5.2.3	MLP-GAP molecular dynamics simulations	98
5.3	Results and discussion	98
5.3.1	Machine learning interatomic potential: model fitting and training database	98
5.3.2	MLP-GAP model performance assessment: errors for testing versus training set	99
5.3.3	Total X-rays and Neutrons structure factors	102
5.3.4	Total and partial pair correlation functions	103
6	General conclusions and future perspectives	109
6.1	Conclusions	109
6.2	Future perspectives	111
	References	113
	References	113

List of Figures

2.1	Schematic representation of the temperature dependence of the square of the frequency of a soft mode. Below the temperature T_c the frequency is imaginary and hence unstable. The frequency at $T = 0$ K is the harmonic value.[54] . . .	22
2.2	Machine-learning-based interatomic potentials methodology. Top: General overview and main required components. Bottom: Three main classes of regression methods for ML potential[84]	38
2.3	Comparative flowchart of total energy calculations with traditional interatomic potentials (left) and ML interatomic potentials (right)[82]	39
3.1	(a) Phonon band structure and (b) density of states of the cubic $Pm\bar{3}m$ phase. The soft modes at M and R points in the phonon band structure indicate that the cubic $Pm\bar{3}m$ phase is dynamically unstable. The red curve in (b) represents the total phonon density of states. The black, blue and orange curves corresponds to the partial phonon density of states of Na, Cl, O, respectively. The k -path in the first Brillouin zone is shown in the inset. The unstable soft modes dominantly come from Na.	52
3.2	(a) Nontilted cubic $Pm\bar{3}m$ crystal structure is denoted by $a^0a^0a^0$. (b) M_3^+ distortion indicates in-phase rotation (the same rotation direction of octahedral layers along an axis) which is simply presented by $a^0a^0c^+$ structure. (c) The tilted $a^0a^0c^-$ system that indicates R_4^+ distortion carried by out-of-phase rotation (the alternating rotation of octahedral layers along an axis). (d) Three different views of the tilted $a^+b^-c^-$ (monoclinic $P2_1/m$) structure resulting from the combination $M_3^+ \oplus R_4^+$ distortions. (e) Energy profile of the 14 tilted structures relative to the nontilted cubic $Pm\bar{3}m$ Na_3OCl . For comparison, the energies of tilted structures are transformed into the energies per $1 \times 1 \times 1$ unit cell. All the 14 tilted structures of Na_3OCl are lower in energy than the cubic $Pm\bar{3}m$ nontilted structure where monoclinic $P2_1/m$ is the most stable structure.	54

- 3.3 (a) Phonon dispersion curves and (b) total and partial densities of states of monoclinic $P2_1/m$. The phonon dispersion curves and the total density of states show no negative modes, which proves the monoclinic $P2_1/m$ is dynamically stable. 55
- 3.4 Temperature-dependent Gibbs free energies (G_{tilts}) at pressure $P = 0$ for 14 tilted structures of Na_3OCl relative to the Gibbs free energy for cubic (G_{cubic}) Na_3OCl 57
- 3.5 Non-equilibrium Gibbs free energies $G^*(T, V, P)$ for the (a) cubic $\text{Pm}\bar{3}m$, (b) orthorhombic Bmmb , and (c) monoclinic $P2_1/m$, and (d) orthorhombic Pnma phases with respect to volume at 0 pressure and different temperatures between 0 K to 650 K are presented by blue circles with black curves fitted to the Birch-Murnaghan equation of states. From the minima of the respective black curves, the Gibbs free energies at zero pressure are obtained, and they are shown with red circles and connected with red lines. (e) The Gibbs free energy difference of the orthorhombic Bmmb , orthorhombic Pnma and monoclinic $P2_1/m$ phases were comparable to the cubic phase. (f) P - T phase diagram of Na_3OCl 58
- 3.6 (a) Phonon band structure at various temperatures from 200 K to 500 K by considering the fourth-order anharmonic contribution. (b) Temperature dependence of the squared phonon frequencies at the M and R modes. (c, d) Anharmonic phonon dispersion curves of cubic Na_3OCl calculated at 150 K and 300 K (below and above T_c) using different treatments of QP theory. The red dotted lines, green dashed lines, black dash-double-dotted lines, and blue solid lines represent the phonon bands obtained from SC1, QP[0], QP[S], and QP-NL, respectively. 60
- 3.7 (a) Helmholtz free energy curves at various temperatures from 100 to 600 K. The minimum points at each temperature curves are marked with blue squares. (b) Thermal expansion curve and lattice constant versus phase transition temperature T_C curve. (c) Temperature dependence of the squared phonon frequencies at the M and R modes when the lattice constant is obtained at energy minimum with the PBEsol functional. The data points marked with empty squares are used for line fitting. 63
- 3.8 Band gaps for 15 phases of Na_3OCl 64

- 3.9 Reaction paths for Na migration are shown with the small colored spheres in (a) cubic $Pm\bar{3}m$, (b) orthorhombic $Bmmb$, and (c) monoclinic $P2_1/m$ phases and Na, O, and Cl atoms with the larger yellow, red (inside the red octahedra), and green spheres, respectively. The relative energy changes of vacancy migration through the minimum energy path in (d) cubic $Pm\bar{3}m$, (e) orthorhombic $Bmmb$, and (f) monoclinic $P2_1/m$ phases are illustrated with colors for the corresponding reaction paths. 65
- 4.1 Temperatures along the thermal cycle for amorphous Na_3OCl : light blue line, instantaneous T values; blue line, T values sliding average with a window of 0.1 ps. The dashed vertical grey line sets the time at which optimization of the volume at $T = 300K$ and 0 GPa was implemented. Inset: final density values optimized at $T = 300K$ for the three $Na_{3-x}OH_xCl$ models. Error bars are estimated with tests at different volume performed on several final configurations (300K) to obtain a final stress tensor close 0 GPa. 71
- 4.2 Left: Total pair correlation functions for amorphous $Na_{3-x}OH_xCl$ ($x= 0$, $x=0.5$, $x=1$) obtained at $T = 300$ K. Right: Zoom-in into the 0.8-1.2 (top) and 1.8-3.2 (bottom) ranges. 75
- 4.3 Partial pair correlation functions $g_{\alpha\beta}(r)$ for amorphous $Na_{3-x}OH_xCl$ ($x= 0$, $x=0.5$, $x=1$) at $T = 300$ K relative to the pairs Na-O, Na-Cl, Na-Na, O-O, Cl-Cl, O-Cl, O-H, and Cl-H. The running integrals over the interatomic distance are shown. 77
- 4.4 a) Representation of the unit cell of crystalline Na_3OCl . The red polyhedra identify the octahedron O site. b) Crystalline supercell of 135 atoms (unit cell replicated $3 \times 3 \times 3$). c-e) Coordination units for Na, O, and Cl found in amorphous Na_3OCl at $T = 300$ K: a fourfold Na atom (O_2Cl_2) (c), a sixfold Cl atom (d), a sixfold O atom (e). f) A Na atom found in amorphous $Na_{2.5}OH_{0.5}Cl$ coordinated by at least an O atom as a hydroxyl group. Counterions interatomic bonds are identified by a dashed line with the corresponding values. We show the atoms within a radial cutoff of 3.3 Å. Color legend: Na, yellow; O, red; Cl, green; H, white. 78
- 4.5 Distributions of the structural units for Na of amorphous $Na_{3-x}OH_xCl$ ($x= 0$, $x=0.5$, $x=1$) as a function of the number of neighbors in each unit (l). Values obtained by using the definition of "total" coordination n_{ij}^t , given in Sec. 4.3.1. 79

- 4.6 MSD versus time for each element in amorphous $\text{Na}_{3-x}\text{OH}_x\text{Cl}$ ($x=0$, $x=0.5$, $x=1$) at $T=300\text{ K}$ (top) and $T=800\text{ K}$ (bottom). Colors legend: Na, yellow; O non-bonded to H atoms, red (solid line); O bonded to H atoms, red (dashed line); H, grey; Cl, green. Note that the MSD calculated at the temperatures $T=300\text{ K}$, $T=450\text{ K}$, $T=600\text{ K}$, $T=800\text{ K}$, $T=1000\text{ K}$ are reported in the ESI, (Fig. S1). 84
- 4.7 a) Rotational dynamical disorder of a given H atom (grey transparent sphere) around one O atom (red opaque sphere) of one hydroxyl OH group in amorphous $\text{Na}_{2.5}\text{OH}_{0.5}\text{Cl}$ over a time span of $\sim 30\text{ ps}$. b) Temporal evolutions of: (a) the interatomic distance between the O_1 atom of one hydroxyl group and a coordinated Na_1 atom, (b) the $\text{H}_1\text{O}_1\text{Na}_1$ angle. c-e) Proposed paddlewheel dynamics found in amorphous $\text{Na}_{2.5}\text{OH}_{0.5}\text{Cl}$ and Na_2OHCl . c) Between 0 and 5.2 ps, a sixfold coordinated O_1 atom of one hydroxyl group shows a bonding distance of 2.29 \AA with the Na atom labelled Na_1 . In between 5.2 ps and 17.5 ps, the hydroxyl OH bond is rotating with respect to Na_1 (from $\sim 150^\circ$ to $\sim 100^\circ$) while maintaining a distance $\text{O}_1\text{-Na}_1$ equal to 2.33 \AA . e) After 17.5 ps a further rotation of the OH group bringing the corresponding angle from $\sim 100^\circ$ to $\sim 25^\circ$ induces the displacement of Na_1 atom to a larger distance ($>4.5\text{ \AA}$) escaping the first coordination shell of O_1 atom. The surrounding atoms of O_1 at a distance lower than $>5\text{ \AA}$ are shown in transparent color. Dashed lines indicate the atoms coordinated within the first coordination shell of O_1 ($<3.3\text{ \AA}$). The concerted migration pathway of Na_1 atom along the $\sim 30\text{ ps}$ is shown in transparent dark yellow. As a guide, an arrow is added to indicate the direction of the pathway. Color legend: Na atoms, yellow; O atoms, red; Cl atoms, green; and H atoms, white. 85

- 4.8 For the Na_2OHCl system: proton hopping process by which H atoms migrate through a dynamical switch between σ - and hydrogen-bonds giving rise to the formation of metastable water molecules (i.e. Grotthuss-like mechanism).[226–231] a) Temporal evolution of the interatomic distance between one H atom labelled H_1 atom, belonging to a water molecule initially formed, and its bonded O atom labelled O_1 . Also shown is the temporal evolution of the distance between H_1 and a second O atom labelled O_2 that is part of a neighboring hydroxyl group. Inset: zoom-in on the temporal window along which H_1 is shared between two O_1 and O_2 , leading to the transient formation and breaking of OH bond and water molecules. b-f) Inter-unit transitions between structural units in amorphous Na_2OHCl at 300 K. Indicatively, the mean lifetimes of the transient H-bonds and water molecules are reported on top of the panels whereas the transition rates are reported between the panels. Here, the transition rate is defined as the number of inter-unit transitions per ps observed within a given process (H-bond or water molecules formation). Color legend: Na, yellow; O, red, and Cl green. 86
- 4.9 Top: Log-log plot of MSD vs time for Na in Na_3OCl at temperatures in between $T = 300$ K and 1200 K. Bottom: corresponding values of β . Inset: β value as a function of time at $T = 800$ K. 90
- 4.10 Na-ion self-diffusion coefficients (inset) and conductivities of amorphous $\text{Na}_{3-x}\text{OH}_x\text{Cl}$ ($x = 0, x=0.5, x=1$). We also report the activation energies of Na ionic conduction obtained via a linear Arrhenius fit. Closed circles correspond to FPMD data and open circles correspond to data at $T = 300$ K extrapolated by using the linear Arrhenius fit. 91
- 5.1 Top: Scatter plots of DFT-computed and GAP-predicted total energies (left), forces (centre) and virials (right) for the training and testing (insets) sets of 200 configurations in total. Bottom: Cumulative error distributions: a given point (x,y) on the curve indicates that y percent of all structures have an error equal to or below x . Insets: Absolute errors distributions of the respective quantities obtained for the training and testing sets. 101
- 5.2 Total X-rays and neutrons structure factors for glassy Na_3OCl at $T = 300$ K. The FPMD results (dark grey lines) are compared to the $S_T(k)$ in the reciprocal space (light color) or obtained through Fourier transform of the pair correlation functions with a cutoff value $k_{\text{max}} = 25$ (red lines) for the models at different sizes obtained with MLP-GAP 103

-
- 5.3 Total pair correlation function for amorphous Na_3OCl at $T = 300$ K. The FPMD results (orange black lines) are compared to the MLP calculated for GAP1 (black dashed lines) models and GAP3 (red dashed lines) mode 104
- 5.4 The partial pair correlation functions $g_{\text{NaO}}(r)$, $g_{\text{NaCl}}(r)$, $g_{\text{NaNa}}(r)$, $g_{\text{OO}}(r)$, $g_{\text{OCl}}(r)$ and $g_{\text{ClCl}}(r)$ for amorphous Na_3OCl at $T = 300$ K obtained from FPMD (fullfilled profiles) and GAP (dashed lines: black for GAP1 and red for GAP3). The curves are shifted vertically for clarity. 107

List of Tables

3.1	Cubic-to-orthorhombic phase transition temperatures are calculated by the QP theory at different levels. Two values in each cell show the transition temperatures estimated from the soft mode frequency at M and R points, respectively	63
4.1	Upper part: nearest-neighbour interatomic distances r_{ij} (in Å) identified by the position of the first maximum of the pair correlation functions $g_{ij}(r)$. We also give the first peak full width at half maximum (FWHM). For comparison, we report the values of the crystalline Na_3OCl phase obtained by experiments.[203, 225] Lower part: total and pair coordination numbers as defined by taking different cutoff radii for the definition of a total or a “cation-anion” shell of interactions (see Sec. 4.3.1). Values in parenthesis correspond to the statistical uncertainty on the last reported digits.	76
4.2	Distribution of the individual cation-anion $n_\alpha(l)$ structural units where an atom of species α (Na, Cl or O) is l -fold coordinated to a counter ion computed for glassy Na_3OCl (see definition 1, Sec. “Total and partial coordination numbers”). In bold are reported the total percentages determined for each l -fold coordination. These quantities have been calculated including neighbours separated by a cutoff corresponding to the first minimum in the $g_{\alpha\beta}(r)$. For the present work, the individual pair cutoffs used are 3.16, 3.94, 4.10, 5.06, 5.51, and 5.39 Å for, respectively, the Na-O, Na-Cl, Na-Na, O-O, Cl-Cl and O-Cl distances. A total cutoff of 3.30 Å was defined from the total $g(r)$. Error bars are given in parenthesis.	82
4.3	Na tracer diffusion coefficients (D^*), Na ions tracer (σ^*), charge (σ^σ) and total conductivities (σ^{tot}), activation energies (E_a) and Haven ratio ($H_R^{J,tot}$) extrapolated at $T = 300$ K and directly computed at $T = 800$ K on the basis of FPMD simulations. We report the values for the three $\text{Na}_{3-x}\text{OH}_x\text{Cl}$ ($x=0$, $x=0.5$, $x=1$) models.	92

5.1	Hyperparameters of the GAP Model. Note that modified values for energy, force and virial are used for a number of sets of configurations.	100
5.2	Bond lengths r_{ij} (in) in terms of position of the first maximum of the pair correlation functions $g_{ij}(r)$ and average coordination number n obtained by FPMD and MLP models GAP1 and GAP3, respectively. For completeness, we also report the values of the crystalline phase obtained by experiments or previous DFT works.	105
5.3	Distribution of the individual cation-anion $n_{\alpha}(l)$ structural units where an atom of species α (Na, Cl or O) is l -fold coordinated to a counter ion computed for glassy Na_3OCl . In bold are reported the total percentages determined for each l -fold coordination. These quantities have been calculated including neighbours separated by a cutoff corresponding to the first minimum in the $g_{\alpha\beta}(r)$. For the present work, the individual pair cutoffs used are 3.16, 3.94, 4.10, 5.06, 5.51, and 5.39 Å for, respectively, the Na-O, Na-Cl, Na-Na, O-O, Cl-Cl and O-Cl distances. A total cutoff of 3.50 Å was defined from the total $g(r)$	106

Chapter 1

Introduction

1.1 Motivation

The electrification of transportation and large-scale energy storage necessitates the development of new high-performance, low-cost batteries capable of meeting the demands of next-generation technology. Presently, commercial batteries are unable to entirely fulfill these requirements, highlighting the need for advancements in battery technology. A crucial aspect in enhancing battery performance and safety lies in the discovery, design, and optimization of solid electrolytes, which form the foundation of solid-state batteries. Traditional lithium-ion batteries, employing liquid electrolyte solutions, suffer from vulnerabilities such as swelling due to temperature changes or leakage caused by external forces. To overcome these limitations, extensive research has focused on exploring materials capable of addressing these weaknesses. The scientific community was encouraged by the successful application of inorganic solid-state electrolytes (SSEs) in batteries and their immense potential in energy-related applications. Inorganic SSEs offer inherent stability and safety features, making them an attractive avenue for replacing liquid electrolytes. Furthermore, incorporating inorganic SSEs in batteries presents an opportunity to introduce physical barriers that prevent the propagation of lithium dendrites. This enables the development of new battery chemistries, including lithium metal batteries, lithium-air systems, and lithium-sulfur systems, which possess exceptionally high energy densities.[1] The demand for batteries with high power and energy densities further underscores the necessity for advanced lithium-ion and lithium-air battery technologies. By substituting solid electrolytes for organic liquid electrolytes, future high-energy batteries have the potential to be safer. Consequently, inorganic SSEs for batteries have garnered significant attention from both the scientific and industrial communities. It is believed that these materials will play a pivotal role in transforming energy usage in the near future.[2]

Despite recognizing the advantages of non-flammable solid electrolytes their practical application faces challenges associated with poor ionic conductivities, as well as chemical and electrochemical stabilities. Despite the wide variety of inorganic materials available, finding a suitable electrolyte for solid-state batteries remains a complex task. In contrast to the rapid ion transport facilitated by solvated ions in liquid electrolytes, the behavior of ions in crystalline solids is fundamentally different. Ion diffusion in inorganic materials depends on the hopping of ions between neighboring accessible sites, which involves overcoming higher energy barriers due to geometric restrictions and electrostatic interactions. This limitation hampers effective ion conduction in the majority of inorganic materials. To address these obstacles, extensive research has been conducted over the past few decades to discover new solid electrolyte materials. The search has encompassed various systems, including crystalline, glassy, polymer, and composite materials.[3] Among the candidates, lithium- and sodium- rich antiperovskite solid electrolytes have recently emerged as highly intriguing materials for solid-state batteries. These materials exhibit strong ionic conductivity, broad electrochemical windows, stability, low cost, and structural diversity. As a result, recent developments in experimental and atomistic modeling techniques have focused on understanding and optimizing the properties of lithium- and sodium-rich antiperovskite solid electrolytes. The aim is to tune the ionic conductivity through structural manipulation.

This thesis aims to contribute to the advancement of solid-state battery technology through an exploration of recent progress in atomistic modeling techniques employed in the study of sodium-rich antiperovskite solid electrolytes. By harnessing the power of computational approaches, a comprehensive understanding of the behavior and properties of these materials can be achieved. This understanding, in turn, will facilitate the design and development of high-performance solid-state batteries. Sodium-rich antiperovskite solid electrolytes have garnered significant attention due to their unique properties, such as high ionic conductivity, wide electrochemical stability window, and cost-effectiveness. To fully exploit the potential of these materials, a comprehensive understanding of their atomic-level behavior and transport mechanisms is crucial. Atomistic modeling techniques offer a powerful tool to delve into the intricate details of sodium-rich antiperovskite solid electrolytes. By simulating the behavior of atoms and ions within the solid network, computational approaches provide insights into the underlying mechanisms governing ionic conductivity, structural stability, and electrochemical performance. Through atomistic modeling, it becomes possible to explore the effects of various factors, including material composition, defects, interfaces, and external conditions, on the overall performance of solid electrolytes. By utilizing computational approaches in this thesis, a deep understanding of the atomic-scale behavior of sodium-rich antiperovskite solid electrolytes is achieved and thoroughly discussed.

1.2 Brief review on perovskite- and antiperovskite-based batteries

Michael Faraday discovered a conduction phenomenon in lead fluoride (PbF_2) and silver sulfide in the 1830s, which is when inorganic solid-state electrolyte (SSE) research began (Ag_2S). In 1914, silver iodide (AgI), the first superionic conductor, was found to have exceptional ionic conductivity that was comparable to that of the liquid phase. [4] Fast sodium ion transportation capabilities were discovered in alumina ($\text{Na}_2\text{O} \cdot 11\text{Al}_2\text{O}_3$) in the 1960s. This material was then used to create high-temperature sodium-sulfur batteries that were employed in South Africa and Japan in the 1980s. Rechargeable batteries were popular and the subject of in-depth research at this time. Due to their strong ionic conductivity and superior electrode wetting, liquid electrolytes have been the foundation of most batteries for the past 200 years. They are vulnerable to flammability, leakage, limited electrochemical stability voltage windows, and corrosion. Due to the expanding demand for longer durability and more consistent safety from the rising electric vehicle market and grid-scale energy storage, these limitations have recently become more noticeable.

Numerous inorganic compounds with extrinsic structure flaws and good ionic conductivities have been created as a result of advancements in crystal structure engineering. These materials primarily consist of two sublattices: a sublattice of mobile ions (Li^+ or Na^+) and a backbone made of immobile ligands joined by polyhedra. Based on the primary backbone composition, there are sulfide, oxide, halide, nitride, and hydride SSEs, all of which have undergone extensive research and optimization for better ionic conductivity through composition change. It is important to note that research on these SSEs with different compositions relies on knowledge of intrinsic crystal structures, which encourages the development of high-performance electrolytes via logical design. It has been discovered that not all inorganic materials, but only a small subset of them, are capable of conducting Li^+ or Na^+ ions. The most researched materials include those that are LISICON-like (lithium superionic conductor), argyrodite, garnet, NASICON-like (sodium superionic conductor), and perovskite structures. [3, 5–9]

Antiperovskite is an inorganic material research has recently become more and more interested in a novel structural type because it exhibits a remarkable range of physical and chemical characteristics, including superconductivity, negative thermal expansion, luminescence, and catalysis.[10] Antiperovskite (A_3XY) is similar to perovskite (ABX_3) with reversed cation (A,B) and anion (X,Y) positions. More recently, excellent ionic conduction in solid compounds was introduced with the help of the structural characteristics of antiperovskites. Compounds that are antiperovskite Li_3OA ($\text{X} = \text{Cl}, \text{Br}$) have been

created and synthesized.[11] They demonstrated lithium diffusion activation energies of as little as 0.2–0.3 eV, ionic conductivities of $>10^{-3}$ S/cm at ambient temperature, and even superionic conduction of $>10^{-2}$ S/cm at temperatures above 250 °C. In contrast, the perovskite structure family's greatest lithium-ion conductivity ranged from 10^{-3} to 10^{-4} S/cm and had an activation energy of roughly 0.4 eV. The major difference results from the antiperovskite's radically different cation position from the perovskite's, which creates a unique local environment for mobile ions and alters their mobility. Actually, the body-centered cubic (bcc) packed arrangement of the anion sublattice of antiperovskites has been proposed to promote high ionic mobility in all kinds of structural families. [12]

Two key benefits of solid-state batteries over traditional Li-ion batteries are frequently cited. First, the separation of the electrodes with the solid electrolyte increases safety by preventing Li buildup, which can result in short-circuiting.[13–16] The second is the increase in energy density brought on by using a Li-metal anode.[17–20] These benefits have not yet been fully realized, and there are still several fundamental obstacles to be addressed, such as interfacial resistance, electrochemical stability, using a metal anode, and maintaining physical contact with solid particles.[21, 22] The battery technology of the 2030s, according to some, but the research challenge of the 2020s, are solid-state batteries.

Advanced lithium-ion and lithium-air battery technologies are required due to the increased demand for batteries with high power and energy densities.[1] Future high-energy batteries may be safer thanks to the potential replacement of organic liquid electrolytes with solid electrolytes. Despite the widespread recognition of the benefits of non-flammable solid electrolytes, their poor ionic conductivities and poor chemical and electrochemical stabilities hinder their usage in actual applications. Over the past few decades, there has been a continuous quest for new materials for solid electrolytes in an effort to address these issues.

Since metallic lithium anodes and lithium-based solid electrolytes have the capacity to operate well together at high voltage and deliver improved performance in terms of specific energy and power capacity, these materials are appealing for battery applications. In addition to having strong ionic conductivity, it must also meet a number of other requirements to be technologically advantageous in electrochemistry applications: In order to operate reliably over a wide temperature range, it must satisfy the following characteristics: (a) low electronic conductivity with minimal self-discharge for long shelf life; (b) large working windows in voltage and current; (c) stable operation at temperatures between 100 °C and 300 °C; (d) low leakage, low electrode corrosion, and good thermomechanical strength to allow for easy packaging with the ability to withstand harsh environments; and (e) low cost, lightweight, and low toxicity. [11]

By increasing the energy density and safety of the Li ion battery, practical development

of all-solid-state Li ion batteries employing Li metal anodes could greatly expand the applicability of electric cars. Superionic Li⁺ conductors, also known as solid-state highly conducting Li⁺ electrolytes, are currently available in a variety of good forms, some of which display conductivities that surpass those of the liquid electrolytes used in traditional Li ion batteries. Unfortunately, the power density and/or cycle life of the most recent all-solid-state Li ion battery generations are constrained. It is commonly accepted that the main reason of these restrictions is the accumulation of interfacial impedances brought on by problems with electrochemical and mechanical instability at the electrode-SSE interfaces. If multielectrolyte layers are used to prevent electrochemical or mechanical instabilities at the electrode interfaces, it is still possible that fundamental space-charge issues at ideal interfaces could still restrict either discharge or charge power density. This is especially true if these instabilities are related to electrochemistry or mechanical instability. [21, 23] There is still a lot of work being done to incorporate Li metal anodes in traditional liquid electrolyte Li ion or LiS batteries, even if all-solid-state batteries are not going to be practical in the near future. These would nevertheless, at the very least, need a thin, dense solid electrolyte separator that is Li stable and stiff enough to prevent the growth of Li dendrites during cycling.[24]

1.3 The potential of antiperovskite electrolytes: a pathway towards high-performance SSE

The discovery of Li₃OA electrolytes has impacted the field of solid-state batteries, offering exciting possibilities for the development of high-performance solid-state electrolytes. Antiperovskite structure electrolytes have emerged as a focal point of extensive research, leading to significant advancements in recent years. Impressive enhancements in ionic conductivity have been achieved, with Li-based antiperovskites reaching 2.5×10^{-2} S/cm and Na-based antiperovskites achieving 4.4×10^{-3} S/cm in various demonstrated in full cells.[25, 26] The antiperovskite structure exhibits versatile physicochemical characteristics that can be easily optimized through chemical, structural, and electrical techniques. This attribute opens up the possibility of substantial breakthroughs towards practical solid-state batteries based on antiperovskite electrolytes. However, despite the remarkable progress made thus far, antiperovskite electrolyte research is still in its early stages, and several challenges need to be addressed to further advance this field

One of the challenges is the limited understanding of structural variations within antiperovskite electrolytes. Exploring and comprehending the diverse structural aspects are essential for tailoring their properties to meet specific requirements. Additionally, the

impact of grain boundaries and their effects on overall performance remains an important area for investigation. The stability of interfaces in full-cell systems utilizing antiperovskite electrolytes is another crucial aspect that requires further understanding. To overcome these challenges and maximize the potential of antiperovskite electrolytes, it is imperative to engage in comprehensive analysis covering various aspects. This includes the fundamental structure and synthesis of antiperovskite electrolytes, as well as their performance in devices, informed by previous structural studies and recent advancements in electrolyte technology.[2]

The discovery of X_3BA antiperovskites that conduct ions can be traced back to the 1960s, when Reuter et al. described the Ag_3SI compound as a conductor of Ag^+ [27, 28]. Müller et al. [29] investigated the obtained Na_3OBr as a high-temperature Na^+ conductor, and found that it had an ionic conductivity in the range of 10^{-5} to 10^{-4} S/cm at a high temperature of 230 °C. This was the first Na^+ conducting antiperovskite structure with the standard X_3BA stoichiometry to be reported. Zhao et al.[11] devised and created the first Li^+ conducting X_3BA -type antiperovskite in 2012, which they named Li_3OCl . Due to its good Li^+ conduction under ambient conditions, Li_3OCl was used as a room-temperature Li^+ conductor. The idea for the new electrolyte was developed based on years of research on the mineral $NaMgF_3$, which has also been noted for its superionic conductivity (of the F- anion) at high temperatures. Li_3OCl (also known as $ClOLi_3$), a "electronically-inverted" antiperovskite, was created with the idea that it would enable Li^+ superionic conduction by imitating F^- conduction in $NaMgF_3$. The produced Li_3OCl and a modified version of $Li_3OCl_{0.5}Br_{0.5}$ demonstrated ionic conductivities of 0.85×10^{-3} and 1.94×10^{-3} S/cm, respectively, and at the temperature above 250 °C, it attained superionic conducting of $> 10^{-2}$ S/cm. The effective use of Li_3OA electrolyte as room-temperature ionic conductors proved the efficiency and viability of the X_3BA antiperovskite structure for ionic conduction, which launched major research efforts on the subject that have been very productive.

Before the first report of the traditional Li_3OA antiperovskites, a number of Li_3OA analogues, namely the $Li_{3-n}(OH_n)A$ ($n < 3$; $A = Cl, Br, I$) compounds, had been investigated as Li^+ conductors. $Li_{3-n}(OH_n)A$ lithium halide hydrates ($LiAH_2O$ or $Li(OH_2)A$) are an example of this series. The first order transition from orthorhombic to cubic symmetry causes the ionic conductivity of $LiBrH_2O$ to abruptly climb to 2 orders of magnitude greater when the temperature is above 33 °C. The difficulty of usually poor conductivities at room temperature persists despite significant efforts to increase the ionic conductivity of these antiperovskite structures, such as the addition of inorganic particles (e.g., Al_2O_3 , SiO_2) [30] These compounds' applicability in solid-state lithium metal batteries is further restricted by the discovery that they are unstable in contact with lithium metal and the antiperovskite $LiA-H_2O$ electrolytes have so received less focus. Another member of the

$\text{Li}_{3-n}(\text{OH}_n)\text{A}$ antiperovskite series that was created from the LiOH-LiA binary molten salts and investigated as SSEs around the same time as LiAH_2O development is the lithium halide hydroxide, or $\text{Li}_2(\text{OH})\text{A}$. $\text{Li}_2(\text{OH})\text{A}$ has a higher Li concentration than LiAH_2O because two-thirds of the Li sites are filled, while $\text{Li}_2(\text{OH})\text{A}$ still has 33% of structural Li vacancies. It is intriguing that the $\text{Li}_2(\text{OH})\text{A}$ series likewise experiences the first-order phase change that was found in the LiAH_2O system. But in $\text{Li}_2(\text{OH})\text{A}$, the transition occurs at a significantly lower temperature. Since the cubic phase is still present in $\text{Li}_2(\text{OH})\text{Br}$ even at temperatures below 50 °C, it is most likely because the crucial phase transition temperature has not been recorded for $\text{Li}_2(\text{OH})\text{Br}$. [31] On the other hand, $\text{Li}_2(\text{OH})\text{I}$ has a high transition temperature and exhibits only orthorhombic symmetry over the relevant temperature range. Because cubic $\text{Li}_2(\text{OH})\text{Cl}$ antiperovskites exhibit strong ionic conductivity above the transition temperatures, it has become a research priority to inhibit the phase transition into noncubic phases in order to preserve the high conductivity at low temperatures. [32] Common deprotonation reagents include metallic Li and butyllithium. These reagents have been used to create a number of antiperovskite compounds, including $\text{Li}_{2.17}(\text{OH}_{0.83})\text{Cl}$, $\text{Li}_{1.16}(\text{OH}_{1.84})\text{Cl}$, and $\text{Li}_{1.04}(\text{OH}_{1.96})\text{Br}$, which all have noninteger H numbers in their chemical formulas. Comparing these deprotonated samples to the comparable beginning antiperovskites with integer H values, it was found that the crucial phase transition temperatures were much lower. [31]

As a result of their simple synthesis, reasonable ionic conductivities, and low electronic conductivities (2 orders of magnitude lower than the LiAH_2O equivalent), $\text{Li}_2(\text{OH})\text{A}$ electrolytes are currently of substantial research interest. Furthermore, unlike flawless Li_3OA antiperovskites, $\text{Li}_2(\text{OH})\text{A}$ antiperovskites have intrinsic Li vacancies. With the advent of $\text{Li}_2(\text{OH})_{0.9}\text{F}_{0.1}\text{Cl}$, the ionic conductivity of the $\text{Li}_2(\text{OH})\text{A}$ series has grown to 3.5×10^{-5} S/cm at 25 °C and 1.9×10^{-3} S/cm at 100 °C. [32] It is anticipated that $\text{Li}_2(\text{OH})\text{A}$ antiperovskite electrolytes with faster ionic conduction will be synthesized via structure engineering and composition optimization, even though there is still a gap between the current conductivity and the requirements for solid-state battery application. This is because the intrinsic structural features are advantageous for doing so while the present attempts are much less than those for conventional electrolytes investigation.

It should be emphasized that the absence of intrinsic defects—which act as the charge carriers in ionic conduction—in the ideal X_3BA antiperovskite structures may be seen as a disadvantage for ionic conduction. The Li_3OCl product was actually generated as a LiCl-depleted form, as Zhao et al. showed in their initial work from 2012, proving this point. They also suggested a number of approaches, including mixing, doping, and depletion, for defect engineering in antiperovskite electrolytes. [11]

Large polyatomic units have also been used to substitute the single ions on crystallographic sites, modifying the structure of Li/Na antiperovskite electrolytes. As a matter of fact, BH_4^- is one of the well-known "superhalogens," which have been proposed to replace halogen ions due to their identical chemistry but higher electron affinity than halogens. To make perovskites for high-stability solar cells, BH_4^- and certain other superhalogens have been employed to lower the halogen concentration.[33, 34] Although the first polyatomic ion structure in Na^+ antiperovskite electrolytes was originally described in $\text{Na}_3\text{O}(\text{NO}_2)$ and $\text{Na}_3\text{O}(\text{CN})$ electrolytes about 30 years ago, the synthesis of strongly conducting $\text{Na}_3\text{O}(\text{BH}_4)$ may be a significant step forward in the development of Na^+ antiperovskite electrolytes.[29, 31] Ionic conductivities at the near level for crystalline antiperovskite electrolytes were only possible before the report of $\text{Na}_3\text{O}(\text{BH}_4)$ at very high temperatures. The electrochemical stability window and air stability, however, were not reported.

The creation of layered antiperovskite electrolytes, including $\text{Li}_7\text{O}_2\text{Br}_3$ and Na_4OI_2 , indicates that research on Li/Na antiperovskite electrolytes has expanded to include structural alteration in addition to composition change. [35, 36] Large polyatomic units have also been used to substitute the single ions on crystallographic sites, modifying the structure of Li/Na antiperovskite electrolytes. On the basis of a computer simulation, Fang et al. presented a new Li antiperovskite structure in 2017 called $\text{Li}_3\text{O}(\text{BH}_4)$, which contains BH_4^- polyatomic ions on the A-sites.[34] All of the aforementioned polyatomic ions have a charge number of -1 and were made to partially or entirely replace the A-site halogen ions in conventional X_3BA antiperovskite electrolytes. Keep in mind that this is not the only option available. In actuality, the previously stated $\text{Li}_2(\text{OH})\text{A}$ series could be viewed as modified Li_3OA antiperovskite structures with OH^- group substitutions on the B-sites. Moreover, polyatomic ions with charge number negative two, such as SO_4^{2-} and SeO_4^{2-} , could likewise replace the original B-site oxygen anions in X_3BA structures.[37] In this scenario, the initial halogen ions would enter B-sites and the massive polyatomic ions would relocate to A-sites, resulting in the inverse antiperovskite structures. An antiperovskite structure made of $\text{Na}_3(\text{SeO}_4)\text{F}_{0.5}\text{Cl}_{0.5}$ showed a low activation energy of 0.137 eV and a high Na^+ conductivity of 8.167×10^{-3} S/cm at ambient temperature. Additionally, it demonstrated reasonable air stability and a sizable electrochemical stability window (up to 4.215 V versus Na^+/Na).

In subsequent paper, M. H. Braga, J. B. Goodenough (2019 Nobel laureate in Chemistry) and colleagues described a variety of divalent-cation-doped Li_3OCl antiperovskites ($\text{Li}_{3-2x}\text{M}_x\text{OCl}$, where M is Mg, Ca, Sr, or Ba), which, when synthesized in glassy form, could provide a record-breaking ionic conductivity at the time (2.5×10^{-2} S/cm at 25 °C and 2.4×10^{-1} S/cm at 100 °C).[38, 39] It was hypothesized that the glassy sample's open structure enabled ionic hopping and contributed to its high conductivity. The ability to form

the glassy materials into dense films devoid of grain boundaries and holes is extraordinary. The high conductivity of the electrolyte sheets may also be a result of this. Additionally, it was proposed that the doping of divalent cations might produce vacancies and reduce the activation energy of Li⁺ transport. The significantly decreased activation energy of the glassy samples is the result of these alterations (e.g., 0.06 eV of Li_{2.99}Ba_{0.005}OCl compared with 0.49 eV of Li₃OCl). A substantial band gap of 4.74 eV was also visible in the predicted electronic band structure of the glassy sample, indicating a broad range of electrochemical stability. The glassy sample's electronic conductivity was 1.05×10^{-8} S/cm, which is less than the 5.5×10^{-8} S/cm of the standard LLZO electrolyte. It is thought that the decreased electronic conductivity is advantageous for dendrite-free Li plating.[40] Following the concept of a glassy electrolyte, Braga et al. created a number of doped Li- and Na-based glassy analogs and used them in both complete cells and Li-Li symmetric cells, both of which showed incredible performance. [39, 41]

Over past decade Li- and Na-rich antiperovskite solid electrolytes (SEs) have arisen to become particularly promising candidate materials for solid-state batteries on the basis of their structural flexibility, high ionic conductivity, wide electrochemical window and stability. However, attempts to reproduce the laboratory synthesis have had mixed success and the structure and ion conduction mechanism in glassy antiperovskite electrolytes is still under debate.[42, 43] Hanghofer et al. followed Braga's experiment to synthesize the Li₃OCl-based glass, but only a low ionic conductivity close to that of lithium halide hydroxides was obtained.[44] Through further investigation, they queried the existence of Li₃OCl glass and speculated that the ultra-high ionic conductivity in Li₃OCl glass was derived from the amorphous LiCl·H₂O, which was reported to have a high conductivity up to 10^{-1} S/cm. Tian et al. [45] reported the successful use of an electrolyte composite made of amorphous Li₃OCl as a matrix embedding Li_{6.75}La₃Zr_{1.75}Ta_{0.25}O₁₂ (LLZTO) garnet-type oxide particles exhibiting a high room temperature conductivity of 2.27×10^{-4} S/cm and an extremely wide electrochemical stability window up to 10 V. The amorphous Li₃OCl acting as a binder, filler and bridge promotes the formation of an integrated composite electrolyte and continuous ionic conductive network among LLZTO particles. Furthermore, the Li₃OCl with excellent affinity to lithium metal in-situ reacts with the lithium metal to form a stable and dense interfacial layer, which greatly decreases the interfacial resistance between the composite electrolyte and lithium metal.[45] Combining the garnet-type electrolyte with amorphous antiperovskites is a promising way to develop the compact garnet-type electrolyte at low temperature for solid-state lithium-ion batteries.[46]

1.4 The glassy state of matter

The investigation of amorphous and glassy antiperovskite electrolytes has garnered significant interest in recent years. In this subsection, we provide a concise overview of the main definitions that characterize the glassy state of matter from a chemical and physical perspective. This discussion is particularly relevant to understand the unique properties and behavior of disordered antiperovskite electrolytes

The nature of a material's connectivity among its constituent parts determines whether it exists in a liquid or solid state, with solids exhibiting higher connectivity compared to fluids. Non-crystalline substances, such as amorphous solids and glasses, lack the long-range atomic and molecular periodic order characteristic of crystals. However, while glasses undergo a glass transition, amorphous solids do not possess a distinct transition point.[47]

Amorphous solids are characterized by a lack of crystal structure, with their molecules or atoms arranged without long-range order. Instead, they exhibit a short-range order within their structure and in some cases a non-negligible intermediate range order. These materials are formed when a highly viscous liquid is rapidly cooled, preventing the formation of traditional crystalline lattices. Glass, specifically, is a non-crystalline solid that retains a disordered structure and exhibits a continuous transformation into a liquid state upon heating, according to Arun K. Varshneya's definition.[48] Glass possesses mechanical rigidity and elasticity, can be scratched or cracked, and appears solid on a typical observation time scale. However, it demonstrates viscous flow and gradually relaxes into a supercooled liquid state, resembling the behavior of a liquid rather than a traditional solid. Amorphous solids are isotropic, meaning they lack directional preferences in their structure. Despite their lack of long-range order, amorphous materials consist of interconnected structural blocks that can resemble the basic units found in the corresponding crystalline phase of the same compound.[49]

Understanding the unique properties and behavior of glassy materials is crucial for various scientific and technological applications. The exploration and utilization of glassy electrolytes have garnered significant interest along the years due to the possible advantages offered by their non-crystalline structure. In some cases, compared to their crystalline counterparts, glassy electrolytes exhibit enhanced structural flexibility, leading to improved performance, particularly in terms of conductivity.

1.5 Experiment and modelling state of art of Li_3OCl and Na_3OCl as electrolyte material

Crystalline Li_3OCl antiperovskite is renowned for its high ionic conductivity, reaching nearly 1 mS/cm at room temperature (RT), making it a very promising solid electrolyte. The material's remarkable conductivity is attributed to its low activation energy of 0.26 eV, which facilitates efficient ion transport.[11] While its amorphous phase has been studied by Braga et al., resulting in an enhanced ionic conductivity of 0.25 mS/cm, the energy barrier was reported to be slightly higher at 0.42 eV.[38] In modelling sign, c- Li_3OCl also attract many studies while only one work on the glass phase has been reported nanoscale phase separation of Li_2O and LiCl and formation of hydroxyl group to form $\text{Li}_x\text{OH}_{1-x}\text{Cl}$ phase. Na_3OCl sample was successfully synthesized by Hippler in 1990[50] and currently by Ahiavi in 2020 [51].

Glassy Li_3OCl - and Na_3OCl -based antiperovskites have also been reported, with a glass transition temperature between 390- 450 K and a conductivity on the order of 10^{-2} S/cm at ambient temperature. Braga and Goodenough's teams first discovered glassy Li_3OCl - and Na_3OCl -based antiperovskites in 2014, which led to the study of cation- and anion-doped X_3OA and glassy (or amorphous) antiperovskite electrolytes beyond the stoichiometric X_3OA crystalline systems.[38] However, attempts to reproduce the initial laboratory synthesis have been unsuccessful, raising questions about the structure and ion conduction mechanism of glassy antiperovskite electrolytes. Hanghofer et al. questioned Braga et al.'s initial findings, suggesting that the high conductivity of Li^+ ions was due to impurities, sample stability, and the creation of $\text{LiCl}\cdot\text{H}_2\text{O}$ resulting from the presence of H_2O .[44]

Ab initio and classical molecular dynamics simulations have provided some evidence of a subnanoscale phase separation phenomenon within Li_3OCl , resulting in the formation of distinct Li_2O and LiCl phases, as well as an intermixing phase. This subnanoscale separation has been found to play a crucial role in promoting the high conductivity of Li ions and enabling a non-zero mobility of Cl ions within the material. The creation of such subnanoscale separation was reported to enhance the overall ionic transport properties of Li_3OCl . In a similar vein, Na_3OCl has attracted significant attention in recent studies employing both experimental and computational approaches. In particular, the computational reports have proven effective in investigating the structural and dynamic properties of Na_3OCl . By employing these methods, researchers have explored various aspects of Na_3OCl crystalline phase, allowing for a comprehensive understanding of its behavior and properties

To gain a better understanding of the transport mechanisms underlying its conductivity performance, a thorough study of the atomic structure is crucial. Recent studies on the use of antiperovskites for solid-state batteries emphasized the need for quantitative structural

assessment of X_3OA systems to prevent any misunderstanding of the correlations between their structure and performance. In general, crystalline X_3OA compounds have well-understood structures and ion dynamics processes, whereas amorphous antiperovskites lack quantitative structural characterizations in both hydrogen-free and hydroxylated phases (such as oxyhalide X_3OA versus hydroxyhalide $X_{3-x}OH_xA$). The lack of understanding of Na_3OCl antiperovskite crystalline and amorphous phase structural stability hinders the analysis of material properties, highlighting the need for a project primarily focused on the structural analysis of Na-based antiperovskite Na_3OCl to clarify its structural properties and ionic transport mechanisms.

1.6 Project ambition, positioning and objectives

As outlined in the previous sections, antiperovskite materials have recently emerged as promising electrolyte candidates for solid-state batteries due to their synthetic flexibility, competing for ionic conductivity, and interesting electrochemical stability window. In particular, Li-rich and Na-rich antiperovskite electrolytes have attracted significant attention due to their potential use in high-energy-density batteries. However, the lack of understanding of their structural properties and the ongoing debate about their structure, especially regarding the amorphous phase, have hindered their development and optimization.

In this context, computational modeling has become an essential tool for understanding the complex behavior of electrolyte materials, which is critical for their successful implementation in practical applications. First, computational modeling allows the prediction of thermodynamic and kinetic properties, such as phase stability, formation energy, and reaction rates. These properties are crucial for understanding the stability and performance of the materials under different conditions and for predicting their behavior in practical applications. Furthermore, one of the main challenges for the detailed comprehension of the behaviour of antiperovskite electrolytes is the lack of experimental data on their structure. This has led to a debate about their amorphous or crystalline nature. Computational modeling can help resolve this issue by predicting the structure and properties of different antiperovskite electrolyte models and comparing them to experimental data.

In recent years, several computational approaches have been developed to model antiperovskite electrolytes, including density functional theory (DFT) and molecular dynamics (MD). These approaches have been used to study the structural, mechanical, and electrochemical properties of various antiperovskite electrolyte systems and to predict their performance in solid-state batteries.

In the following are outlined the specific scientific objectives of this Ph.D. work:

1. Structural stability, phase transition, P-T diagram, and Na ions migration energy barrier of crystalline phases of antiperovskite Na_3OCl by DFT-based calculations.
2. Unveiling the structural and ions dynamics of amorphous $\text{Na}_{3-x}\text{OH}_x\text{Cl}$ ($x = 0, 0.5, 1$) antiperovskite electrolytes by first-principles molecular dynamics.
3. Quantitative assessment of the structural properties of amorphous antiperovskite Na_3OCl electrolyte by first-principles and machine learning molecular dynamics.

Chapter 2

Computational Methods and Models

2.1 Lattice dynamics, Gibbs free energy

2.1.1 Harmonic approximation

The dynamics of interacting ions within the Born-Oppenheimer approximation are described by Hamiltonian $H = T + U$, where T is kinetic energy and U is the potential energy of system. When U is an analytic function of atomic displacements from equilibrium position $\{u\}$, it can be expanded as a Taylor series with respect to u as

$$U = U_0 + U_2 + U_3 + U_4 + \cdots + U_n + \cdots, \quad (2.1)$$

$$U_n = -\frac{1}{n!} \sum_{\{l,k,\alpha\}} \phi_{\alpha_1, \dots, \alpha_n}(l_1 k_1; \dots; l_n k_n) \times u_{\alpha_1}(l_1 k_1) \cdots u_{\alpha_n}(l_n k_n), \quad (2.2)$$

where U_n is the n th-order contribution to the potential U , l and k are unit cells and atoms indices.

In the harmonic approximation, only the quadratic potential term is considered and the Hamiltonian is given with the simplest form $H_0 = T + U_2$. The force experienced by atom k_2 in α_2 direction due to the displacement of another atom k_1 in α_1 direction can be expressed as

$$F_{\alpha_2}(l_2 k_2) = - \sum_{\{l,k,\alpha\}} \phi_{\alpha_1, \alpha_2}(l_1 k_1; l_2 k_2) \times u_{\alpha_1}(l_1 k_1) \quad (2.3)$$

The equation of motion for each atom under harmonic approximation can be written as

$$m_{k_2} \ddot{u}_{\alpha_2}(l_2 k_2, t) = - \sum_{\{l, k, \alpha\}} \phi_{\alpha_1, \alpha_2}(l_1 k_1; l_2 k_2) \times u_{\alpha_1}(l_1 k_1)$$

The solution of equation of motion has the form of superposition of traveling waves $u_{\alpha}(t) = \sum_{qj} A_{qj} \exp[i(qr - \omega t)]$ where A_{qj} is a displacement operator.

The phonon frequency ω can be obtained by constructing the dynamical matrix $D_{\alpha\beta}$

$$D_{\alpha\beta}(kk'; q) = \frac{1}{\sqrt{M_k M_{k'}}} \sum_{l'} \phi_{\alpha\beta}(0k; l'k') \exp(iqr(l')). \quad (2.4)$$

where M is the mass of atom κ and $r(l')$ is the translational vector of the l' unit cell. By diagonalizing the dynamical matrix, one obtains harmonic phonon frequencies as $D(q)e_{qj} = \omega_{qj}^2 e_{qj}$, where the index j labels the phonon modes for each crystal momentum vector q and e_{qj} is the polarization vector of the phonon mode q_j .

2.1.2 Pertubative and nonpertubative approximation

Quasiharmonic approximation

By expanding the harmonic phonon model of lattice dynamics, the quasi-harmonic approximation (QHA) describes the thermal expansions of a material. In this approximation, phonon frequencies become volume-dependent while the harmonic approximation holds for each volume.

According to standard thermodynamics, if the system is held at constant T and P , the equilibrium state is the one that minimizes the availability or non-equilibrium Gibbs energy of the crystal phase [52].

$$G(T, P) = \min_V [U_{el}(V) + F_{vib}(T, V) + PV] = \min_V [G^*(T, V, P)], \quad (2.5)$$

where $U_{el}(V)$ is the internal electronic energy from DFT calculations and $G^*(T, V, P) \equiv U_{el}(V) + F_{vib}(T, V) + PV$, and F_{vib} is the vibrational Helmholtz free energy. The Gibbs free energy is obtained from minimizing G^* with respect to volume V at given temperature T and pressure P .

The Bose-Einstein distribution gives the mean number of phonons for any frequency at a given temperature T . To derive the distribution we need to start from the partition function, Z , which is defined in its general form as[53]

$$Z = \sum_{j=1}^{\infty} \exp(-E_j/k_B T) \quad (2.6)$$

where E_j is the energy of the j -th excited state. The partition function for the phonons associated with N normal modes of a crystal (not including the zero-point motion, see below) is therefore given as

$$Z = \prod_k \left[\sum_{n_k=0}^{\infty} \exp(-n_k \varepsilon_k / k_B T) \right] \quad (2.7)$$

where the energy of an excitation, ε_k is equal to $\hbar\omega_k$ for the branch and wave vector of the k -th normal mode of the crystal, and n_k is the number of phonons excited into the k -th normal mode. By using the series $\sum_{n=0}^{\infty} \exp(-nx) = \frac{1}{1-\exp(-x)}$, the partition function can be rewrite

$$Z = \prod_k \frac{1}{1 - \exp(-\varepsilon_k / k_B T)} \quad (2.8)$$

$$\ln Z = - \sum_k \ln [1 - \exp(-\varepsilon_k / k_B T)] \quad (2.9)$$

The mean occupation number, n_k , of any state, ε_k , is obtained from the partition function by the standard result:

$$n_k = -k_B T \frac{\partial}{\partial \varepsilon_k} \ln Z = \frac{1}{\exp(\hbar\omega_k / k_B T) - 1} \quad (2.10)$$

which is Bose-Einstein distribution.

For the partition function in the complete case, we need to include the potential energy of the system, V , and the zero-point motion. The partition function becomes

$$Z = \exp(-V/k_B T) \prod_k \exp(-\varepsilon_k / 2k_B T) \quad (2.11)$$

Therefore the free vibretional energy F_{vib} is given as

$$F_{vib}(T, V) = -k_B T \ln Z = \frac{1}{2} \sum_{qj} \hbar\omega_{qj} + k_B T \sum \ln [1 - \exp(-\hbar\omega_{qj} / k_B T)]. \quad (2.12)$$

The QHA only accounts for the volume dependence of phonon frequencies and neglects higher-order anharmonicities. While the anharmonic effect is partially incorporated via the volume dependence of $\omega_q(V)$, the QHA completely neglects the intrinsic anharmonic effects which are responsible for making the temperature dependence of phonon frequencies. Nevertheless, the QH theory turns out to be a good approximation at temperatures far below

the melting point and has been employed to predict the thermal expansivity and phase boundary of various materials based on DFT. When the temperature reaches the melting point or the structure is strongly anharmonic, the QHA is less reliable. Moreover, the QHA is not valid for cases where phonon modes become unstable within the HA

Renormalized phonon theory and self-consistent phonon approach

The self-consistent phonon (SCPH) theory is one of the most successful approaches for calculating the temperature dependent phonon frequencies nonperturbatively. If we retain cubic, quartic, ..., terms in the expansion of the crystal's potential energy in powers of the displacements of the atoms from their equilibrium positions we are dealing with what is called an anharmonic crystal. In SCPH the anharmonic term is consider up to fourth order, $H = H_0 + U_3 + U_4$, where U_n is the n th-order contribution to the potential energy surface in terms of the displacement operator A . The atomic displacement $u_\alpha(lk)$ can be represented in terms of A_{qj} as follows:[54]

$$u_\alpha(lk) = (NM_k)^{-1/2} \sum_{qj} A_{qj} e_\alpha(k; qj) e^{iqr(l)} \quad (2.13)$$

where N is number of q points or the number of unit cells, $e_\alpha(k; qj)$ is displacement (polarization) vector and is a component of e_{qj}

$$\sum_k |e_\alpha(k; qj)|^2 = 1$$

$$\sum_k e_\alpha(k; qj) e_\alpha(k; -qj') = \delta_{jj'} \quad (2.14)$$

$$A_{qj} = N^{-1/2} \sum_{kl} (M_k)^{1/2} e^{-iqr(l)} e_\alpha^*(k; qj) u_\alpha(lk) \quad (2.15)$$

We then obtain n th-order potential energy represented in terms of the harmonic displacement operator A_q :

$$U_n = \frac{1}{n!} \sum_{\{q\}} \Delta(q_1 + \dots + q_n) V(q_1; \dots; q_n) \times A_{q_1} \dots A_{q_n} \quad (2.16)$$

Here and in the following, we use q for the shorthand notation of (q, j) satisfying $q = (q, j)$ and $-q = (-q, j)$. The term $\Delta(q)$ is 1 if q is a vector of the reciprocal lattice G ($q_1 + \dots + q_n = G$) and 0 otherwise. The coefficient which appear in the anharmonic Hamiltonian are the Fourier transforms of the n -th order atomic force constants.[55] $V(q_1; \dots; q_n)$ is the reciprocal

representation of the n th-order IFCs which is defined as[56]

$$V(q_1; \dots; q_n) = N^{1-n/2} \sum_{\{k, \alpha\}} (M_{k_1} \dots M_{k_n})^{-1/2} e_{\alpha_1}(k_1; q_1) \dots e_{\alpha_n}(k_n; q_n) \quad (2.17)$$

$$\times \sum_{l_2 \dots l_n} V_{\alpha_1 \dots \alpha_n}(0k_1; \dots; l_n k_n) e^{i(q_2 r(l_2) + \dots + q_n r(l_n))}.$$

The Hamiltonian of the anharmonic system in normal mode coordinates

$$H = \frac{1}{2} \sum_q \dot{A}_q \dot{A}_{-q} + \frac{1}{2} \sum_q \omega_q^2 A_q A_{-q} + \sum_{n \geq 3} \frac{1}{n!} \sum_{q_1} \dots \sum_{q_n} V_n(q_1; \dots; q_n) A_{q_1} \dots A_{q_n} \Delta(q_1 + \dots + q_n) \quad (2.18)$$

We assume the dominant terms are those with $n = 4$ (quartic term) for the soft modes theory. Moreover, we assume that the atoms undergo small oscillations, so that the anharmonic terms are small in comparison with the harmonic term. This second assumption implies that the character of the phonons does not change significantly in the presence of the anharmonic interactions, and that the only effect of the higher order terms, apart from the finite lifetime effect, is a change in frequency.

The Hamiltonian for the phonon (not include the kinetic energy $\frac{1}{2} \sum_q \dot{A}_q \dot{A}_{-q}$) then becomes:

$$H_{ph} = \frac{1}{2} \sum_q \omega_q^2 A_q A_{-q} + \frac{1}{4!} \sum_{q_1, \dots, q_4} V_4(q_1; q_2; q_3; q_4) A_{q_1} A_{q_2} A_{q_3} A_{q_4} \Delta(q_1 + q_2 + q_3 + q_4) \quad (2.19)$$

The main approximation we make is to replace a pair of normal mode coordinates by the thermal averages

$$A_{q_3} A_{q_4} \rightarrow \langle A_{q_3} A_{q_4} \rangle \quad (2.20)$$

The thermal average of a pair of normal mode coordinates is zero unless: $q_4 = -q_3$ which imposes the conservation requirement for the thermal averages:

$$\langle A_{q_3} A_{q_4} \rangle \propto \delta_{q_3 q_4} \quad (2.21)$$

In addition, we now only allow scattering processes in which two phonons scatter to form two more; we neglect terms where one phonon breaks into three or three phonons merge into one. Furthermore, we now neglect Umklapp terms. In the other words, we consider the case where $G = 0$ or $q_1 + q_2 + q_3 + q_4 = 0$

Bearing in mind the changes in the conservation requirements, the approximate Hamiltonian becomes:

$$H_{ph}^a = \frac{1}{2} \sum_q \omega_q^2 A_q A_{-q} + \frac{1}{4} \sum_q \sum_{q'} V_4(q; -q; q'; -q') \langle A_{q'} A_{-q'} \rangle A_q A_{-q} \quad (2.22)$$

It should be noted that we gain a factor of 6 in the quartic term that comes from the summation over all modes. This can be seen as arising from all allowed scattering processes of the type $(q_1, q_2) \rightarrow (q_3, q_4)$. Two phonons of wave vector q_1, q_2 scatter from each other to give two new phonons of wave vector q_3, q_4 . In our approximation we include only the wave vectors that obey the criterion $q_1 + q_2 + q_3 + q_4 = 0$ or $(q, -q) \rightarrow (q', -q')$.

$$H_{ph}^a = \frac{1}{2} \sum_q \left(\omega_q^2 + \frac{1}{2} \sum_{q'} V_4(q; -q; q'; -q') \langle A_{q'} A_{-q'} \rangle \right) A_q A_{-q} = \frac{1}{2} \sum_q \tilde{\omega}_q^2 A_q A_{-q} \quad (2.23)$$

Thermal amplitude of a normal mode coordinate $\langle A_{q'} A_{-q'} \rangle = \frac{\hbar}{\tilde{\omega}_{q'}} \left[n(\tilde{\omega}_{q'}, T) + \frac{1}{2} \right] \simeq \frac{k_B T}{\tilde{\omega}_{q'}^2}$ in the high temperature limit when $k_B T \gg \hbar \tilde{\omega}_{q'}$, since average kinetic energy, $\langle K \rangle$, of the crystal is defined $\langle K \rangle = \frac{1}{2} \sum_q \omega_q^2 \langle A_q A_{-q} \rangle$. We have the property of a harmonic oscillator $\langle K \rangle = \langle V \rangle$. Therefore the total harmonic energy of the crystal is $\langle E \rangle = \sum_q \omega_q^2 \langle A_q A_{-q} \rangle$. This is the sum over the energies of the separate modes, so that we are able to conclude that the energy of a single mode, is equal to $E_q = \omega_q^2 \langle A_q A_{-q} \rangle$. It is simply obtained that $\langle A_q A_{-q} \rangle = \frac{\hbar}{\omega_q} \left[n(\omega_q, T) + \frac{1}{2} \right]$ where $n(\omega, T) + \frac{1}{2} = \left[\exp\left(\frac{\hbar \omega_q}{k_B T}\right) - 1 \right]^{-1} + \frac{1}{2} \simeq \frac{k_B T}{\hbar \omega_q} \gg 1$

Then

$$\tilde{\omega}_q^2 = \omega_q^2 + \frac{k_B T}{2} \sum_{q'} \frac{V_4(q; -q; q'; -q')}{\tilde{\omega}_{q'}^2} \quad (2.24)$$

The set of frequencies $\tilde{\omega}_q^2$ are called the renormalized phonon frequencies and this model is called renormalized phonon theory or pseudo-harmonic approximation.

This equation has a self-consistent set of solutions for the renormalized frequencies, although in practice it is common to replace the renormalized frequencies in the denominator by their harmonic values.

It should be appreciated that the temperature dependence in this model is quite different from that due to thermal expansion, although thermal expansion is, of course, also an anharmonic effect. In general the increase of the crystal volume on heating leads to a reduction of the phonon frequencies, whereas the direct anharmonic interactions considered here lead to an increase in phonon frequencies on heating. In most cases the indirect anharmonic effects

mediated through the thermal expansion dominate, but for phase transition theory it is the direct interactions that are important. The important point to note is that we have been able to introduce temperature explicitly into the phonon frequencies.

If the coupling constants V_4 are approximately independent of temperature, the phonon frequencies vary linearly with temperature. The simple picture of a phonon frequency that varies linearly with temperature is very relevant in the standard model of displacive phase transitions. Let us consider a phonon frequency, of wave vector q , which has been renormalised by the quartic anharmonic interactions and which can simply be expressed as

$$\tilde{\omega}^2 = \omega_0^2 + \alpha T$$

where α will in general be positive.

We recall from our discussion of the calculation of harmonic frequencies that if ω_0^2 is negative the crystal is unstable against the displacements of the corresponding mode eigenvector. We now consider a symmetric high-temperature phase. If it has a harmonic frequency at any wave vector q that is imaginary, then the structure is not stable at 0 K, and there is another structure of lower symmetry that has a lower energy at 0 K. The lower energy structure can be viewed as a small modification of the higher-symmetry structure: the modification is caused by the distortion corresponding to the eigenvector of the mode with the imaginary frequency. In other words, the stable structure is equivalent to the symmetric structure with a frozen-in normal mode coordinate of wave vector q corresponding to the imaginary harmonic frequency $\omega_0(qj)$.

On warming, the anharmonic contribution to the phonon frequency increases until the renormalised frequency of $\tilde{\omega}(qj)$ becomes zero and then real. At this point the symmetric structure is now stable, and the point at which the renormalised frequency reaches zero in value corresponds to the phase transition between the low-temperature low-symmetry phase and the high-temperature symmetric phase. This gives a transition temperature, T_c , for the phase transition which is related to the fundamental parameters:[57]

This mode (in the high-temperature phase) is called a soft mode, because it has a low frequency and the crystal is essentially soft against the corresponding displacements of the atoms. The frequency is said to soften on cooling towards the transition point. Often the wave vector q is a high-symmetry point (a Brillouin zone boundary or the zone centre), but this need not always be so. Also, the transition on cooling occurs as soon as any one point on a phonon branch reaches zero. There is also a soft mode on the low-temperature side of the transition, which increases in frequency on cooling, associated with the instability that occurs on heating.

It should be noted that the anharmonic effects that drive a soft mode phase transition need not be particularly strong [58](Bruce and Cowley 1981, p 91). Rather, the soft mode harmonic

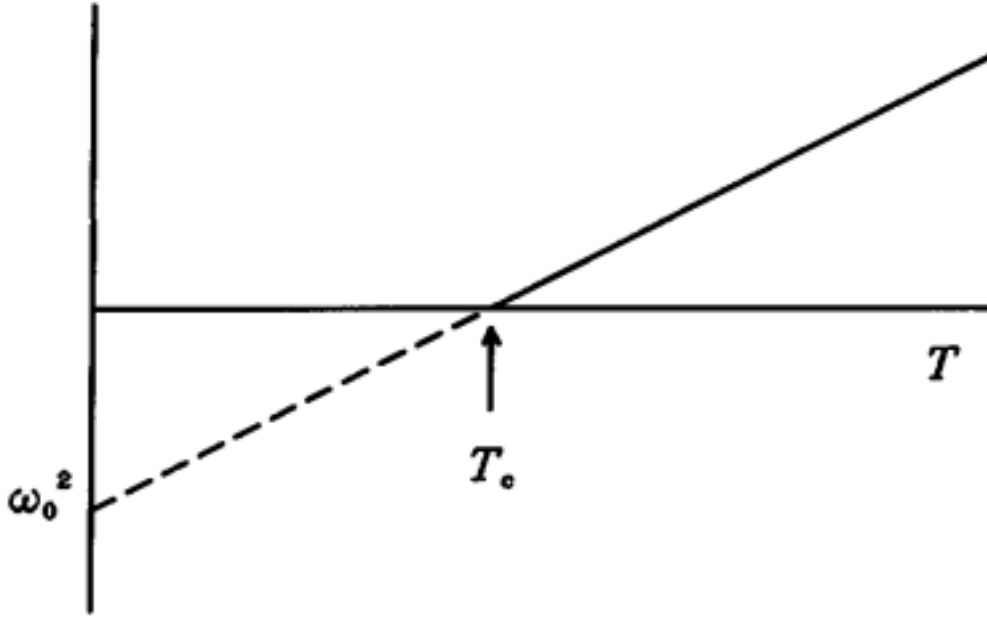


Figure 2.1: Schematic representation of the temperature dependence of the square of the frequency of a soft mode. Below the temperature T_c the frequency is imaginary and hence unstable. The frequency at $T = 0$ K is the harmonic value.[54]

frequency has a small imaginary value so that it is particularly sensitive to the effects of the anharmonic interactions.

We now consider the behavior of the soft modes. If the crystal is unstable against a small displacive distortion that can be expressed as a normal mode coordinate, the harmonic term $\tilde{\omega}_q^2 A_q A_{-q}$ must have a maximum energy when the normal mode coordinate A_q has a value of zero. This is only possible if $\tilde{\omega}_q^2 < 0$, that is, the phonon frequency $\tilde{\omega}_q$ has an imaginary value. We see from Eq. 2.24 that the anharmonic interactions increase the phonon frequency on heating if $V_4 > 0$. Thus if $\tilde{\omega}_q$ has an imaginary value at $T = 0$ K, the anharmonic interactions will make the frequency become real for temperatures greater than T_c , the temperature at which $\tilde{\omega}_q = 0$ in Eq. 2.24

$$T_c = -2\tilde{\omega}_q^2 / \left(k_B \sum_{q'} \frac{V_4(q; -q; q'; -q')}{\tilde{\omega}_{q'}^2} \right)$$

At temperatures greater than T_c the harmonic mode is stable, $\tilde{\omega}_q^2 > 0$, so the high-symmetry phase is also stable. On the other hand, at low temperatures the crystal is unstable against displacements that are described by the normal mode of label q ; we can think about the soft mode being frozen into the structure. Then the equation can be rewritten as

$$\tilde{\omega}_q^2 = \left(\frac{k_B}{2} \sum_{q'} \frac{V_4(q; -q; q'; -q')}{\tilde{\omega}_{q'}^2} \right) (T - T_c)$$

This equation yields the temperature dependence of the soft-mode frequency.

The soft-mode model is pictured schematically in Fig. 2.1, where we plot the frequency of the soft mode in the high-symmetry phase as a function of temperature. At $T = 0$ K the structure of the high-symmetry phase is unstable with respect to the distortion to the low-symmetry phase, and the frequency of the soft mode has an imaginary value. On increasing temperature the anharmonic interactions raise the value of $\tilde{\omega}_q^2$. Eventually the $\tilde{\omega}_q^2$ contribution of the anharmonic interactions is sufficiently large that the value of $\tilde{\omega}_q^2$ becomes positive, at which point the high-symmetry phase is stable. This defines the transition temperature. Experimentally the soft-mode frequency is found to fall on cooling toward the transition temperature, and it often follows the temperature dependence $\tilde{\omega}_q^2 \propto (T - T_c)$.^[54]

2.2 Density functional theory

The quantum mechanical wavefunction contains, in principle, all the information about a given system. For the case of a simple 2-D square potential or even a hydrogen atom we can solve the Schrödinger equation exactly in order to get the wavefunction of the system. We can then determine the allowed energy states of the system. Unfortunately it is impossible to solve the Schrödinger equation for a N-body system. Evidently, we must involve some approximations to render the problem soluble albeit tricky. Here we have our simplest definition of DFT: A method of obtaining an approximate solution to the Schrödinger equation of a many-body system.

DFT is a successful theory to calculate the electronic structure of atoms, molecules, and solids. Its goal is the quantitative understanding of material properties from the fundamental laws of quantum mechanics.

Traditional electronic structure methods attempt to find approximate solutions to the Schrödinger equation of N interacting electrons moving in an external, electrostatic potential (typically the Coulomb potential generated by the atomic nuclei). However, there are serious limitations of this approach: (1) the problem is highly nontrivial, even for very small numbers N and the resulting wave functions are complicated objects and (2) the computational effort grows very rapidly with increasing N, so the description of larger systems becomes prohibitive.^[59]

A different approach is taken in density-functional theory where, instead of the many-body wave function, the one-body density is used as the fundamental variable. Since the density

$\rho(\mathbf{r})$ is a function of only three spatial coordinates (rather than the $3N$ coordinates of the wave function), density-functional theory is computationally feasible even for large systems. [60]

DFT started with the theorems of Hohenberg and Kohn (1964)[61] demonstrating the equivalence of the polyelectronic wave function (complex number valued in the $6N$ -dimensional phase space for N electrons) and electronic density (real number valued in three-dimensional (3-D) ordinary space) for completely specifying the ground-state electronic structure and energy E_0 of any chemical system (N electrons moving in the electrostatic potential of P static positively charged atomic nuclei). A single distribution of electronic density in space $\rho(r)$ minimizes the total electronic energy: it is the solution of the functional equation $E_0 = \min E[\rho(r)]$. One year later, Kohn and Sham (1965)[62] proposed a practical algorithm to solve the equation, by showing that the many-bodies problem of solving the Schrödinger equation for the full polyelectronic wave function can be replaced by the much simpler one of N -independent electrons moving in an effective potential.

One-electron wave functions Ψ_i are expanded over an appropriate basis set of size M . When 3-D periodic calculations are performed on a supercell model, plane waves constitute the most convenient and popular basis set. Wave vectors are chosen so as to sample the model's Brillouin zone suitably, and some upper kinetic energy cutoff sets the highest frequencies allowed in the representation of the wave function. Convergence with respect to k -point sampling and energy cutoff must be verified in each particular instance.

Overall, the scaling property of the Kohn–Sham method is of the order N^3 and there lies the secret of its success. Indeed, the method's accuracy in energy is comparable to that of the so-called “post Hartree–Fock” approaches, like MP2, which also account for a part of the correlation energy, namely the difference between the true energy and the “Hartree–Fock limit,” or minimal energy provided by the best effort within this early approximation. However, concurrent “post-Hartree–Fock” approaches scale as N^5 or more and are thus tractable for two orders of magnitude less electrons only in the same computer. Walter Kohn was awarded the Nobel prize in chemistry in 1998 for his seminal contributions to DFT.

A further significant gain in execution time is offered with the approximation that core electrons will be only slightly perturbed by chemical combinations, so that it suffices to consider external or valence electrons exposed to the Coulombian potentials of nuclei, screened by core electrons, also called “pseudo-potentials.” The Kohn–Sham method is then applied to valence electrons represented by one-electron pseudo-wave-functions and submitted to an effective potential built from the superposition of all nuclei pseudo-potentials. This approach may reduce N by one order of magnitude.[63]

In summary, the overwhelming advantage of DFT for computational catalysis stems from its numerical scaling properties, its “chemical” accuracy, and its ability to cover in a consistent

way the whole periodic table, provided the adequate pseudo-potentials have been developed, a non-trivial task.

The book by Robert G. Parr and Yang Weitao[64] (1989) is recommended for a thorough but extensive presentation of the fundamentals of DFT.

2.2.1 Schrödinger equation

The time independent Schrödinger's equation in the Born-Oppenheimer approximation in which the electronic structure is computed at fixed nuclear positions. For a molecular system, it is:

$$\hat{H}\Psi(r_1, r_2, \dots, r_N; R_1, R_2, \dots, R_M) = E\Psi(r_1, r_2, \dots, r_N; R_1, R_2, \dots, R_M) \quad (2.25)$$

Where r_1, r_2, \dots, r_N represent the cartesian coordinates of the N electrons in the molecule, and R_1, R_2, \dots, R_M are the nuclear coordinates of the M nuclei in the molecule. The Hamiltonian operator is given by,

$$\hat{H} = \hat{T}_e + \hat{T}_n + \hat{V}_{en} + \hat{V}_{ee} + \hat{V}_{nn} \quad (2.26)$$

where the kinetic (T) and potential (V) energies of N electrons (e) and M nuclei (n) are given by,

$$\begin{aligned} \hat{T}_e &= -\frac{\hbar^2}{2m_e} \sum_{i=1}^N \nabla_i^2 \\ \hat{T}_n &= -\frac{\hbar^2}{2} \sum_{I=1}^M \frac{\nabla_I^2}{m_I} \\ \hat{V}_{en} &= -\sum_{i=1}^N \sum_{J=1}^M \frac{Z_I e^2}{4\pi\epsilon_0 |r_i - R_J|} \\ \hat{V}_{ee} &= -\sum_{i=1}^N \sum_{j>i}^N \frac{e^2}{4\pi\epsilon_0 |r_i - r_j|} \\ \hat{V}_{nn} &= -\sum_{I=1}^M \sum_{J>I}^M \frac{Z_I Z_J e^2}{4\pi\epsilon_0 |R_I - R_J|} \end{aligned} \quad (2.27)$$

Here, I and J run over the M nuclei while i and j denote the N electrons in the system. The first two terms describe the kinetic energy of the electrons and nuclei. The other three terms represent the attractive electrostatic interaction between the nuclei and the electrons and repulsive potential due to the electron-electron and nucleus-nucleus repulsive interactions, respectively. To simplify the many body Hamiltonian, all equations in the remaining thesis will be expressed by introducing the Hartree atomic units, whereby $\hbar = e = m_e = 4\pi\epsilon_0 = 1$.

If we were able to solve Eq. 2.26 and find the eigenstate with the lowest energy, which is called the ground state of the system. The complication of the solution of the equation rises exponentially with the size of a system, and therefore, appropriate approximations are required [62] [giustino 2014]

2.2.2 Born-Oppenheimer approximation

Due to their masses the nuclei move much slower than the electrons so the nuclei can be considered fixed when calculating the electron dynamics. Therefore the nuclear kinetic energy is zero and their potential energy is merely a constant. Consequently the electronic problem can be solved separately. [65] When we consider the movement of electrons the total wavefunction can be written as:

$$\Psi(\{r_i\}, \{R_I\}) = \Theta(\{R_I\}) \Psi(\{r_i\}; \{R_I\}) \quad (2.28)$$

where $\Theta(\{R_I\})$ describes the nuclei and $\Psi(\{r_i\}; \{R_I\})$ denotes the electrons (depending parametrically on the positions of the nuclei). With the BO approximation, Eq. (4) can be divided into two separate Schrödinger equations

$$[\hat{T}_e + \hat{V}_{en} + \hat{V}_{ee}] \Phi(\{r_i\}; \{R_I\}) = V(\{R_I\}) \Psi(\{r_i\}; \{R_I\}) \quad (2.29)$$

and

$$[\hat{T}_n + \hat{V}_{nn} + V(\{R_I\})] \Theta(\{R_I\}) = E_R \Theta(\{R_I\}) \quad (2.30)$$

Eq. (5) is the equation for the electronic problem with the nuclei positions fixed. The eigenvalue of the energy $V(\{R_I\})$ depends parametrically on the positions of the nuclei. After solving Eq. 2.29, $V(\{R_I\})$ is known and by applying it to Eq. 2.30, which has no electronic degrees of freedom, the motion of the nuclei is obtained. Eq. 2.30 is sometimes replaced by a Newton equation, i.e., to move the nuclei classically, using ∇V as the forces. Then the whole problem is solved.

The significance of the BO approximation or adiabatic approximation is to separate the movement of electrons and nuclei. Now we can consider that the electrons are moving in a static external potential $V_{ext}(r)$ formed by the nuclei, which is the starting point of DFT.

2.2.3 Independent electron approximation

Calculations within the independent-electron approximation are often a prerequisite for those which include correlation effects. The assumption of independently moving electrons implies

that the total wavefunction of the N- electron system $\Psi(r_1, r_2, \dots, r_N)$ can be written in the form of an antisymmetrized product of single-electron wavefunctions. The objective of the Hartree-Fock method is to produce the best possible one-electron wavefunctions for use in approximating the exact wavefunction for a multi-electron system, which can be an atom or a molecule.[66]

The simplest approximation is the Hartree approximation. The initial ansatz is that we may write the many-body wavefunction as $\Psi(r_1, r_2, \dots, r_N) = \Psi(r_1)\Psi(r_2)\dots\Psi(r_N)$ from which it follows that the electrons are independent, and interact only via the mean-field Coulomb potential. This yields one-electron Schrödinger equations of the form

$$-\frac{\nabla^2}{2}\Psi_i(r) + V(r)\Psi_i(r) = \varepsilon_i\Psi_i(r) \quad (2.31)$$

where $V(r)$ is the potential in which the electron moves; this includes both the nuclear-electron interaction and the mean field arising from the N-1 other electrons. Although these Hartree equations are numerically tractable via the self-consistent field method, it is unsurprising that such a crude approximation fails to capture elements of the essential physics. The Pauli exclusion principle demands that the many-body wavefunction be antisymmetric with respect to interchange of any two electron coordinates $\Psi(r_1, r_2, \dots, r_N) = -\Psi(r_1, r_2, \dots, r_N)$ which clearly cannot be satisfied by a non-trivial wavefunction of the form of Hartree approximation. This exchange condition can be satisfied by forming a Slater determinant of single-particle orbitals

$$\Psi(r_1, r_2, \dots, r_N) = \frac{1}{\sqrt{N}} \det\{\Psi(r_1, r_2, \dots, r_N)\} \quad (2.32)$$

Again, this decouples the electrons, leading to the single-particle Hartree-Fock equations

$$[\hat{T}_e + \hat{V}_{en} + \hat{V}_{ee}]\Psi_i(r) - \sum_j \int dr' \frac{\Psi_j^*(r')\Psi_i^*(r')\Psi_i(r)}{|r-r'|} = \varepsilon_i\Psi_i(r) \quad (2.33)$$

The last term on the left-hand side is the exchange term; this looks similar to the direct Coulomb term, but for the exchanged indices. It is a manifestation of the Pauli exclusion principle, and acts so as to separate electrons of the same spin; the consequent depletion of the charge density in the immediate vicinity of a given electron due to this effect is called the exchange hole. The exchange term adds considerably to the complexity of these equations.

The Hartree-Fock equations deal with exchange exactly; however, the equations neglect more detailed correlations due to many-body interactions. The effects of electronic correlations are not negligible; indeed the failure of Hartree-Fock theory to successfully incorporate correlation leads to one of its most celebrated failures: its prediction that jellium is

an insulating rather than a metallic system. The requirement for a computationally practicable scheme that successfully incorporates the effects of both exchange and correlation leads us to consider the conceptually disarmingly simple and elegant density functional theory

2.2.4 Thomas-Fermi-Dirac approximation

The predecessor to DFT was the Thomas-Fermi (TF) model proposed by Thomas and Fermi in 1927.[67] In this method, they used the electron density $\rho(\mathbf{r})$ as the basic variable instead of the wavefunction.

In quantum mechanics, and in particular quantum chemistry, the electronic density is a measure of the probability of an electron occupying an infinitesimal element of space surrounding any given point. It is a scalar quantity depending upon three spatial variables. The electronic density corresponding to a normalized N -electron wave function (with \mathbf{r} and s denoting spatial and spin variables respectively) is defined as

$$\rho(\mathbf{r}) = N \sum_{s_1} \dots \sum_{s_N} \int dr_2 \dots \int dr_N |\Psi(\mathbf{r}_1, s_1, \mathbf{r}_2, s_2, \dots, \mathbf{r}_N, s_N)|^2 = \langle \Psi | \hat{\rho}(\mathbf{r}) | \Psi \rangle \quad (2.34)$$

where the operator corresponding to the density observable is

$$\hat{\rho}(\mathbf{r}) = \sum_{i=1}^N \sum_{s_i} \delta(\mathbf{r} - \mathbf{r}_i) \quad (2.35)$$

The total energy of a system in an external potential $V_{ext}(r)$ is written as a functional of the electron density $\rho(\mathbf{r})$ as:

2.2.5 Hohenberg-Kohn theorems

Theorem I: The ground state particle density $\rho(\mathbf{r})$ of a system of interacting particles in an external potential $V_{ext}(r)$ uniquely determines the external potential $V_{ext}(r)$, except for a constant.[61]

The many-body Hamiltonian H fixes the groundstate of the system under consideration, i.e. it determines the groundstate many-body wavefunction Ψ , and thus the above theorem ensures that this itself is also a unique functional of the ground state density. Consequently, the kinetic and electron-electron interaction energies will also be functionals of $\rho(\mathbf{r})$. One may therefore define the functional

$$F[\rho(\mathbf{r})] = \langle \Psi | T + V_{ee} | \Psi \rangle \quad (2.36)$$

where T is the kinetic energy operator, and V_{ee} is the electron-electron interaction operator. This functional F is a universal functional in the sense that it has the same dependence on the electron density for any system, independent of the external potential concerned. The exact density dependence of this functional is, however, unknown.

Using this functional, one may then define, for a given external potential $V(r)$ the energy functional

$$E[\rho(\mathbf{r})] = \int \rho(\mathbf{r})V_{\text{ext}}(\mathbf{r})d\mathbf{r} + F[\rho(\mathbf{r})] \quad (2.37)$$

Where $F[\rho(\mathbf{r})]$ is an unknown, but otherwise universal functional of the electron density $\rho(\mathbf{r})$ only.

Theorem 2: The groundstate energy may be obtained variationally: the density that minimises the total energy is the exact groundstate density.

2.2.6 The Kohn-Sham Equation

Although these two theorems prove the existence of a universal functional, they do not give any idea as to the nature of the functional, or how to actually calculate the groundstate density. In order to do so, we must discuss the Kohn-Sham formulation. This is based upon a sleight of hand whereby we map the fully interacting system of N -electrons onto a fictitious auxiliary system of N non-interacting electrons moving within an effective Kohn-Sham potential, $V_{\text{KS}}(\mathbf{r})$, thereby coupling the electrons.[68] The single-particle Kohn-Sham orbitals are constrained to yield the same groundstate density as that of the fully-interacting system, so the Hohenberg-Kohn-Sham theorems are still valid.[62, 64]

Variation of the total energy functional with respect to the electron density, subject to the constraint of fixed particle number, i.e.

$$\int \rho(\mathbf{r})d\mathbf{r} = N \quad (2.38)$$

yields

$$\delta \left[F[\rho(\mathbf{r})] + \int V_{\text{ext}}(\mathbf{r})\rho(\mathbf{r})d\mathbf{r} - \mu \left(\int \rho(\mathbf{r})d\mathbf{r} - N \right) \right] = 0, \quad (2.39)$$

where μ is a Lagrange multiplier associated with our constraint. The Euler-Lagrange equation associated with minimisation of this functional is then

$$\mu = \frac{\delta F[\rho(\mathbf{r})]}{\delta \rho(\mathbf{r})} + V_{\text{ext}}(\mathbf{r}), \quad (2.40)$$

The Kohn-Sham formulation allows us to write the universal functional $F[\rho(\mathbf{r})]$ as

$$F[\rho(\mathbf{r})] = T_S[\rho(\mathbf{r})] + E_H[\rho(\mathbf{r})] + E_{XC}[\rho(\mathbf{r})], \quad (2.41)$$

The first two of which are known exactly and constitute the majority of the energy, the third being a small unknown quantity,

$T_S[\rho(\mathbf{r})]$ is the kinetic energy, which may be written in terms of the non-interacting single-particle orbitals, not the kinetic energy of the actual physical system under consideration.

$$T_S[\rho(\mathbf{r})] = -\frac{1}{2} \sum_{i=1}^N \int \psi^*(\mathbf{r}) \nabla^2 \psi_i(\mathbf{r}) d\mathbf{r}. \quad (2.42)$$

$E_H[\rho(\mathbf{r})]$ is the classical Hartree energy of the electrons

$$E_H[\rho(\mathbf{r})] = \frac{1}{2} \iint \frac{\rho(\mathbf{r})\rho(\mathbf{r}')}{|\mathbf{r} - \mathbf{r}'|} d\mathbf{r}d\mathbf{r}', \quad (2.43)$$

Thus the Euler-Lagrange Eq. 2.40 becomes

$$\mu = \frac{\delta T_S[\rho(\mathbf{r})]}{\delta \rho(\mathbf{r})} + V_{KS}(\mathbf{r}), \quad (2.44)$$

where $v_{KS}(\mathbf{r})$ is the effective Kohn-Sham potential is expressed as

$$V_{KS}(\mathbf{r}) = V_{\text{ext}}(\mathbf{r}) + V_H(\mathbf{r}) + V_{XC}(\mathbf{r}), \quad (2.45)$$

The Hartree potential $v_H(\mathbf{r})$ is given by

$$V_H(\mathbf{r}) = \frac{\delta E_H[\rho(\mathbf{r})]}{\delta \rho(\mathbf{r})} = \int \frac{\rho(\mathbf{r}')}{|\mathbf{r} - \mathbf{r}'|} d\mathbf{r}', \quad (2.46)$$

with the exchange-correlation potential $v_{xc}(\mathbf{r})$ and V_{ext} are defined as

$$V_{XC}(\mathbf{r}) = \frac{\delta E_{XC}[\rho(\mathbf{r})]}{\delta \rho(\mathbf{r})}. \quad (2.47)$$

$$V_{\text{ext}} = \frac{\delta E_{\text{ext}}}{\delta \rho(\mathbf{r})} = - \sum_{I=1}^M \frac{Z_I}{|\mathbf{r}_i - \mathbf{R}_I|} \quad (2.48)$$

The Euler-Lagrange equation is now of exactly the same form as that which leads to the Hartree equations. Therefore we are required to solve the Schrödinger-type equations. The density obtained when solving the alternative non-interacting Kohn-Sham system is the same as the exact groundstate density. The groundstate density is obtained in practice by solving the N one-electron Schrödinger equations,

$$\left[-\frac{1}{2}\nabla^2 + V_{\text{KS}}(\mathbf{r}) \right] \psi_i(\mathbf{r}) = \varepsilon_i \psi_i(\mathbf{r}), \quad (2.49)$$

where the ε_i correspond to the eigenvalues of the single-particle states and the charge density $\rho(\mathbf{r})$ is constructed from the Kohn-Sham orbitals as

$$\rho(\mathbf{r}) = \sum_{i=1}^N |\psi_i(\mathbf{r})|^2 \quad (2.50)$$

Similarly, the many-electron wavefunction of the system may be constructed as a Slater determinant of the Kohn-Sham orbitals

2.2.7 The Exchange-Correlation Term

The Kohn-Sham equations are thus far exact: no approximations have yet been made; we have simply mapped the fully interacting system onto an auxiliary non-interacting system that yields the same groundstate density. An approximation is introduced in defining the Exchange-Correlation energy. An implicit definition of $E_{\text{XC}}[\rho(\mathbf{r})]$ can be given through the Kohn-Sham kinetic energy as

$$E_{\text{XC}}[\rho(\mathbf{r})] = T[\rho(\mathbf{r})] - T_{\text{S}}[\rho(\mathbf{r})] + E_{\text{ee}}[\rho(\mathbf{r})] - E_{\text{H}}[\rho(\mathbf{r})], \quad (2.51)$$

where $T_{\text{S}}[\rho(\mathbf{r})]$ and $E_{\text{ee}}[\rho(\mathbf{r})]$ are the exact kinetic and electron-electron interaction energies respectively. Physically, this term can be interpreted as containing the contributions of detailed correlation and exchange to the system energy. However, the actual form of E_{xc} is not known; thus we must introduce approximate functionals based upon the electron density to describe this term. There are two common approximations (in various forms) in use: the local density approximation (LDA)[69, 70], and the generalised gradient approximation (GGA)[71]

Local Density Approximation (LDA)

This assumes that the exchange-correlation energy at a point \mathbf{r} is simply equal to the exchange-correlation energy of a uniform electron gas that has the same density at the point \mathbf{r} . Thus we can write

$$E_{\text{XC}}^{\text{LDA}}[\rho(\mathbf{r})] = \int d\mathbf{r} \varepsilon_{\text{XC}}^{\text{hom}}(\mathbf{r}) \rho(\mathbf{r}),$$

The quantity $\varepsilon_{\text{XC}}^{\text{hom}}(\mathbf{r}) \rho(\mathbf{r})$ can be further split into exchange and correlation contributions

$$\varepsilon_{\text{XC}}^{\text{hom}}(\bar{\rho}) = \varepsilon_{\text{X}}(\bar{\rho}) + \varepsilon_{\text{C}}(\bar{\rho}),$$

The exchange part, $\epsilon_X(\bar{\rho})$, which represents the exchange energy of an electron in a uniform electron gas of a particular density, was originally derived by Bloch and Dirac in the late 1920's

$$\epsilon_{XC}^{\text{hom}}(\bar{\rho}) = -\frac{3}{4} \left[\frac{3\bar{\rho}}{\pi} \right]^{\frac{1}{3}}$$

Generalised Gradient Approximation (GGA)

the LDA neglects the inhomogeneities of the real charge density. The development of various generalized-gradient approximations (GGAs) which include density gradient corrections and higher spatial derivatives of the electron density and give better results than LDA in many cases.

$$E_{XC}^{\text{GGA}}[\rho(r)] = \int dr \epsilon_{XC}^{\text{hom}}(r) \rho(r) F_{xc}[\rho(r), \nabla\rho(r)]$$

Unlike the LDA, there is no unique form for the GGA, and indeed many possible variations are possible [72–75], each corresponding to a different enhancement factor.

However GGA sometimes overcorrects LDA results in ionic crystals where the lattice constants from LDA calculations fit well with experimental data but GGA will overestimate it. Nevertheless, both LDA and GGA perform badly in materials where the electrons tend to be localized and strongly correlated such as transition metal oxides and rare-earth elements and compounds. This drawback leads to approximations beyond LDA and GGA

2.2.8 Pseudopotential method

It is well known that most physical properties of solids are dependent on the valence electrons to a much greater degree than that of the tightly bound core electrons. It is for this reason that the pseudopotential approximation is introduced. This approximation uses this fact to remove the core electrons and the strong nuclear potential and replace them with a weaker pseudopotential which acts on a set of pseudo wavefunctions rather than the true valence wavefunctions. In fact, the pseudopotential can be optimised so that, in practice, it is even weaker than the frozen core potential [76]

Pseudopotentials are often used in conjunction with plane wave basis sets. It takes a very large number of plane waves to expand the wave functions of core electrons because they are highly oscillatory near nuclei. Pseudopotentials essentially replace the core electrons and true potential (Z/r) with a smoother, effective potential that produces atomic, valence electron wave functions with less oscillatory behavior while preserving the key features of the all-electron,

atomic, valence electron wave functions such as their eigenvalues, values outside the cutoff radius (which separates the core and valence region), etc

The pseudopotential is constructed in such a way that there are no radial nodes in the pseudo wavefunction in the core region and that the pseudo wavefunctions and pseudopotential are identical to the all electron wavefunction and potential outside a radius cut-off r_c . This condition has to be carefully checked for as it is possible for the pseudopotential to introduce new non-physical states (so called ghost states) into the calculation.[77]

2.2.9 Plane wave basis set

Once the exchange and correlation functional is fixed, the KS equation could be solved. The first step toward the numerical solution of KS Eq. 2.49 is to choose a basis set to expand the electron wave functions. In the case where the periodic boundary conditions (PBC) are used, often one uses a plane wave (PW) basis set, which is widely applied for the treatment of many condensed matter systems. Due to the periodicity of the potential, the KS eigenstates become Bloch functions and the single particle orbitals can be expanded as PW's. Using the Bloch theorem, the periodic wave functions of the systems could be written:

$$\psi_i^k(\mathbf{r}) = e^{i\mathbf{k}\mathbf{r}} \varphi_i^k(\mathbf{r})$$

where ψ is the wave function of the periodic system, k is the reciprocal space vector and φ is a function with the same periodicity as the system. Since φ is an arbitrary function, we could expand it as a PW's using Fourier series:

$$\varphi_i^k(\mathbf{r}) = \sum_G C_i^k(\mathbf{G}) e^{i\mathbf{G}\mathbf{r}}$$

where k \mathbf{k} is a continuous wave vector that is confined to the first Brillouin zone of the reciprocal lattice. The wave function reads:

$$\psi_i^k(\mathbf{r}) = \sum_G C_i^k(\mathbf{G}) e^{i(\mathbf{k}+\mathbf{G})\mathbf{r}}$$

Where C_i^k is the Fourier coefficient or the plane-wave coefficients and G is a reciprocal space vector defined by $\mathbf{G}\cdot\mathbf{R}=2\pi m$, where m is an integer, \mathbf{R} are crystal lattice vectors. The above results show that the electron wave functions can be expanded in terms of a linear combination of plane-waves,

The number of G vectors can be tuned by making sure that the convergence of some basic properties is reached and considering only Fourier components corresponding to energies less

than a cut off energy $E_{cut} = \frac{1}{2}(k + G)^2$. The choice of this cutoff energy depends on the studied system as well as the pseudopotential used and determines the accuracy of the DFT energy.

It is possible also to further simplify equation [1.30] by reducing the summation over k , for instance by including only the Γ ($k=(0,0,0)$) point. Such a choice is suitable for isolated systems and in general for cases in which the dispersion of the band structure can be safely approximated with a straight line. This is of course inaccurate for metals unless a very large unit cell is employed. Finally the wave function is given by:

$$\psi_i(\mathbf{r}) = \sum_{\mathbf{G}} C_i(\mathbf{G}) e^{i\mathbf{G}\mathbf{r}}$$

Plane waves are not explicitly dependent on the atomic coordinates. In addition, the accuracy of the basis set could be simply improved by increasing the number of the Fourier components used. However, as stated previously, the choice of E_{cut} is always crucial. The number of the plane waves for a given E_{cut} depends on the cell volume (Ω) and the K -points used. An estimation of the number of plane waves corresponding to a given cutoff is given by:

$$N_{PW} = \frac{1}{2\pi^2} \Omega E_{cut}^{\frac{3}{2}}$$

2.2.10 Total energy

The total energy derived from density functional theory in the framework of the plane waves basis set and the pseudopotential approximation could be derived from Eq. 2.39 by substituting the potential expression by the pseudopotential contribution of the local and non-local parts:

$$E^{KS}[\rho(\mathbf{r})] = \sum_i \int \psi_i^*(\mathbf{r}) \left(-\frac{1}{2} \nabla^2 + V_{nloc}^{PS} \right) \psi_i(\mathbf{r}) d\mathbf{r} + E_H[\rho(\mathbf{r})] + E_{xc}[\rho(\mathbf{r})] + E_{ion}^{loc} + \sum_{J>I}^M \frac{Z_I Z_J}{|\mathbf{R}_I - \mathbf{R}_J|}$$

where $T_s[\rho(\mathbf{r})] = \sum_i \int \psi_i^*(\mathbf{r}) \left(-\frac{1}{2} \nabla^2 + V_{nloc}^{PS} \right) \psi_i(\mathbf{r}) d\mathbf{r}$, and $E_{ext} = E_{ion}^{loc} + \sum_{J>I}^M \frac{Z_I Z_J}{|\mathbf{R}_I - \mathbf{R}_J|}$ where $E_{ion}^{loc} = \int V_{loc}^{PS} \rho(\mathbf{r}) d\mathbf{r}$

The associated Schrödinger like equation is given by:

$$\left(-\frac{1}{2} \nabla^2 + V_{nloc} + V_{eff}(r) \right) \psi_i(\mathbf{r}) = \epsilon_i \psi_i(\mathbf{r})$$

The new effective potential reads:

$$V_{eff}(r) = V_H(r) + V_{XC}(r) + V_{ion}^{loc} + V_{ext}(r)$$

2.3 Molecular dynamics

2.3.1 First principles molecular dynamics

Molecular dynamics (MD) method, a numerical simulation technique where the temporal evolution of a set of interacting particles is followed by integrating their equations of motion, can be combined with DFT to realistically describe complex system. This method is named as first principles molecular dynamics (FPMD) simulations (also referred to as *ab initio* MD (AIMD) in literature). The interaction between atoms in FPMD approach is computed directly from the DFT total energy. As introduced in previous sections, this DFT total energy is a function of electron wavefunctions and atomic coordinates. By applying the Born-Oppenheimer (BO) approximation, the motion of electrons and nuclei are decoupled and each timestep when the nuclei move from the position $R_I(t)$ updated to $R_I(t + dt)$, the optimization of the electronic structure is performed. In other words, one can assume that the electronic fast motion can be separated from the slow nuclei one, and that the electrons adapt instantaneously to the change on the nuclear configuration. Therefore, the electrons are taken as being always in their quantum mechanical ground state. The forces acting on nuclei are calculated as the gradient of the total energy (E_T) with respect to the ionic position and the variables $R_I(t)$ update to $R_I(t + dt)$. The iterative force estimation assumes that the electronic structure is recalculated and the complete diagonalization of the Hamiltonian (H_T) is performed at each time step along the discrete trajectory $\{R_I(t)\}$

$$\begin{cases} M_I R_I = -\nabla_{R_I} E_T [\{\psi_i\} \{R_I\}], \\ H_T \psi_i(r) = \epsilon_i \psi_i(r) \end{cases} \quad (2.52)$$

In 1985, Car and Parrinello proposed an alternative way to this BO approximation scheme, which represented a real advance in FPMD simulations. FPMD involves two major problems: the integration of motion of nuclear positions and the dynamical propagation of the electronic subsystem of the ground state. This last requirement in the Car-Parrinello Molecular Dynamics (CPMD) approach is satisfied in a numerically stable way and constitutes an acceptable compromise for the time step length of the nuclear motion. The formulation is an extension of the classical molecular dynamics Lagrangian in which the wavefunctions representing the electronic degrees of freedom are added to the system with any other dynamical variable as a thermostat

$$L_{CP} = \sum_I M_I \dot{R}_I^2 + \sum_i \mu \int dr^3 |\dot{\psi}_i(r)|^2 + \frac{1}{2} \sum_k \eta_k \dot{q}_k - E_T[\rho, q_k, \{\psi_i\}, \{R_I\}] + \sum_{ij} \lambda_{ij} \left(\int dr^3 \psi_i^*(r) \psi_j(r) - \delta_{ij} \right)$$

From left to right, the different terms in the aboved equation represent respectively the kinetic energies of the nuclei, the electrons and the dynamical variables, the total energy (DFT functional) and the last term is the orthonormality constraint of the wavefunctions. At each step, the CPMD approach implements the following Euler-Lagrange equation of motion (EOM).

$$\begin{cases} \mu \ddot{\psi}_i(r) = -\frac{\delta E_T}{\delta \psi_i^*} + \sum_j \lambda_{ij} \psi_j(r), \\ M_I \ddot{R}_I = -\nabla_{R_I} E_T, \\ \eta_k \ddot{q}_k = -\frac{\partial E}{\partial q_k} \end{cases} \quad (2.53)$$

where μ is control parameter for the update rate of the wavefunctions with respect to the nuclear positions and represents the fictitious mass attributed to the orbitals $\psi_i(r)$, \ddot{R}_I the acceleration of atom I. Proper choice of the input parameter μ allows good control of adiabaticity. The EOM are implemented in a discrete finite difference method via a velocity-Verlet algorithm. [78]

The main idea of the Car-Parrinello method is to consider the electronic states $\{\psi_i\}$ as classical dynamical variables. In this context the fictitious dynamical optimization of $\{\psi_i\}$ and the real atomic dynamics are run in parallel. When the nuclei move from one configuration to another, the electronic states $\{\psi_i\}$ are automatically optimized to the new configuration. The fictitious electronic motion is governed by Eq.2.53 and similarly evolve at a "fictitious temperature" $\propto \mu \int dr^3 \dot{\psi}_i^*(r) \dot{\psi}_i(r)$. In this sense, if the fictitious electronic temperature is low enough, and if we optimize the initial configuration wave functions to its ground state, the electronic subsystem will remain close to its instantaneous minimum energy (minimum of the BO energy surface) during the dynamical evolution of the ions.[79] The total conserved CP energy is given as:

$$E = \int \mu \dot{\psi}_i^*(r) \dot{\psi}_i(r) dr + \frac{1}{2} M \dot{R}_I^2 + E_T$$

The CPMD scheme represented a significant advance in realistic simulations of real and complex materials under various thermodynamic conditions. The method is nowadays widely applied to a large variety of materials, ranging from crystalline solids to disordered systems such as liquids and glasses. Typical CPMD time scales ranges cover from tens of picoseconds.

2.3.2 Classical MD

As previously mentioned, MD method, a numerical simulation technique where the temporal evolution of a set of interacting particles is followed by integrating their equations of motion. It used the laws of classical mechanics, notably Newton's equations, which for each particle i of atom mass m_i are written as follow

$$m \frac{d^2 r_i}{dt^2} = F_i(t)$$

$$F_i(t) = -\nabla_i U(r_1, r_2, \dots, r_N)$$

$F_i(t)$ is the force acting on the particle i of mass m_i by $(N-1)$ other particles. $U(r_1, r_2, \dots, r_N)$ is the interaction potential of the N particle system. The total energy of the system is the sum of the interaction potential and the mean kinetic energy of the particles.

MD simulations are applied to systems containing many particles interacting through relatively short-range forces. Typical time scale ranges cover from femtoseconds to nanoseconds. A simulation is good from the point of view of its duration, if the latter is much greater than the relaxation time characteristics of the quantity under consideration. MD is fundamentally based on the interaction forces between particles. The method used to calculate these interaction forces, therefore, characterizes the simulation. Molecular dynamics simulation scheme is carried out by following the main steps below summarized

- Define the initial configuration of the system (positions, velocities);
- Compute the forces acting on particles as gradient of potential;
- Calculate the positions and the velocities of all particles at $t + dt$ (move particles);
- Move time forward and repeat the procedures from step 2

Classical MD has limitations when considering network-forming glasses due to the empirical or semi-empirical nature of the interatomic potentials employed in classical MD. For this class of materials, the determination of the potential energy surface requires the consideration of the electronic structure.

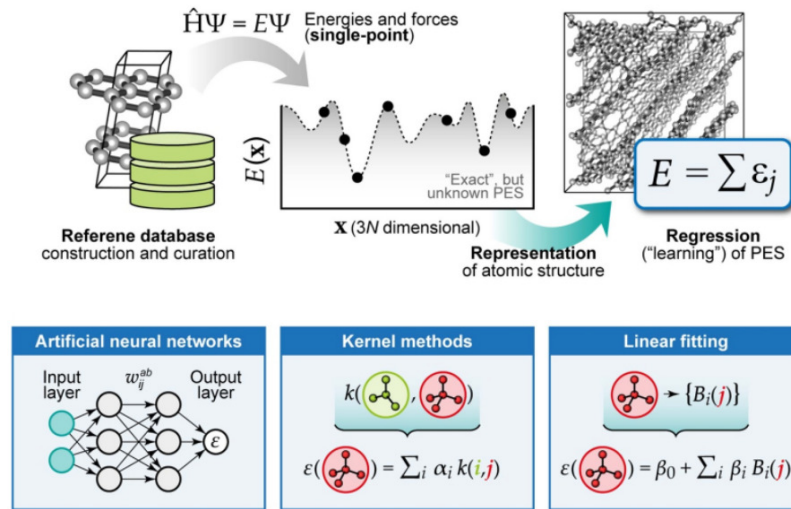


Figure 2.2: Machine-learning-based interatomic potentials methodology. Top: General overview and main required components. Bottom: Three main classes of regression methods for ML potential[84]

2.4 Machine learning interatomic potentials

2.4.1 General overview

Machine learning (ML) interatomic potentials (MLIP) are increasingly taking a relevant place in the study of material properties at the atomic scale and have a great advantage in terms of computational cost, rapidity and even accuracy [80–82]. ML potentials are a mathematical representation of 3N-dimensional potential energy surface (PES) by a set of local environment descriptors [83]. Thus, ML algorithms are used to accurately interpolate energies, forces, and pressures from a database of accurate results obtained by quantum mechanical calculations (FPMD-DFT). The correspondence between the PES and local environment descriptors is learned directly from the reference data, which gives ML potentials good accuracy and reasonable transferability within a certain degree [80]. Several ML regression techniques grouped into three classes (as shown at the bottom of Fig. 2.2) have been developed to map the local environments of the atoms onto the PES[84]. The first class, based on the artificial neural network (ANN), includes the neural network potentials (NNP) [85]. The second class consists of kernel methods among which we have the Gaussian approximation potential (GAP). And the third class refers to the methods based on linear adjustment, including the potential of the neighborhood spectral analysis (SNAP), the potential of the momentum tensor (MTP).

Figure 2.3 shows the comparative flowcharts for the traditional and ML potentials. Note that for the traditional potential, the energy of an atom i is calculated using the

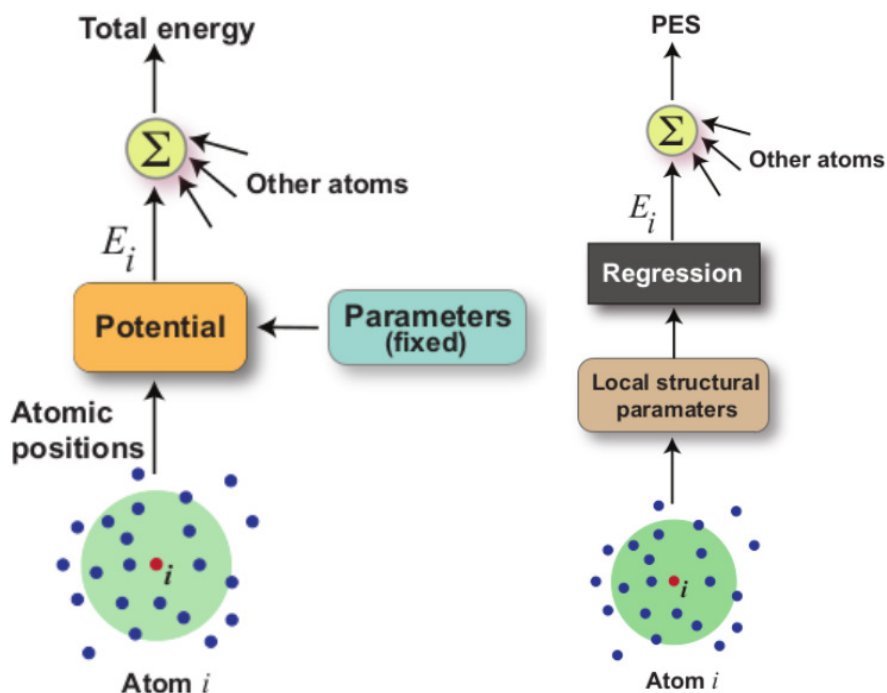


Figure 2.3: Comparative flowchart of total energy calculations with traditional interatomic potentials (left) and ML interatomic potentials (right)[82]

atomic coordinates within the cutoff sphere and the fixed values of the (empirical) potential parameters. The total energy of the system is thus obtained by summing the atomic energies of all atoms. In contrast, in the case of the MLIP, the local environment of a given atom i within the cutoff sphere is encoded in a set of local structural parameters without any prior assumptions about the functional form. An appropriate regression model allows to establish the correspondence with the energy of this atom. The sum of the atomic energies gives the total energy and thus a point on the PES of the system.

After fitting the ML potential, it can be used to predict energies and forces for large systems without the need for additional reference data. Fig. 2.2 (top) shows the three main ingredients needed to generate the ML potential, namely the reference data from the FPMD/DFT calculations (the quality of the ML model depends on the quality of its input data), the mathematical representation for atomic structure with the descriptors that must be permutational, rotational and translational invariance [83] and the regression method (kernel-based method such as GAP, linear regression, etc).

2.4.2 Gaussian Approximation Potential methodology

GAP belongs to the family of kernel-based methods. In 2010, Bartok et al introduced the GAP framework, which uses Gaussian process regression [86]. This approach is increasingly used to implement the ML potential. As mentioned at the end of the previous section, the construction of the GAP requires three ingredients.

- Database of reference configuration: This is the starting point for the ML potential. In this work, accurate energies, forces and virial stresses are computed from large DFT-FPMD dataset for glassy Na_3OCl . These data are used in appropriate format for the training and validation process of our ML potential.
- Mathematical representations for atomic structure: Having the reference data, we need to convert the atomic structure using descriptors into a suitable input form for the potential-energy surface (PES) fit. All descriptors must satisfy the symmetry requirements (invariant to translation, rotation and permutation). The Smooth Overlap of Atomic Positions (SOAP) is the many-body descriptors developed for GAP [83]. It should be confined to the local environment of the atom within a given cutoff distance.
- Regression task: This last ingredient consists in performing the PES fitting based on GAP. This is a supervised learning problem because we are dealing with labeled input data. To implement GAP, the total energy is decomposed into individual atomic contributions[80]

$$\begin{aligned} E &= \left(\delta^{2b}\right)^2 \sum_{i \in \text{pairs}} \varepsilon^{(2b)}(\mathbf{q}^{(i)}) + \left(\delta^{MB}\right)^2 \sum_{i \in \text{atoms}} \varepsilon^{(MB)}(\mathbf{q}^{(i)}) \\ &= \sum_i \varepsilon(q^{(i)}) = \sum_{ij} \beta_j K(q^{(i)}, q^{(j)}) \end{aligned}$$

where the coefficient β are determined by the ML fitting procedure, $\varepsilon(q^{(i)})$ represent the energy contribution of atom i and $K(q^{(i)}, q^{(j)})$ is the kernel function that quantify the degree of similarity between the atomic environment described by descriptors $q^{(i)}$ and $q^{(j)}$.

In 2-body descriptors, a squared exponential kernel was used

$$K^{(2b)}(\mathbf{q}^{(i)}, \mathbf{q}^{(j)}) = \exp \left[-\frac{1}{2} \sum_{\xi} \frac{(q_{\xi}^i - q_{\xi}^j)^2}{\theta_{\xi}^2} \right]$$

where j denotes one of N_t training configuration $\mathbf{q}^{(j)}$. where ξ is an index running over the components of the descriptor vector \mathbf{q} . The descriptor has one single scalar component

(namely, the distance r_{12} between the two atoms involved)

In SOAP descriptors, the local atomic density of atom i from its neighbors within a cutoff distance r_{cut}

$$\rho_i(r) = \sum_j f_{cut}(\|r_{ij}\|) \exp\left[-\frac{(r_i - r_{ij})^2}{2\sigma_{at}^2}\right]$$

where σ_{at} is a parameter that controls the smoothness of the potential, r_i the position vector of atom i and j and f_{cut} is the cutoff function define as follow:

$$f_{cut}(r_{ij}) = \frac{1}{2} + \cos\left(\frac{\pi r}{r_{cut}}\right) = f_{cut}(r_{ij}) = \frac{1}{2} + \cos\left(\frac{\pi r}{r_{cut}}\right) = \begin{cases} 1, & r < r_{cut} - d \\ \frac{1}{2} \left[1 + \cos\left(\pi \frac{r - r_{cut} + d}{d}\right)\right], & r_{cut} - d < r \leq r_{cut} \\ 0, & r > r_{cut} \end{cases}$$

Here, d is the cutoff transition width for which f_{cut} decreases smoothly to 0. The SOAP kernel is evaluated by expanding the local density $\rho_i(r)$ in a local basis set of orthogonal radial basis functions $g_n(r)$ and spherical harmonic Y_{lm} .

$$\rho_i(r) = \sum_{nlm} C_{nlm}^i g_n(r) Y_{lm}(r),$$

where C_{nlm}^i are the expansion coefficients. The descriptors are formed from these expansion coefficients by calculating the spherical power spectrum.

$$(\mathbf{q}^{(i)})_{m'l} = \frac{1}{\sqrt{2l+1}} C_{nlm}^i (C_{n'l'm}^i)^*$$

This many-body SOAP descriptors satisfy the symmetry requirements and the associated dot product kernel is defined as follow:

$$K^{MB}(\mathbf{q}^{(i)}, \mathbf{q}^{(j)}) = \left| \frac{\mathbf{q}^{(i)} \cdot \mathbf{q}^{(j)}}{|\mathbf{q}^{(i)}| \cdot |\mathbf{q}^{(j)}|} \right|^\zeta,$$

where ζ is a positive integer parameter that improve the sensitivity of the kernel and increase the body order the model and K is the kernel function that quantify the degree of similarity between the atomic environment described by descriptors [80]. There are several tools for implementing ML, and we present some of them in the next section.

Regression is used to find a function (line) that represents a set of data points as closely as possible. In statistical modeling, regression analysis is a set of statistical processes for estimating the relationships between a dependent variable (often called the 'outcome'

or 'response' variable) and one or more independent variables (often called 'predictors', 'covariates', 'explanatory variables' or 'features'). The most common form of regression analysis is linear regression, in which one finds the line (or a more complex linear combination) that most closely fits the data according to a specific mathematical criterion. A Gaussian process is a probabilistic method that gives a confidence (shaded) for the predicted function. Gaussian processes are a powerful tool in the machine learning toolbox. They allow us to make predictions about our data by incorporating prior knowledge. Their most obvious area of application is fitting a function to the data. This is called regression and is used, for example, in robotics or time series forecasting. For a given set of training points, there are potentially infinitely many functions that fit the data. Gaussian processes offer an elegant solution to this problem by assigning a probability to each of these functions.

There are several ways to interpret Gaussian process (GP) regression models. One can think of a Gaussian process as defining a distribution over functions, and inference taking place directly in the space of functions, the function-space view. Although this view is appealing it may initially be difficult to grasp, the equivalent weight-space view is discussed which may be more familiar and accessible. Deringer et al. [87] provides fundamental background and more detailed analysis on the regression process.

Chapter 3

Structural stability and ionic transport of crystalline antiperovskite Na_3OCl

3.1 Introduction

Antiperovskite materials have attracted much attention due to their applicability in various technologies. Many researches have been performed to understand the ion transport, magnetism, superconductivity of the antiperovskite materials [88–92]. These materials have interesting physical properties like giant magnetoresistance in Mn_3GaC [93], the near-zero temperature coefficient of resistivity in Mn_3NiN [89]. Especially, alkali metal oxyhalides such as Li_3OCl , Li_3OBr , Na_3OCl , and Na_3OBr have demonstrated superionic conductivity [11].

Recently, there has been growing interests in solid-state electrolytes as they can provide non-flammable, lower-maintenance batteries with a longer life cycle and a lower self-discharge [38]. Since organic liquid electrolytes used as Li transport medium in the traditional rechargeable batteries are flammable, they suffer from safety issues. During charge and discharge processes the formation and growth of anode dendrites through the electrolyte to the cathode results in short-circuit and incendiary consequences. Present-day Li ion batteries are fabricated in the discharged state to avoid any alkali metal in the anode. However, the anode of a high-voltage cell reacts with the organic-liquid electrolyte and forms a solid-electrolyte interphase (SEI) passivation layer. The solid electrolytes have energy gap large enough above the Fermi energies of metallic lithium and sodium to eliminate formation of SEI layers. Solid electrolytes also have the potential to improve battery performance since they have the potential to be utilized with elemental metals such as lithium or sodium for the anode, which would increase the energy density of the battery. Therefore, all-solid-state batteries are

emerging as suitable candidates for large-scale energy storage. Solid electrolytes have not yet been extensively employed in commercial batteries as they suffer from poor ionic conduction at acceptable temperatures and insufficient stability with respect to the anode. The discovery of solid glassy electrolytes evolved from an antiperovskite structure overcomes the disadvantages of traditional rechargeable batteries such as the formation of dendrite, the presence of SEI, large volumetrics [26] and results in a high ionic conductivity at room temperature in the order of 10^{-4} to 10^{-3} S cm⁻¹ up to a stellar value of 0.025 S cm⁻¹ and low activation energies in the range of 0.2–0.3 eV [38]. Therefore, Li/Na rich antiperovskites (Li/NaRAP) are promising in solid-state batteries.

One of the main goals of these studies was to search efficient alternatives to Li ions where we concluded that cheap, abundant, and non-toxic Na was the most possible alternative for Li [94–97]. Na ion batteries are considered as a possible lower-cost alternative to Li-ion batteries due to the abundance of sodium in the earth's crust [98]. As already mentioned that Li₃OCl is promising as a solid-state electrolyte. Being a structural analog of Li₃OCl, Na₃OCl can be the best choice as a solid electrolyte for Na ion batteries.

Antiperovskite (A₃XY) is similar to perovskite (ABX₃) with reversed cation (A,B) and anion (X,Y) positions. Most perovskites undergo symmetry-breaking transitions resulting from the distortions or rotations of the octahedra under temperature and pressure variations [99]. A method for describing and classifying tilted octahedra only in cell-doubling perovskite is shown by Glazer notation which uses symbols of the type $a^*b^*c^*$. The component tilts can be taken about the pseudocubic axes of the untilted perovskite. a, b, c denotes the magnitude of the angles of tilt about the three unit-cell axes in accordance to directions [100], [010], [001]. Equality of tilts is represented by repeating one of the letters, that is aac means equal tilts along the [100] and [010] directions with a different tilt along the [001] direction. In addition to the magnitude of the tilt it is also necessary to consider the sign of the tilt. If a particular octahedron is tilted about an axis, then the next octahedron along this axis can be tilted in the same or opposite directions (in-phase or out-of-phase). The superscript * being +, -, 0 indicates in-phase, out-of-phase or no tilt along a specific axis, respectively. Glazer showed 23 possible simple tilt systems corresponding to 15 space groups [100]. In Howard and Stokes group-theoretical analysis, 15 space groups are listed. Eight tilt systems missing have higher symmetry than the corresponding space group [101]. The knowledge of tilt octahedra is valid in studying structural instability of perovskite and antiperovskite materials.

Karin Hippler studied the single crystal structure of Na₃OCl and observed that oxygen is surrounded by six Na atoms to make distorted octahedra and chlorine is coordinated by 12 Na atoms [50]. Zhao et al. and Zhang et al. reported that Li₃OCl had a cubic structure (Pm $\bar{3}$ m) [11, 102], and Zinenko et al. showed the similar phonon spectra of Na₃OCl [103] and Chen et

al. pointed out phonon instability at R and M points in the cubic structure [99]. Following the work of Chen et al. [99], we were able to show that the energy of Na_3OCl can be lowered by the tilting of Na_6O octahedra and stable phonon modes can be achieved.

Until recently, information on the enthalpies of formation for the Na_3OCl and its thermodynamics properties and phase change were not available. Despite the experimental synthesis and identification of the cubic $\text{Pm}\bar{3}\text{m}$ phase by Hippler *et al.*, [50] dating back to more than 30 years, only recently thorough characterizations have been reported. [104, 105] Moreover, recent theoretical studies on a similar class of materials such as halide perovskites imply *the necessity of including lattice anharmonicity*, particularly, for the reliable prediction of phase transition temperature that matches well with available experimental data. For example, Tadano and Saidi calculated the cubic-to-tetragonal phase transition temperature of $\alpha\text{-CsPbBr}_3$ (404 - 423 K) by obtaining a very small difference from the experimental measurement (403 K). [106] For this outcome, they included the loop diagram that consists of quartic interatomic force constants (IFCs), and the contribution of the bubble self-energy term that consists of cubic IFCs on top of the self-consistent solution (SC1). Moreover, Tadano and Tsuneyuki found that lattice anharmonicity plays an important role in describing the lattice thermal conductivity of type-I clathrate $\text{Ba}_8\text{Ga}_{16}\text{Ge}_{30}$. [107]

The imaginary modes associated with dynamic instabilities are fundamentally anharmonic in nature and a quantitative description requires moving beyond the harmonic approximation. Using the finite-displacement method to calculate these higher-order terms comes at a considerably higher computational cost than their harmonic equivalents, and perturbation theory is not valid for highly anharmonic materials where the anharmonic corrections to the harmonic energies are significant. In these cases, alternative non-perturbative approaches are required to describe the anharmonicity. Although typically more expensive than the perturbation theory-based alternatives, these methods have the advantage of implicitly taking into account higher-order anharmonicity and temperature effects.

As can be seen, there are a growing number of methods in the literature for going beyond the (quasi-) harmonic approximation by describing anharmonicity in lattice dynamics, including imaginary modes, but most of these come at a substantially higher computational cost over the simpler mode-mapping and renormalisation approaches described in the previous section. When choosing an appropriate treatment, there is generally therefore a trade-off between computational cost and accuracy, and the balance will be determined by both the system under study, the properties to be calculated, and the required level of accuracy. For systems with strongly-coupled and highly-anharmonic modes, techniques such as SCAILD, TDEP or the SSCHA will give accurate results but at an increased computational cost. On the other hand, in systems where the anharmonicity is largely restricted to a small number

of imaginary modes, or for studies where cost is a primary concern (e.g. high-throughput modelling), the significantly cheaper mode-mapping approaches may suffice.[108]

In many perovskite materials, the high symmetry cubic phase is stable at a high temperature, and with decreasing temperature, structures with lower symmetry such as tetragonal, orthorhombic, and monoclinic phases become stable. Therefore, in the harmonic phonon band structures of cubic SrTiO₃, PbTiO₃, and BaTiO₃ imaginary frequencies are found.[56, 109, 110] Both halide and oxide perovskites are well-known materials and an increasing amount of research reports their intriguing characteristics. Antiperovskites are structurally similar to perovskites. However, atomic positions occupied by cations in perovskites are replaced with anions in antiperovskites and *vice versa*. In terms of applications, antiperovskite alkali metal oxyhalides are good candidates for solid-state electrolytes.[111] Cubic Na₃OCl has imaginary frequencies at the *M* and *R* modes, and 14 possible tilted systems are generated by combining $M_3^+ \oplus R_4^+$ distortions that have lower static energy than the cubic phase.[105] In this paper, the stability of these 14 tilted phases, as well as the cubic phase, are discussed in terms of the Gibbs free energy using the quasi-harmonic approximation (QHA) method, which considers the effect of volume expansion to figure out the most stable phase and phase transition during the cooling down process.

3.2 Computational methods

Calculations are performed in the framework of the Vienna ab initio simulation package (VASP).[112] The generalized gradient approximation (GGA) in the Perdew-Burke-Ernzerhof parametrization[71] is used for the exchange correlation potential. The electron-ion interactions are described by the projector augmented wave (PAW) method.[77] The geometries have been relaxed using conjugate gradient method with forces estimated until less than 0.001 eV/Å using the Hellman-Feynman theorem. The total energy is converged to 10⁻⁶ eV with the energy cutoff of 500 eV. The tetrahedron method with Blöchl corrections is chosen for a very accurate total energy in full relaxation.

3.2.1 Harmonic phonon calculations

The harmonic approximation assumes that the second derivative of potential energy with respect to the atomic displacement is constant. This is a reasonably good approximation, particularly for the materials where the atoms are tightly bound through a strong covalent bond. In other words, the shape of the potential energy surface around the energy minimum is close to a parabolic shape for these materials. However, for the materials formed with the

relatively weak bond between constituent atoms, the curvature around the energy minimum easily deviates from parabolic shape even with a displacement caused by the thermal excitation energy equivalent to room temperature. In this case, the anharmonic shape of the potential energy surface can be interpreted as the change of the effective harmonic frequency depending on the temperature.

Phonopy code [113] is used to generate the phonon dispersion curves and verify the space group of the 15 tilted structures before and after relaxation. The k-path in first Brillouin zone is selected using Xcrysden program [114]. Band structure and density of states calculation are obtained through the generalized gradient approximation (GGA) and hybrid functional Hyed-Scuseria-Erznerhof (HSE) methods [115].

The phonon dispersion of cubic $Pm\bar{3}m$ and 14 tilted structures are generated by the Phonopy code [113]. In the Phonopy code, force sets are created using finite displacement method. [116–118]

3.2.2 Quasi-harmonic approximation

For a certain class of materials, the harmonic approximation could be a cost-efficient and reliable way to model material properties. Moreover, there are well-established methods for calculating thermodynamics quantities out of phonon band structure calculations. However, for some materials that have strong lattice anharmonicity, higher-order force constants need to be considered for the reliable prediction of material properties. Herein, we first draw the P - T phase diagram of Na_3OCl through the Gibbs free energy calculated with the quasi-harmonic approximation (QHA). These calculations enable us to investigate phase change in a wide temperature and pressure range with a relatively small computational cost. Then, we move on to the anharmonic phonon calculations to examine the effect of lattice anharmonicity in the phase transition of the material. Since the number of interatomic force constants dramatically increases in case, the materials have low symmetry, so we selected the high-symmetry cubic phase only for this purpose. [113, 119]

By expanding the harmonic phonon model of lattice dynamics, the QHA describes the thermal expansion of the material. In this approximation, phonon frequencies become volume-dependent while the harmonic approximation holds for each volume.[120, 121] The QHA turns out to be a good approximation at temperatures far below the melting points[122, 123] and many studies were performed with the QHA to predict the phase-dependent thermodynamic and elastic properties of the materials, which are consistent with experimental reports. The quasi-harmonic approach implemented in the Phonopy code is used to calculate thermodynamic quantities and estimate the phase transition. [109, 124–133]

The Gibbs free energy $G(T,P)$ is an useful thermodynamic potential in the study

of processes at constant temperature T and pressure P . Through examining the free energies $G(T, P)$ of possible crystal phases, phase changes can be monitored by varying two thermodynamic parameters. In our calculations, the Gibbs free energy G is obtained from minimizing the availability or non-equilibrium Gibbs free energy (G^*) with respect to the volume V at a given T and P as follows. [52]

$$G(T, P) = \min_V [U_{el}(V) + F_{vib}(T, V) + PV], \quad (3.1)$$

where U_{el} is the total electronic energy, $G^*(T, V, P) \equiv U_{el}(V) + F_{vib}(T, V) + PV$, and F_{vib} is the vibrational free energy. The vibrational free energy can be calculated from the QHA or anharmonic approaches using the phonon density of states. Based on QHA the vibrational free energy F_{vib} is expressed as [113]

$$F_{vib}(T, V) = \frac{1}{2} \sum_{qj} \hbar \omega_{qj}(V) + k_B T \sum_{qj} \ln \left[1 - \exp \left(-\frac{\hbar \omega_{qj}(V)}{k_B T} \right) \right]. \quad (3.2)$$

where the index j labels the phonon modes for each crystal momentum vector q .

3.2.3 Self-consistent phonon approach

In the phonon calculations considering lattice anharmonicity, the most important procedure is determining IFCs. To this end, it is necessary to have structures with atoms that are displaced from their force-zero positions. If the small number of atoms are displaced, we need to have relatively large structures. Sometimes, it is necessary to have several thousands of structures even for high-symmetry cubic phase. In this case, the error for the determination of IFCs is very small since the amount of displacement is constant and the direction of displacements are along each of three orthogonal axes. Therefore, one important aspect of our methodology is the use of atomic-scale calculations to evaluate forces acting on individual atoms that are displaced from their force-zero structure. These effects do play a crucial role in determining the impact of anharmonic effects. To this purpose a first strategy consists in resorting to density functional theory [134] (DFT) as implemented in the Vienna ab initio simulation package (VASP).[112] The Perdew-Burke-Ernzerhof (PBE) version of generalized gradient approximation (GGA) [71] is adopted for the exchange-correlation functional. The electron-ion interactions are described by the projector augmented wave (PAW) method.[77] The geometries are relaxed using the conjugate gradient (CG) method until the Hellman-Feynman forces on the individual atoms become less than 0.001 eV/Å. The convergence criteria of total energy in the self-consistent field (SCF) loop is 10^{-8} eV with the energy cutoff of 500 eV. The tetrahedron method with Blöchl corrections is chosen for accurate integration over the

Brillouin-zone.

As a second strategy of structural sampling, we resorted to a scheme fully rooted into ab-initio molecular dynamics (AIMD). [135–137] We initially conducted AIMD simulations, within a Born-Oppenheimer scheme [138], in the canonical NVT ensemble by setting the temperature to 300 K. The thermostat of Nosé-Hoover was implemented. [139] This canonical simulations lasted for 4 ps, with a time step of 2 fs. From the trajectory obtained, we sampled 80 atomic configurations at constant time intervals. Subsequently, on these configuration, all the atoms inside the simulation cell were randomly displaced by 0.1 Å. The atomic forces for the configurations prepared in this manner were obtained using DFT calculations with the energy cutoff of 500 eV and $4 \times 4 \times 4$ k -grids. The methods for structure sampling employed in this study are very much consistent with each other. However, AIMD proved more efficient and it has been mostly adopted throughout this study.

When performing SCP calculations (as implemented in ALAMODE [140]) one has to keep in mind that considering lattice anharmonicity is analogous to the quasiparticle GW method in the electronic structure calculations. As the GW calculations consider many-body interactions starting from Kohn-Sham eigenstates, the SCP theory considers lattice anharmonicity by solving the Dyson equation that considers phonon many-body interactions. In doing so, we need to consider three main anharmonic self-energy terms, the so-called tadpole, loop, and bubble diagrams. Each of the three terms can be calculated with cubic or quartic IFCs (Φ_3, Φ_4). However, finding a fully self-consistent solution of the Green function $G(\omega)$ in the Dyson equation including those three self-energy terms is very challenging because of the bubble self-energy term that contains an ω dependence. Therefore the strategy of Tadano *et al.* is initially to obtain a self-consistent solution without the bubble term (SC1). Then the fully dressed Green function can be solved with the Dyson equation that contains frequency dependent bubble self-energy and the solution of SC1 as an input phonon propagator. Therefore the Dyson equation that needs to be solved can be written as follows:

$$\{G_q(\omega)\}^{-1} \approx \{G_q^S(\omega)\}^{-1} - \Sigma_q^B [G^S, \Phi_3] (\omega). \quad (3.3)$$

Tadano *et al.* end up with the following self-consistent equation to practically deal with the above equation.[106]

$$\Omega_{qj}^2 = \left(\omega_{qj}^S\right)^2 - 2\omega_{qj}^S \text{Re} \Sigma_{qj}^B [G^S, \Phi_3] (\omega = \Omega_{qj}) \quad (3.4)$$

where ω_{qj}^S is the self-consistent solution (SC1) obtained without frequency dependent bubble self-energy term. Instead of solving for fully self-consistent solutions of Eq. (3.4), by putting $\omega = \Omega_{qj}$, we can obtain the solution similar to G_0W_0 calculations in the electron many-body

calculations (QP-NL). Depending on the ways that the frequency in the bubble self-energy is approximated in Eq. (3.4), there are two more levels of approximations. [106] Those are corresponding to the cases when $\omega = 0$ and $\omega = \omega_{qj}^S$ which are denoted as QP[0] and QP[S], respectively.

3.3 Result and discussion

3.3.1 Structural stability

As already mentioned that Li₃OCl is promising as a solid-state electrolyte. Being a structural analog of Li₃OCl, Na₃OCl can be the best choice as a solid electrolyte for Na ion batteries. However, similar to cubic Li₃OCl, cubic Na₃OCl also has negative frequencies at the M and R points in its phonon dispersions. Following the work of Chen *et al.* [99], we were able to show that the energy of Na₃OCl can be lowered by the tilting of Na₆O octahedra and stable phonon modes can be achieved.

Optimization and relaxation process gave the lattice parameter of Na₃OCl cubic primitive cell $a=4.538$ Å using the GGA method and $a=4.382$ Å using the local density approximation (LDA) method. In experiment, Karin Hippler reported $a=4.496(2)$ Å [50]. Due to the approximation of the exchange-correlation energy functional, convergence of the used basis set, and how well the pseudopotentials compare to full potential all electron methods, our calculated results are not exactly the same as the experiment but it is being acceptable. In Kohn-Sham's equation, the exchange-correlation energy functional is computed approximately by LDA or GGA methods. LDA is generally not accurate enough to describe the energetics of chemical reactions (heats of reaction and activation energy barriers), leading to an overestimation of the binding energies of molecules and solids in particular [141, 142]. GGA is presented to overcome such deficiencies. Therefore, the results obtained from GGA are much better than LDA method. As compared to the experimental results, LDA result is underestimated by 2.54% while GGA result is overestimated by 0.93%.

At first glance in Fig. 3.1(a), we easily realize that the lattice vibrations are unstable at M and R symmetry points of the cubic Pm $\bar{3}$ m Na₃OCl in a 3×3×3 supercell that show imaginary frequencies at the M and R points in the phonon dispersion curves. We already checked for phonon convergence from 1×1×1 primitive cell to 6×6×6 supercell, the results show that phonon modes in 3×3×3 supercell have very similar properties to them in larger supercell size. The soft phonon modes occur at M and R which still remain negative when cell size increases but a phonon mode at M is slighter negative for the enlarged cell size. Phonon curves illustrate the elastic vibrations of atomic lattice points of crystal. When cell

size increases the interaction between lattice points becomes more practical and boundary effect is reduced which increases the computational accuracy. In phonopy, the generation of force constants relies on finite displacement method. Na_3OCl is a non-metallic crystal which is polarized due to atomic displacements. The macroscopic electric field is generated by the long-range character of the Coulomb forces that are associated with long wave longitudinal optical phonons [143]. Through non-analytic term correction, the LO-TO (longitudinal-optical, transverse-optical) curves split at the Γ point [144]. Oxygen and chlorine have isotropic Born effective charges with values of $-1.795e$ and $-1.283e$, respectively. The diagonal Born effective charges of Na are $Z_{xx}=0.938e$ and $Z_{yy}=Z_{zz}=1.070e$. The calculated Born effective charges of O, Cl and the average one of Na are quite same as their nominal ionic charges $-2e$, $-e$ and $+e$ which is the characteristic of a pure ionic crystal. For cubic crystal, their electronic and ionic dielectric tensors are diagonal and have only one independent component [145]. The dielectric tensor of Na_3OCl has identical diagonal values of about 3.0 which is larger than the theoretically reported result of 1.97 using TB-mBJ functional [146]. Up to now, no experimental report on the dielectric constant of this material is reported.

The instability at M and R points, indicating the motion of sodium in these modes leads to a rotation of octahedra Na_6O [103]. As you can see in Fig. 3.2 the animation trend of their soft modes displacement that induces in-phase and out-of-phase rotations. The unstable modes imply that the crystal energy can be lowered through octahedral tilts generating the other 14 tilt structures. In Fig. 3.1(b) the partial density of states indicate that the unstable modes are concerned only with the Na ions. Most of the lower frequency stable modes are distributed by Cl. O and Na reigns the high-frequency modes above approximately 5 THz.

The soft modes at M and R points are expressed by M_3^+ and R_4^+ irreducible representations, where M_3^+ is in-phase tilting and R_4^+ is out-of-phase tilting [147]. A method for describing and classifying tilted octahedra only in cell-doubling perovskite is shown by Glazer notation which uses symbols of the type $a^*b^*c^*$. The component tilts can be taken about the pseudocubic axes of the untilted perovskite. a , b , c denotes the magnitude of the angles of tilt about the three unit-cell axes in accordance to directions [100], [010], [001]. Equality of tilts is represented by repeating one of the letters, that is aac means equal tilts along the [100] and [010] directions with a different tilt along the [001] direction. In addition to the magnitude of the tilt it is also necessary to consider the sign of the tilt. If a particular octahedron is tilted about an axis, then the next octahedron along this axis can be tilted in the same or opposite directions (in-phase or out-of-phase). The superscript * being +, -, 0 indicates in-phase, out-of-phase or no tilt along a specific axis, respectively. Glazer showed 23 possible simple tilt systems corresponding to 15 space groups [100]. In Howard and Stokes group-theoretical analysis, 15 space groups are listed. Eight tilt systems missing have higher symmetry than

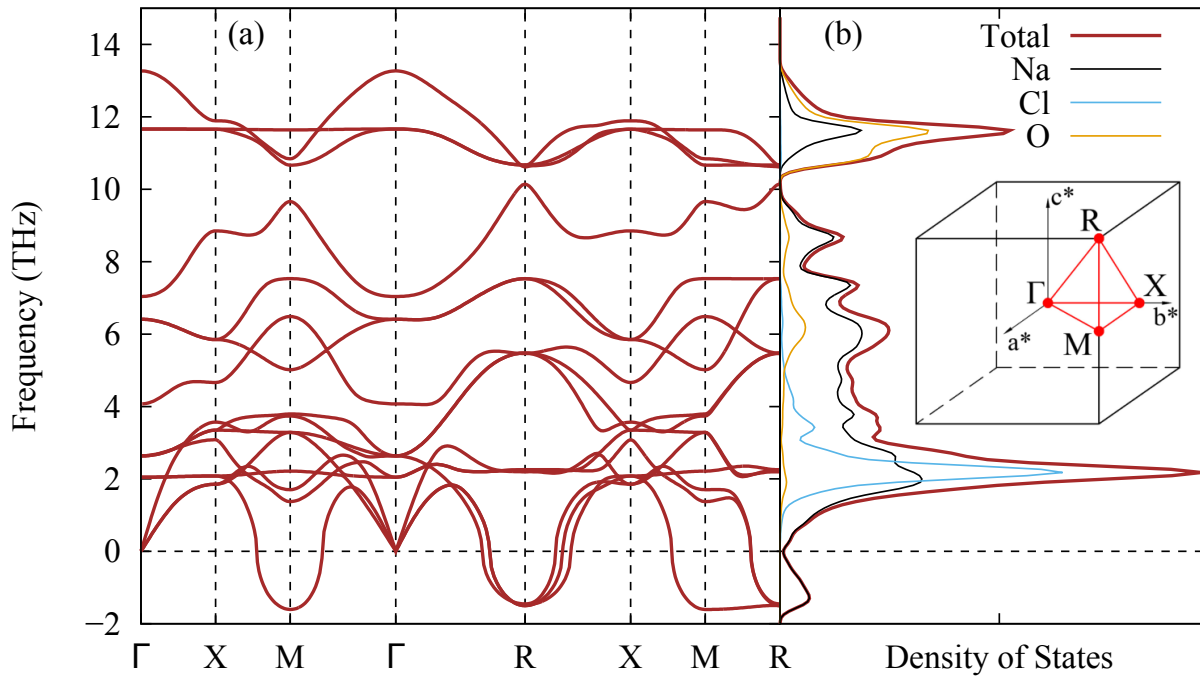


Figure 3.1: (a) Phonon band structure and (b) density of states of the cubic $\text{Pm}\bar{3}\text{m}$ phase. The soft modes at M and R points in the phonon band structure indicate that the cubic $\text{Pm}\bar{3}\text{m}$ phase is dynamically unstable. The red curve in (b) represents the total phonon density of states. The black, blue and orange curves corresponds to the partial phonon density of states of Na, Cl, O, respectively. The k -path in the first Brillouin zone is shown in the inset. The unstable soft modes dominantly come from Na.

the corresponding space group [101]. The knowledge of tilt octahedra is valid in studying structural instability of perovskite and antiperovskite materials. Fig. 3.2(a) shows the top view of the cubic nontilted crystal structure. The M_3^+ distortion results in an in-phase rotation, as shown in Fig. 3.2(b), and it corresponds to the $a^0a^0c^+$ structure following the Glazer's notation [100]. Similarly, the R_4^+ distortion results in an out-of-phase rotation, as presented in Fig. 3.2(c), and it corresponds to $a^0a^0c^-$. The structure of the monoclinic $P2_1/m$ Na_3OCl results from the $M_3^+ \oplus R_4^+$ distortions as shown in Fig. 3.2(d). The tilt is in-phase along the a axis and the tilts along the b and c axes are out-of-phase, which gives the Glazer's notation of $a^+b^-c^-$. The negative frequency at M point leads to M_3^+ distortion that derives to 4 tilted systems $a^0a^0c^+$, $a^0b^+b^+$, $a^+a^+a^+$, and $a^+b^+c^+$. The irreducible representations R_4^+ led from soft mode at R point are related to 6 tilted systems $a^0a^0c^-$, $a^0b^-b^-$, $a^-a^-a^-$, $a^0b^-c^-$, $a^-b^-b^-$, and $a^-b^-c^-$. The $M_3^+ \oplus R_4^+$ distortions result in 4 tilted systems $a^0b^+c^-$, $a^+b^-b^-$, $a^+b^-c^-$, and $a^+a^+c^-$ [147]. As a whole, M_3^+ and R_4^+ distortions of space group $\text{Pm}\bar{3}\text{m}$ can generate 14 tilt systems. The energetic stability of ionic crystals is typically reported in a variety of manners, such as the formation energy, the cohesive energy, and the lattice energy [148]. Fig. 3.2(e) presents the calculated energies of all the 14 tilt systems relative to cubic $\text{Pm}\bar{3}\text{m}$ Na_3OCl ($\Delta E = E_{\text{tilt}} - E_{\text{nontilt}}$, where E_{tilt} is the energy of a tilt system and E_{nontilt} is the energy of cubic $\text{Pm}\bar{3}\text{m}$ Na_3OCl). The energies are calculated using a $2 \times 2 \times 2$ unit cell (U.C.) and a $8 \times 8 \times 8$ k -point mesh for each structure. Space groups of 15 systems agree well with the previous study of tilting octahedra in perovskites [101]. For Li_3OCl , 10 tilted structures are more stable than the cubic phase and the remaining 4 structures are energetically close to the cubic phase. The maximum energy difference between the cubic phase and the most stable structure of Li_3OCl is less than 1 meV/U.C. [99]. While all the 14 tilted structures of Na_3OCl are much lower in energy than the cubic $\text{Pm}\bar{3}\text{m}$ nontilted structure with the energy differences ranging from 11 to 16 meV/U.C., the energetically most stable structure is $P2_1/m$. By using the exchange-correlation functional with LDA, the computed energy of monoclinic $P2_1/m$ relative to cubic $\text{Pm}\bar{3}\text{m}$ is -27 meV/U.C., and the most stable structure is unchanged. The cohesive energy of Na_3OCl is defined as $E_{\text{coh}} = [(3E_{\text{Na}} + E_{\text{O}} + E_{\text{Cl}}) - E_{\text{Na}_3\text{OCl}}]$, where E_{Na} , E_{O} , and E_{Cl} refer to the total energies of isolated Na, O, and Cl atoms, respectively. The cohesive energy of the nontilted Na_3OCl in $\text{Pm}\bar{3}\text{m}$ phase is 15.560 eV/U.C. The formation energy (E_f) of Na_3OCl is defined as $E_f = [E_{\text{Na}_3\text{OCl}} - (3E_{\text{Na}(\text{bcc})} + \frac{1}{2}E_{\text{O}_2} + \frac{1}{2}E_{\text{Cl}_2})]$ where $E_{\text{Na}_3\text{OCl}}$, $E_{\text{Na}(\text{bcc})}$, E_{O_2} , and E_{Cl_2} refer to the total energies of bulk Na_3OCl , bulk Na in body-centered-cubic (bcc) phase, and gas phase O_2 and Cl_2 molecules, respectively. The formation energy of Na_3OCl per primitive cell is equal to -7.932 eV.

The tolerance factor of an antiperovskite A_3XY is defined as $t = \frac{r_Y + r_A}{\sqrt{2}(r_X + r_A)}$, where r_X , r_Y , r_A are the radii of the X-anion, Y-anion, and A-cation, respectively. The tolerance factor of

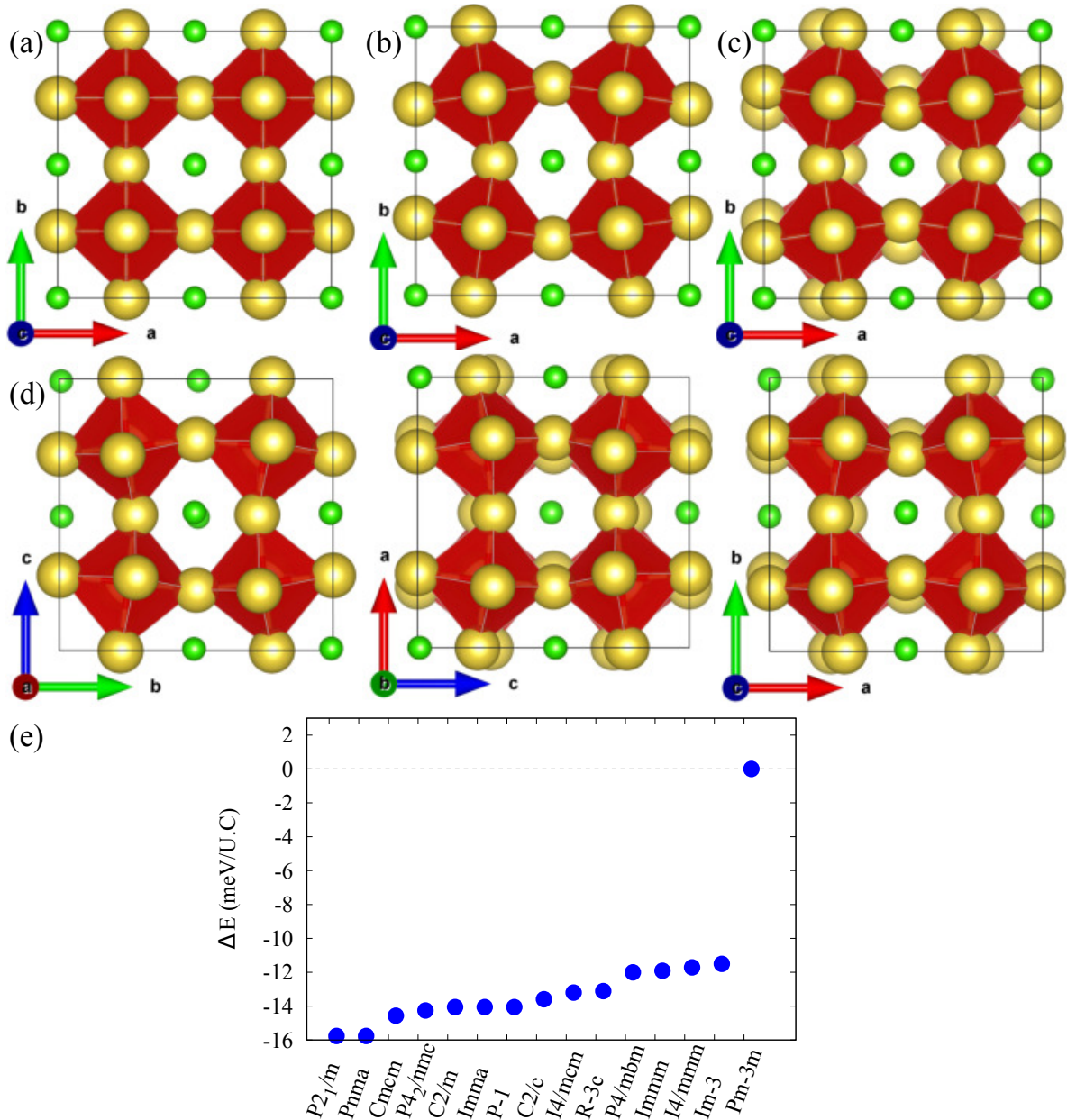


Figure 3.2: (a) Nontilted cubic $\text{Pm}\bar{3}\text{m}$ crystal structure is denoted by $a^0a^0a^0$. (b) M_3^+ distortion indicates in-phase rotation (the same rotation direction of octahedral layers along an axis) which is simply presented by $a^0a^0c^+$ structure. (c) The tilted $a^0a^0c^-$ system that indicates R_4^+ distortion carried by out-of-phase rotation (the alternating rotation of octahedral layers along an axis). (d) Three different views of the tilted $a^+b^-c^-$ (monoclinic $\text{P}2_1/\text{m}$) structure resulting from the combination $M_3^+ \oplus R_4^+$ distortions. (e) Energy profile of the 14 tilted structures relative to the nontilted cubic $\text{Pm}\bar{3}\text{m}$ Na_3OCl . For comparison, the energies of tilted structures are transformed into the energies per $1 \times 1 \times 1$ unit cell. All the 14 tilted structures of Na_3OCl are lower in energy than the cubic $\text{Pm}\bar{3}\text{m}$ nontilted structure where monoclinic $\text{P}2_1/\text{m}$ is the most stable structure.

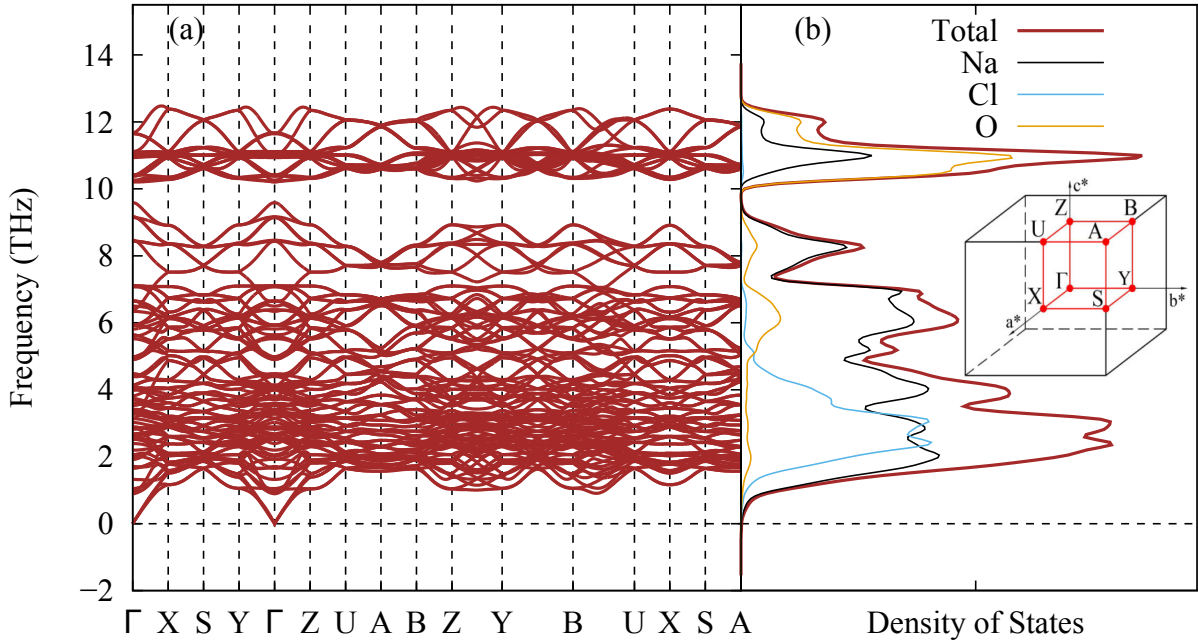


Figure 3.3: (a) Phonon dispersion curves and (b) total and partial densities of states of monoclinic $P2_1/m$. The phonon dispersion curves and the total density of states show no negative modes, which proves the monoclinic $P2_1/m$ is dynamically stable.

Na_3OCl is 0.83 which increases to 0.87 for Na_3OBr and 0.94 for Na_3OI . The ionic radii of a Na cation and Cl, Br, I, and O anions are taken from Shannon's data [149]. It suggests that the substitution of Cl with larger ions results in increasing tolerance factor and it approaches 1. In other words, the cubic phase becomes favorable in case of larger substituents for Cl where the Na_6O octahedral tilt will lead to higher energy [145, 150]. However, consistent with energy and phonon calculations, the lower tolerance factor (0.83) suggests that cubic phase is not favorable for Na_3OCl and the Na_6O tilt is needed to achieve the stable phase.

The lattice vibrations of all 14 tilted structures are studied to find out the most stable structure among tilted phases. In Fig. 3.3, no negative frequency in phonon dispersion curves is shown for monoclinic $P2_1/m$, which confirms its dynamic stability. Therefore, $P2_1/m$ is both energetically and vibrationally stable while the other 13 tilt systems have unstable phonon curves as well as higher energies. The total and partial phonon densities of states in Fig. 3.3(b) strongly determine the stability of monoclinic $P2_1/m$ since the calculation takes place on a dense k mesh that fully describes the first Brillouin zone. The chosen k -paths in the first Brillouin zone of monoclinic $P2_1/m$ are presented in Fig. 3.3(b) as well.

The sequece phase change of Na_3OCl is a curious subject from the finding out the most stable monoclinic $P2_1/m$ phase at 0 K. By studying the temperature effect in phase transition the harmonic approach fails to explain, we need to consider the anharmonic

contributions to vibrations. In the harmonic approximation, the vibrational energy is considered up to the second order for small displacement while cubic and higher order terms are neglected.[113, 119] The solution of harmonic equation of motion is well known but the anharmonic one does not have exact solutions and needs other approximation schemes. The anharmonic part usually leads to only a small modification of the overall behavior. Since the amplitudes of the displacements are expected to decrease at low temperatures (i.e. the kinetic energy of the chain), the harmonic term will be the only important term at low temperatures. The problem is often treated with a simplest model first and then corrected with more accurate models.[54] The temperature dependence of equilibrium properties, phase transitions, and thermal conductivity cannot be understood with only the harmonic approximation since they are related to anharmonic interactions.

The QHA results in Fig. 3.4 show the sequence of phase change from cubic $\text{Pm}\bar{3}\text{m}$ to orthorhombic Bmmb (denoted by $a^0b^+c^-$) and then to monoclinic $\text{P2}_1/\text{m}$ (denoted by $a^+b^-c^-$). The cubic phase is the most stable phase at high temperature and low pressure, and it has a phase transitions to the orthorhombic phase at around 650 K. The orthorhombic Bmmb phase is a tilted phase that results from the condensation of imaginary M and R soft modes. The condensation of the soft mode at M causes in-phase rotation along the y -axis and the soft mode condensation at R induces out-of-phase rotation along the z -axis. With decreasing temperature, the next phase transition is to the monoclinic $\text{P2}_1/\text{m}$ phase that is derived from a condensed X soft mode of the $a^0b^+c^-$ phase. [151] This phase transition to the $\text{P2}_1/\text{m}$ structure is also known to be induced by the combination of M and R soft phonon condensation from the cubic phase. According to the quasi-harmonic phonon calculations, this phase transition is predicted to occur at around 135 K.

To check the convergence of harmonic force constants with respect to the supercell size, we calculated the root-mean-square (RMS) of the difference of force constants. When the RMS is calculated with the force constants of $4\times 4\times 4$ supercell as the reference, we found that the RMS values of $1\times 1\times 1$, $2\times 2\times 2$, and $3\times 3\times 3$ supercells are 0.4393, 0.0242, and, 0.0056, respectively. Moreover, we also checked the convergence of free energy in different cell sizes. The results show that the free energy differences of the cubic phase between $2\times 2\times 2$ supercell and $3\times 3\times 3$, $4\times 4\times 4$, and $6\times 6\times 6$ supercells are greater than 10^{-2} eV per unit cell (UC). These energy differences are larger than the free energy differences between cubic and titled phases and, in turn, this results in a large error in the phase transition temperature. However, we confirmed that in the case of $4\times 4\times 4$ supercell, the free energy converges within 10^{-3} eV/UC. Therefore, 3 phases involved in the phase transition, the $4\times 4\times 4$ supercell (320 atoms) with the $2\times 2\times 2$ k -mesh is used to ensure the consistency. Figs. 3.5(a-d) show the non-equilibrium Gibbs free energies of four phases of Na_3OCl . From the minimum at each temperature curve,

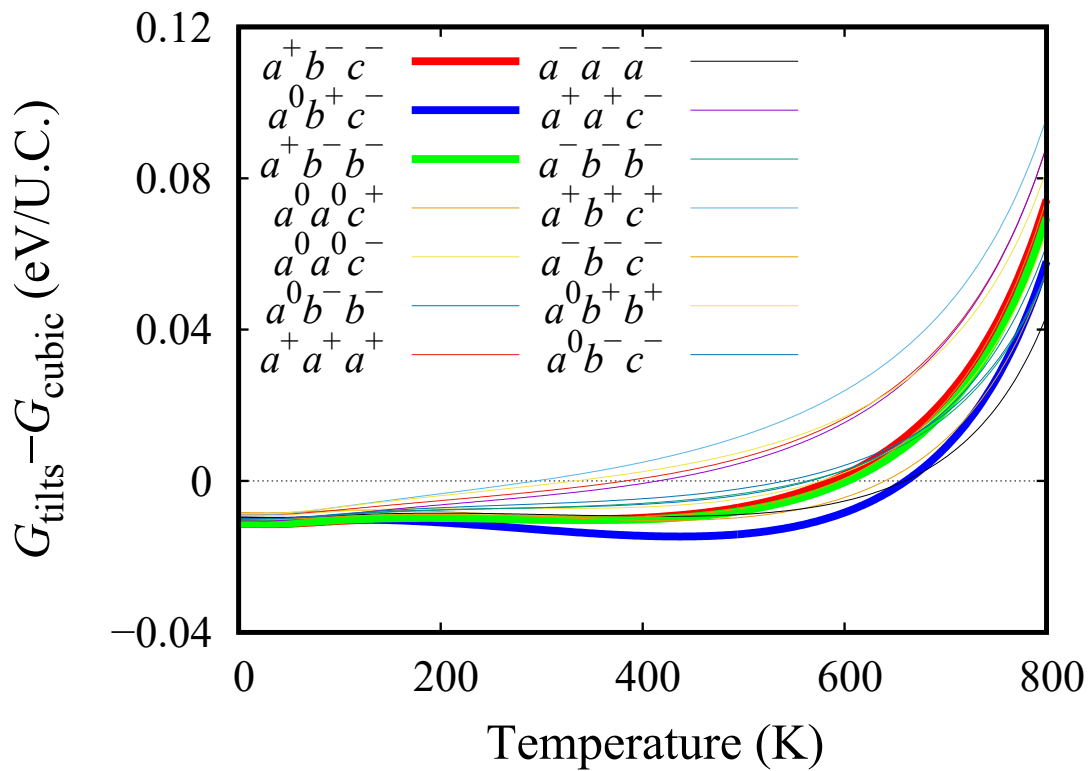


Figure 3.4: Temperature-dependent Gibbs free energies (G_{tilts}) at pressure $P = 0$ for 14 tilted structures of Na_3OCl relative to the Gibbs free energy for cubic (G_{cubic}) Na_3OCl .

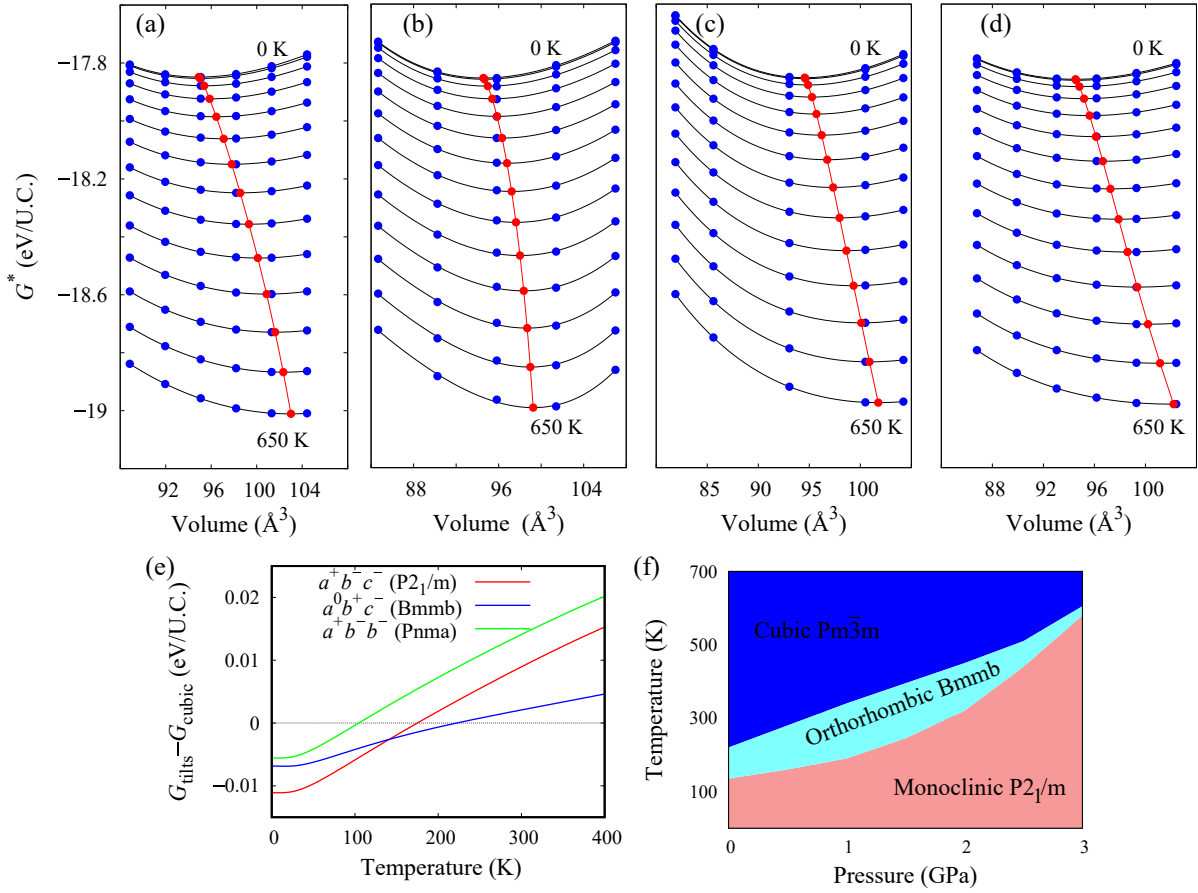


Figure 3.5: Non-equilibrium Gibbs free energies $G^*(T, V, P)$ for the (a) cubic $\text{Pm}\bar{3}\text{m}$, (b) orthorhombic Bmmb , and (c) monoclinic $\text{P}2_1/\text{m}$, and (d) orthorhombic Pnma phases with respect to volume at 0 pressure and different temperatures between 0 K to 650 K are presented by blue circles with black curves fitted to the Birch-Murnaghan equation of states. From the minima of the respective black curves, the Gibbs free energies at zero pressure are obtained, and they are shown with red circles and connected with red lines. (e) The Gibbs free energy difference of the orthorhombic Bmmb , orthorhombic Pnma and monoclinic $\text{P}2_1/\text{m}$ phases were comparable to the cubic phase. (f) P - T phase diagram of Na_3OCl .

the Gibbs free energy G is determined. The difference in the Gibbs free energies between the tilted phase and the cubic phase is shown in Fig. 3.5(e), and it shows that the cubic phase is stabilized at temperatures higher than 220 K. The orthorhombic Bmmb phase is stabilized in the range between 135 K and 220 K.

This phase transition result is consistent with the experimental observation stating that the cubic structure is the most stable phase at room temperature and ambient pressure.[50] The phase diagram can be generated by calculating Gibbs free energies as a function of the temperature for the given six different pressures which are obtained by Eq. (3.1). Fig. 3.5(f) shows that the room temperature stable phase is the lower symmetry phase when the pressure is higher than 0.7 GPa. We propose that Na_3OCl is in the monoclinic $P2_1/m$ phase at a pressure over 2.1 GPa and room-temperature conditions. The orthorhombic phase is observed in the range of pressure between 0.7 and 2.1 GPa, and cubic phase is considered to be the most stable at the pressure below 0.7 GPa.

Due to the relatively small computational cost of phonon calculations with QHA, we were able to examine 3 different polymorphs and plot the phase diagram with respect to temperature and pressure. Despite this advantage, it is also well known that QHA has a limitation in the description of lattice anharmonicity. Therefore we additionally performed self-consistent phonon (SCP) calculations using ALAMODE.[140] It considers not only the second but also fourth-order IFCs at the same time, which enables the description of phonon frequency change with respect to temperature. [56, 152] We also note that previous calculations on oxide or halide perovskites already demonstrated that SCP calculations of the high-symmetry cubic phase are useful for prediction of the phase transition temperature. The literature reports that particular soft phonons lead to phase transition by phonon condensation. Given the structural similarity of Na_3OCl with the perovskite materials, we need to pay attention to the possibility of observing similar behavior.[56]

After finishing force calculations for all sampled structures, we need to determine IFCs out of raw data. This can be understood as the fitting of IFCs using DFT force data. Therefore there could be many detailed choices, including regularization methods that are frequently used in the machine learning to prevent overfitting. However, we found that simple ordinary least square (OLS) fitting works well here. Sometimes, harmonic force constants are determined first with finite displacement sampling and then the other higher orders of IFCs are determined with predetermined harmonic FC fixed. This is the preferred way of fitting since it reduces the possible errors of harmonic FC in the case when all orders of IFCs are determined simultaneously. Here, we found that resulting phonon band structures do not change much even when all orders of IFCs are determined simultaneously. Although IFCs up to quartic terms are used in the SCP calculations, higher orders up to the sixth IFCs are also determined

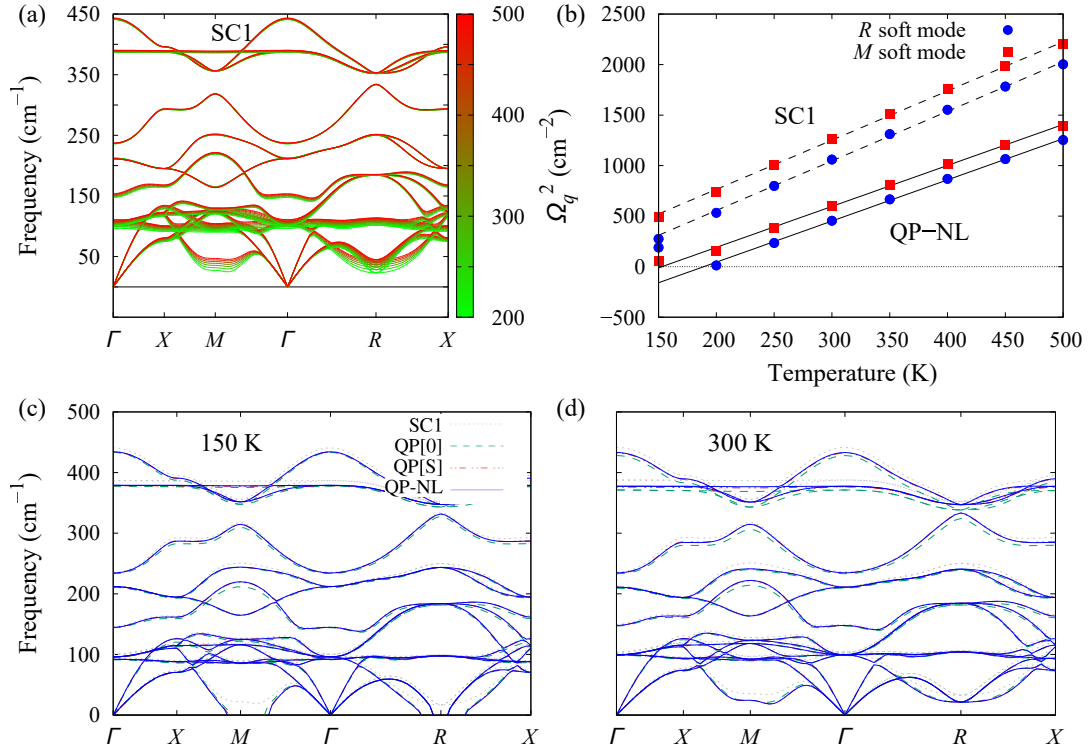


Figure 3.6: (a) Phonon band structure at various temperatures from 200 K to 500 K by considering the fourth-order anharmonic contribution. (b) Temperature dependence of the squared phonon frequencies at the M and R modes. (c, d) Anharmonic phonon dispersion curves of cubic Na_3OCl calculated at 150 K and 300 K (below and above T_c) using different treatments of QP theory. The red dotted lines, green dashed lines, black dash-double-dotted lines, and blue solid lines represent the phonon bands obtained from SC1, QP[0], QP[S], and QP-NL, respectively.

for the accuracy of IFCs that we are going to use.[56, 152] All possible combinations of interactions were considered for harmonic and cubic terms, and the combinations with the distance between atoms less than 12 bohr, 8 bohr, and 8 bohr were considered for the fourth, fifth, and sixth-order IFCs, respectively.

There are imaginary frequencies in the phonon band structures of 12 octahedral tilted structures. However, those imaginary frequencies are neglected in the calculation of vibrational free energy. Moreover, the strong lattice anharmonicity found in perovskite materials raises the need of applying this method, including the consideration of lattice anharmonicity in the antiperovskite Na_3OCl . For the consideration of lattice anharmonicity, we need to prepare a quartic order of interatomic force constants. However, lower symmetry structures require a formidable amount of interatomic force constants. Therefore, here we considered only the high symmetry cubic phase. The phonon band structure of the cubic

Na₃OCl phase shows imaginary frequencies at M and R symmetry points. If we consider lattice anharmonicity, these imaginary frequencies modes turn into soft phonon modes with positive frequency. In addition, they tend to have strong temperature dependence and disappear below a certain temperature. Therefore, through those calculations, we will be able to predict the phase transition temperature. Moreover, the lower energy structure can be viewed as a small modification of the higher-symmetry structure. Because the modification is caused by the distortion corresponding to the eigenvector of the modes with the imaginary frequency, we can predict the symmetry of the low-temperature phase. With this in mind, we performed SCP calculations as implemented in ALAMODE [140]. In Fig. 3.6(a), the anharmonic phonon band structures of cubic $\text{Pm}\bar{3}\text{m}$ Na₃OCl calculated with the SC1 method is shown in the range of temperatures from 200 K to 500 K. We can recognize that by including the fourth-order IFC in the SCP equation, the imaginary phonon frequencies disappear. In doing that, we also found that the q -mesh of $8 \times 8 \times 8$ is a reasonable choice in terms of the convergence of soft mode frequencies at M and R symmetry points (see Table S2 in Supplemental Material). As shown in Fig. 3.6(b), the soft mode frequencies at M and R can be nicely fitted with the equation, $\Omega_q^2(T) = a(T - T_c)$. From Fig. 3.6(b), the result shows that the orthorhombic-to-cubic phase transition occurs at around 86 K, which is an underestimate compared to the QHA result with the $3 \times 3 \times 3$ supercell. It is consistent with the theory that QHA method neglects the imaginary frequencies while the anharmonic approach takes into account the effect of these phonon modes. Accordingly, the vibrational energy decreases in consequence lowering the free energy of the cubic phase.

The calculated anharmonic phonon dispersion curves using SC1 approximation are compared to the one using the QP method by including bubble self-energy in Figs. 3.6(c,d). The SC1 phonon frequencies are overestimated compared to the QP frequencies, and the overestimation is significant in the soft mode while the QP[0] and QP[S] results are close to the QP-NL one. The QP[0] frequencies are slightly underestimated in the optical modes while the QP[S] results are consistent with the QP-NL ones. Similar to SC1 characteristic, through linear fitting of the temperature dependence of squared phonon frequencies, we can estimate the phase transition temperature as given in Table. 3.1. The QP theory with different treatments gives similar results of about 195 K, which is more than two times higher than the transition temperature from the SC1 method and a similar report is given by Tadano *et al.*. By including the bubble self-energy term on top of the SC1 solution they found that the phase transition temperatures of halide perovskite become close to the experimental ones.[106] Their estimation of the transition temperature without the bubble term was almost half of the value compared to the experimental one. However, by including the bubble term, they were able to improve the results significantly. Unfortunately, the experimental phase transition

temperatures of Na₃OCl have not been reported yet. Therefore, direct comparison with the experimental data is not available at this point. Nonetheless, its room-temperature stability of the cubic phase reported in the literature suggests that the current computational predictions are at least in a reasonable range.

The materials with strong lattice anharmonicity also tend to be sensitive to external strain. Therefore we need to carefully consider the effect of thermal expansion on the phase transition temperature. For reliable prediction of thermal expansion, we adopted the PBEsol exchange-correlation functional. It is demonstrated that the lattice constant calculated with PBEsol functional [153] is close to the experimental one compared to that estimated with other functionals such as PBE or LDA. Please note that, without temperature effect, the lattice constant of cubic phase is 4.483 Å which is smaller than PBE lattice constant (4.538 Å) by 1.2%. To consider temperature effect on the lattice constant, thermal expansion of cubic Na₃OCl is calculated with the Helmholtz free energy curves at various temperatures as presented in Fig. 3.7(a). The minimum points of energy-lattice constant curves at each temperature are marked with blue squares. As shown in Fig. 3.7(b), the lattice constant increases almost linearly with increasing temperature. However, we need to keep in mind that thermal expansion curve is plotted from the calculations with fixed lattice constant. Therefore, it is necessary to have different information which shows the relationship between lattice constant versus T_C . For the estimation of T_C , as shown in Fig. 3.7(c), a linear relation of square frequencies at M and R soft modes is used. Note that for the thermal expansion we used self-consistent phonon calculations (SC1), however for the estimation of T_C , we used phonon band structures calculated with additional self-energy term that has frequency dependence (QP-NL). The data in Fig. 3.7(c) are the particular case when the lattice constant is obtained at an energy minimum with the PBEsol functional. We can easily recognize that the frequencies at two soft modes are so close, which results in the phase transition temperature at similar temperatures (152 - 183 K) by the condensation of each soft mode. As shown in Fig. 3.7(b), when the lattice constant increases, the estimated T_C decreases. The crossing point of thermal expansion line and lattice constant versus T_C curve indicates the phase transition point after considering thermal expansion. In comparison with T_C in Fig. 3.7(c) which assumes a fixed lattice constant, the consideration of thermal expansion makes T_C lower by 16 - 21 K (136 vs 152 K and 162 vs 183 K). The effect of thermal expansion seems to be not so significant in this particular material. However, as shown in Fig. 3.7(b), this can be dependent on how the soft mode frequency changes when the lattice constant increases.

Method	Range of transition temperatures (K)
SC1	54 - 86
QP[0]	168 - 195
QP[S]	167 - 195
QP-NL	166 - 195

Table 3.1: Cubic-to-orthorhombic phase transition temperatures are calculated by the QP theory at different levels. Two values in each cell show the transition temperatures estimated from the soft mode frequency at M and R points, respectively

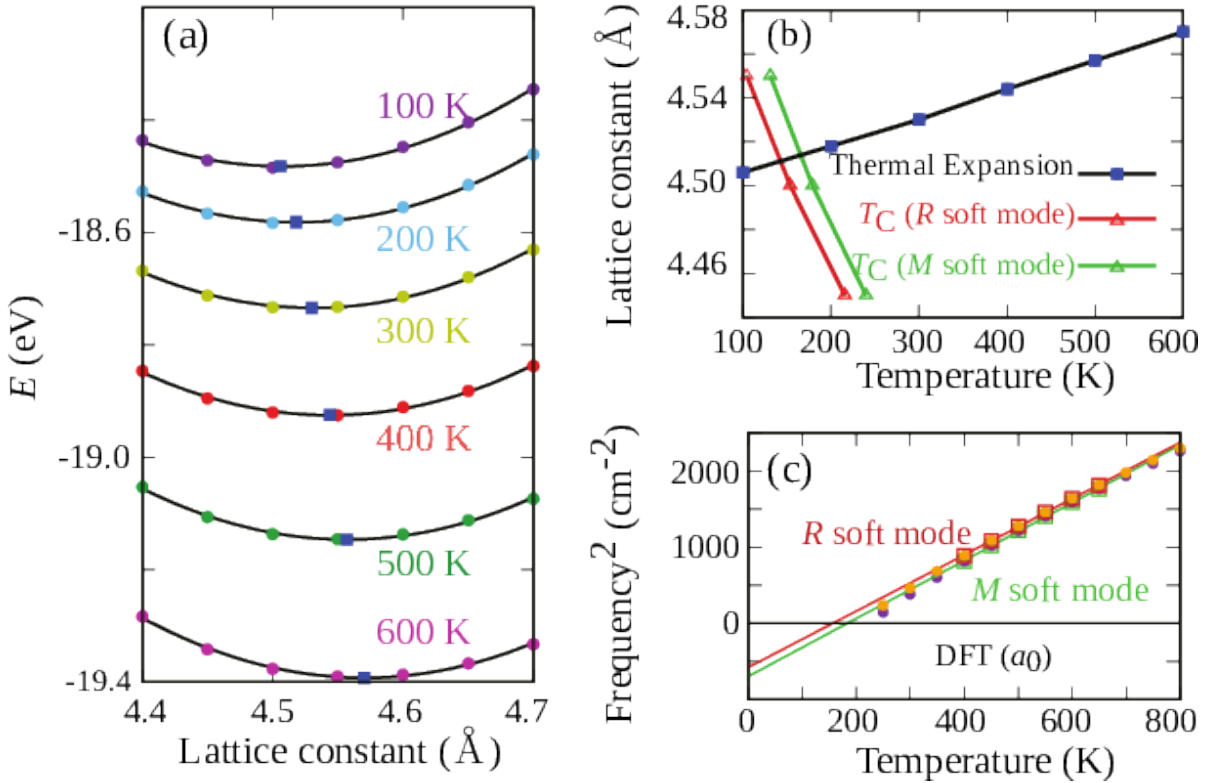
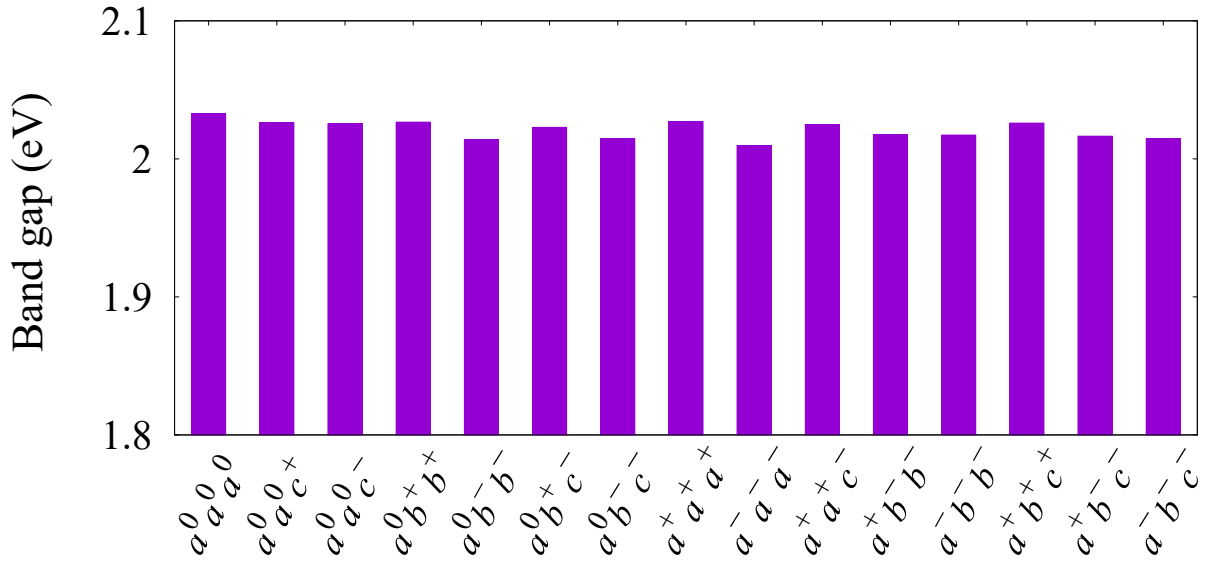


Figure 3.7: (a) Helmholtz free energy curves at various temperatures from 100 to 600 K. The minimum points at each temperature curves are marked with blue squares. (b) Thermal expansion curve and lattice constant versus phase transition temperature T_C curve. (c) Temperature dependence of the squared phonon frequencies at the M and R modes when the lattice constant is obtained at energy minimum with the PBEsol functional. The data points marked with empty squares are used for line fitting.

Figure 3.8: Band gaps for 15 phases of Na₃OCl

3.3.2 Electronic structure and ionic transport properties

Electronic structure and ionic transport properties of Na₃OCl are important as the safety and efficiency indicators for electrolyte applications. Since electrolyte is not supposed to conduct electricity for safety, we calculated the electronic band gaps of the 14 tilted phases including the cubic phase and found that the band gaps of all the phases fall in the range between 2.01 eV and 2.03 eV when we used the GGA functional as shown in Fig. 3.8. In the previous report by Pham *et al.*[105], the band gaps of cubic and monoclinic phases increased to around 3.40 eV when the hybrid functional Hied-Scuseria-Erznerhof (HSE) method is used while the band gaps are around 2 eV when the GGA functional is used [154]. From these results, we may consider Na₃OCl as an insulator in all the tilted phases. Secondly, the ionic transport property is obtained by calculating the migration energy barriers of Na via the vacancy-mediated mechanism[155] with the nudged elastic band (NEB) method [156] for cubic Pm $\bar{3}$ m, orthorhombic Bmmb, and monoclinic P2₁/m phases. NEB calculation is performed in a supercell of 40 atoms. The energy convergence criterion is set to 10⁻³ eV and five intermediate NEB images are used. Fig. 3.9(a-c) show the possible reaction paths of vacancy migration in a schematic way; the Pm $\bar{3}$ m phase has only one path, but the Bmmb and P2₁/m phases have 6 and 12 paths, respectively. Figs. 3.9(d-f) show the calculated minimum energy paths for sodium vacancy migration from one Na site to another in cubic Pm $\bar{3}$ m, orthorhombic Bmmb, and monoclinic P2₁/m phases. There are six available migration paths in orthorhombic Bmmb made of three symmetrically distinct Na sites,[157] and twelve paths in P2₁/m composed of four symmetrically distinct Na sites (see Table S3 and S4 in Supplemental Material for

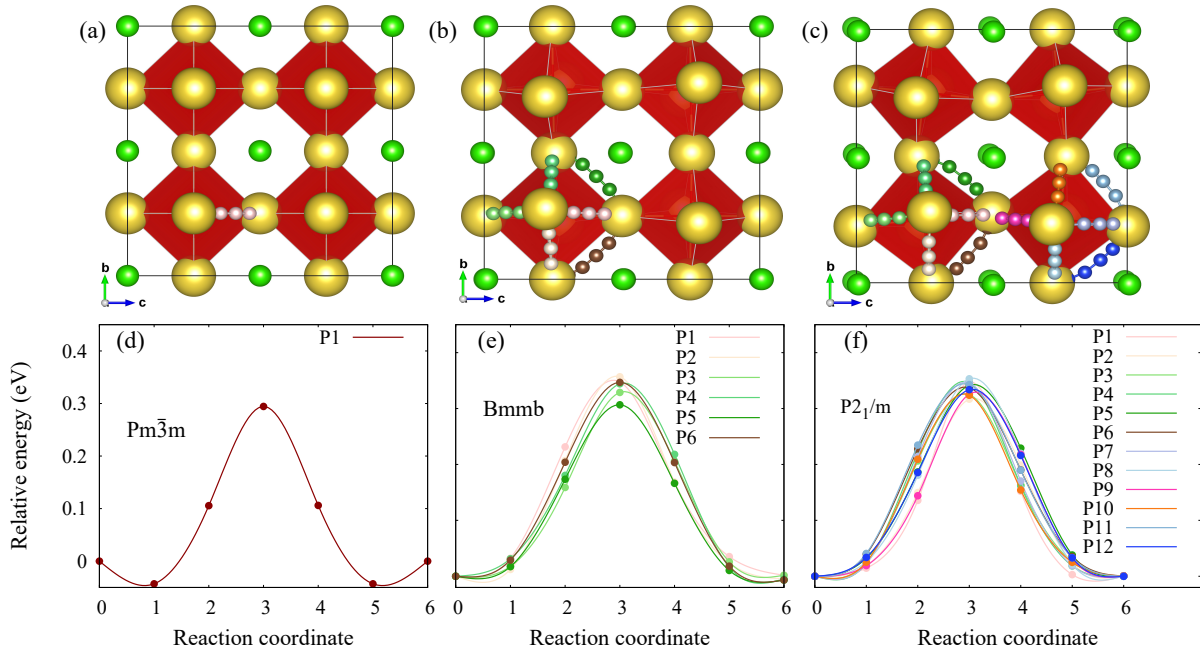


Figure 3.9: Reaction paths for Na migration are shown with the small colored spheres in (a) cubic $Pm\bar{3}m$, (b) orthorhombic $Bmmb$, and (c) monoclinic $P2_1/m$ phases and Na, O, and Cl atoms with the larger yellow, red (inside the red octahedra), and green spheres, respectively. The relative energy changes of vacancy migration through the minimum energy path in (d) cubic $Pm\bar{3}m$, (e) orthorhombic $Bmmb$, and (f) monoclinic $P2_1/m$ phases are illustrated with colors for the corresponding reaction paths.

Wyckoff positions in orthorhombic $Bmmb$ and monoclinic $P2_1/m$ [158]). The single vacancy migration energies are 0.32 - 0.35 eV (average 0.34 eV) for monoclinic $P2_1/m$, 0.31 - 0.35 eV (average 0.34 eV) for orthorhombic $Bmmb$, and 0.30 eV for cubic, respectively. The distorted structures ($P2_1/m$ and $Bmmb$ phases) are shown to have not much variation in migration energy barriers compared to the cubic one. For cubic phase, the energy barrier (0.30 eV) that we obtained falls between the range of previous reports; the activation energy is 0.29 eV by Ahiavi *et al.* [51] and the migration energy barrier is 0.43 eV by Wang *et al.*[159]

3.4 Summary

Thus in this study, we have found the two most energetically and dynamically stable structures of Na_3OCl are $Pnma$ and $P2_1/m$ among the 14 tilted phases at 0 K. The sequence phase change of Na_3OCl with temperature is interesting research to observe its structural stability and its properties with temperatures. Two types of phonon calculations are performed to investigate the phase transition of antiperovskite Na_3OCl . The first one is quasi-harmonic

phonon calculations. When the Gibbs free energies of 14 different polymorphs are calculated with the QHA, the P - T phase diagram shows that three stable phases would appear in the limited scopes of temperature and pressure. At ambient pressure, the high-symmetry cubic phase with $Pm\bar{3}m$ symmetry is expected to be stable at the temperature above 205 K and monoclinic phase with $P2_1/m$ symmetry becomes stable below 135 K. In the temperature range between 135 K and 205 K, $Bmmb$ is expected to be most stable structure. The second one is the inclusion of anharmonic terms in the phonon calculations by using quartic and cubic IFCs. The phase transition temperatures (T_C) are calculated with the basic self-consistent phonon calculations (SC1) as well as the temperature-dependent phonon band structures calculated with additional consideration of the bubble self-energy term (QP-NL). Since the latter method corrects the overestimation of soft mode frequency, more than twice of phase transition temperature is expected using the former one (54 - 86 K vs 166 - 195 K). The effect of thermal expansion on T_C is not significant in cubic Na₃OCl. Nonetheless, our method shows that the behavior of the soft mode upon lattice constant change could play a critical role in the theoretical determination of thermal expansion effects on T_C . The overall results are consistent with the previous computational report on halide perovskite α -CsPbBr₃ and experimentally confirmed room temperature stability of cubic Na₃OCl. For the three vibrationally stable phases, we calculated migration energy barriers of Na vacancy, and found that the energy barriers falling in the range from 0.30 to 0.34 eV are not much different in phases.

Chapter 4

Unveiling the structure and ions dynamics of amorphous $\text{Na}_{3-x}\text{OH}_x\text{Cl}$ antiperovskite electrolytes

4.1 Motivation

Over the past decade, low-melting-point Li- and Na-rich antiperovskite solid electrolytes (SEs) have been targeted worldwide as promising materials for solid-state batteries because of their structural flexibility, high ionic conductivity, wide electrochemical window, and stability.[160–164] In particular, sodium oxyhalide and hydroxyhalide antiperovskites hold the potential to be used in the SEs domain due to their low melting point ($T_m < 300$ °C), affordable cost and low environmental impact of the constituent elements (Na, H, O, and Cl), and rapid synthesis.[165] By exploiting their versatile structure, expressed as X_3OA ($\text{X} = \text{Li}^+$ or Na^+ ; $\text{A} =$ halides (Cl^- , Br^- , I^-) or other anions (BH_4^- , NO_2^-)), the properties, performance and ion dynamics mechanisms of antiperovskite SEs can be tailored through chemical doping, defect tuning, and structural manipulation, thereby providing an exploitable multifaceted chemistry.[160, 166–174] By virtue of aliovalent doping or via mixed hydroxides, Li-rich antiperovskites have been shown to yield superionic ion conductivities, i.e. ~ 0.1 mS/cm.[165, 175] Beyond the stoichiometric X_3OA crystalline systems, attention has been drawn to the use of cation- and anion-doped X_3OA as well as glassy (or amorphous) antiperovskite electrolytes.[166, 176, 177] Glassy Li_3OCl - and Na_3OCl -based antiperovskites have been originally exploited by the teams of Braga and Goodenough, showing a glass transition temperature in the range 390-450 K and a conductivity of the order of 10^{-2} S/cm at room temperature.[178–180] However, attempts at reproducing the original laboratory

synthesis were not conclusive and, to date, structure and ion conduction mechanism of glassy antiperovskite electrolytes remain unsolved issues. [160, 176, 181]

The original work of Braga et al.[178] was later questioned by Hanghofer et al.[181], who ascribed the high conductivity of Li^+ ions to the presence of impurity and stability of the sample, and the formation of $\text{LiCl}\cdot\text{H}_2\text{O}$ to the presence of H_2O . The results of Ref.[178] have been substantiated by *ab initio* and classical molecular dynamics (MD) simulations agreeing on the existence of a subnanoscale phase separation of Li_3OCl into Li_2O and LiCl phases together with an intermixed phase. The formation of such subnanoscale separation was considered to be the promoter of the high conductivity of Li ions as well as a non-negligible Cl ions mobility.[182]

Successful use of an electrolyte composite was recently reported by Tian et al..[45, 183, 184] In this application, an amorphous Li_3OCl was used as a matrix embedding $\text{Li}_{6.75}\text{La}_3\text{Zr}_{1.75}\text{Ta}_{0.25}\text{O}_{12}$ garnet-type oxide particles exhibiting a high room temperature conductivity of $2.27\cdot 10^{-4} \text{ S}\cdot\text{cm}^{-1}$ and an extremely wide electrochemical stability window up to 10 V. In this particular case, the added value promoted by the amorphous X_3OA phase was the ability to act as a binder and filling agent ensuring the formation of an integrated composite SE with a continuous widespread ionic conductive network. The key role of the amorphous phase was also assigned to the excellent affinity to the lithium metal, greatly decreasing the interfacial resistance between the anode and the electrolyte.[45, 183, 184]

A detailed understanding of the atomic structure is a key step to further capture the details of the transport mechanisms behind its conductivity performance. Recent reviews on the use of anti-perovskites for solid-state batteries underlined the limited nature of the available structural characterization and pointed out the severe need of a quantitative structural assessment to avoid any misinterpretation of the correlations between structure and performances.[160, 185, 186] Overall, structure and ion dynamics mechanisms are well known for crystalline X_3OA compounds. This is not the case for amorphous antiperovskites, especially in both hydrogen-free and hydroxylated phases (e.g., oxyhalide X_3OA vs. hydroxyhalide $\text{X}_{3-x}\text{OH}_x\text{A}$).

In view of these considerations, this work relies on predictive atomic-scale modelling, as first-principles molecular dynamics (FPMD), to elucidate the structure and transport properties of amorphous H-free and hydroxylated $\text{Na}_{3-x}\text{OH}_x\text{Cl}$ systems. In terms of structural analysis, we provide a detailed study of both X-rays and neutrons structure factors. If the X-ray probe is of high importance, neutron studies are particularly needed in the case of antiperovskite electrolyte investigation, being capable of detecting low-Z elements (or light elements, such as H and Li) that are out of reach of X-ray (synchrotron source) techniques.[160, 161, 176]

Our paper is organized as follows. Sec. 2 describes the methodologies and models systems

employed within first-principles molecular dynamics. We give details on the production of the amorphous systems allowing for the calculation of static and dynamical properties. A specific subsection is devoted to a set of definitions for quantities (ionic diffusion and conductivities) targeted in this work for their potential applications in the solid-state electrolyte. Results are presented in Sec. 3 and separated into two subsections, the first one (3.1) devoted to structural properties and the second one (3.2) to dynamical properties. The analysis of the structural properties features, firstly, calculated properties in reciprocal and real space (3.1.1 and 3.1.1), namely the structure factors and the pair correlation functions. The following parts are devoted to the analysis of the coordination numbers (3.1.3) and the structural units (3.1.4), with special attention paid to the chemical nature of the various motifs and their variations with the composition.

Subsection 3.2 is organized into three parts, describing respectively the different trends taken by the mean square displacements (3.2.1), a dynamical structural rearrangement involving the hydroxyl group (the “paddlewheel” effects, 3.2.2), and the behavior of the diffusion coefficients (3.2.3) leading to the assessment of the ionic conductivity (3.2.4). Concluding remarks are collected in Sec. 4.

4.2 Calculation methodology and models

4.2.1 Producing $\text{Na}_{3-x}\text{OH}_x\text{Cl}$ amorphous models at 300 K

The Car-Parrinello (CP) method[187] was used to produce dynamical trajectories of the targeted $\text{Na}_{3-x}\text{OH}_x\text{Cl}$ systems. The exchange-correlation functional selected is the generalized gradient approximation (GGA) proposed by Perdew, Burke and Ernzerhof (PBE).[188] The valence-core interaction was described by numerical norm-conserving Troullier-Martins (TM)[189] pseudopotentials for all elements (Na, O, H, and Cl). In the case of Na, semi-core states were included to ensure a good description of the energetics and electronic features dependent on its cationic nature. This amounts to electronic configurations He $2s^2, 2p^6, 3s^1$ for Na; He $2s^2, 2p^4$ for O; $1s^1$ for H and Ne $3s^2, 3p^5$ for Cl. Valence electrons are treated explicitly and represented on a plane-wave basis set with the sampling of the Brillouin restricted to the Γ point. A fictitious electron mass of 600 a.u. and a time step of 0.12 fs ensured optimal conservation of the constants of motion. FPMD simulations were performed in the canonical NVT ensemble with the ionic temperature controlled with a Nose-Hoover [190–192] thermostat chain.[193] For the simulations performed at high temperature (>1000 K) we used a Blochl-Parrinello electronic thermostat [194] with a target kinetic energy of 0.1 a.u. to control the fictitious motion of the electronic degrees of freedom. Our FPMD

approach [187] has been extensively used and benchmarked in the last decades and contributed to the improvement of our understanding of both the physical and chemical properties of chalcogenide and chalcogen halide glasses,[195–197] hybrid[198] and porous[199] systems, and nanomaterials.[200–202]

The Na_3OCl glass model was generated by quenching from the melt. The initial configuration consisted of a Na_3OCl crystal cubic unit cell replicated $3 \times 3 \times 3$ times to obtain a 135 atoms model (81 Na, 27 O, and 27 Cl) in a cubic simulation cell of side 13.6148 Å.[203] The initial box was expanded by 15% with respect to crystal density in order to ease melting at a high temperature. A similar approach was followed for the case of glassy Li_3OCl . [182] Periodic boundary conditions were applied throughout. The model underwent a thermal cycle via canonical NVT simulations, according to the following protocol: 1.3 ps at $T = 300$ K, 1.2 ps at $T = 1200$ K, 3.1 ps at $T = 1500$ K, 46.5 ps at $T = 1800$ K, 38.6 ps at $T = 1000$ K, 33.7 ps at $T = 750$ K and 35 ps at $T = 300$ K (see Fig. 1). At the end of the cycle of $T = 300$ K, the density of the system was set to 2.04 g/cm^3 (corresponding to a final volume expansion of +5% with respect to the crystal phase) in order to reduce the stress tensor to values very close to 0 GPa. Along the thermal cycle the energy cutoff for the plane wave expansion was $R_{Ec} = 80$ Ry. This value was increased at $T = 300$ K ($R_{Ec} = 160$ Ry) to achieve convergence of the stress tensor. By using the final configuration of amorphous Na_3OCl at $T = 300$ K, we randomly replaced the proper amount of Na atoms with H atoms to obtain $\text{Na}_{2.5}\text{OH}_{0.5}\text{Cl}$ and Na_2OHCl (corresponding to $\sim 17\%$ and $\sim 33\%$ of Na replaced, respectively). These systems undertook a thermal cycle via canonical NVT simulations with the following time schedule: 20 ps at $T = 1800$ K, 22 ps at $T = 1000$ K, 19 ps at $T = 750$ K, and 30 ps at $T = 300$ K. To obtain vanishing pressure at $T = 300$ K, the density of the system was set to 1.93 g/cm^3 ($\text{Na}_{2.5}\text{OH}_{0.5}\text{Cl}$), and 1.75 g/cm^3 (Na_2OHCl) (Fig. 1 inset). In what follows, the results on the atomic structure are presented as time-average values over the last 20 ps of the thermal cycles at $T = 300$ K. For all the simulations done here, we used the developer version of the CPMD package.

4.2.2 Dynamical simulations at finite temperatures

FPMD simulations allow to assess the transport properties of mobile ions in amorphous materials.[204, 205] In this work, the ions dynamics and transport properties were studied at different temperatures, specifically $T = 300$ K, 450 K, 600 K, 800 K, 1000 K, and 1200 K (Na_3OCl only). The three systems were equilibrated in the NVT canonical ensemble for a total simulation time of ~ 30 ps. Trajectories were collected every 20 fs. The mean square

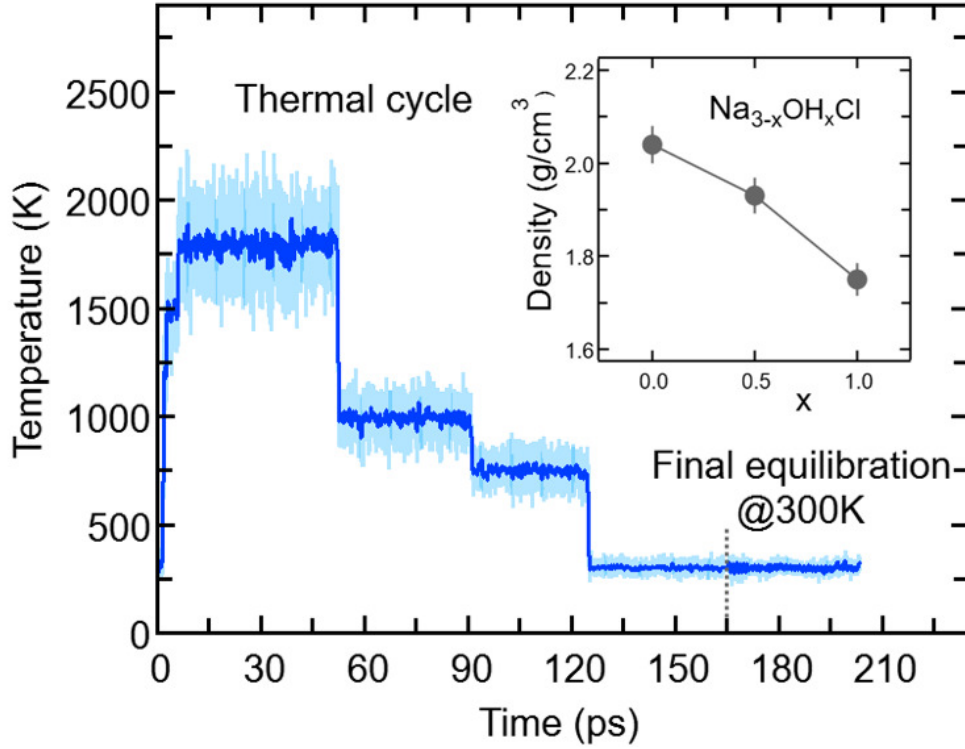


Figure 4.1: Temperatures along the thermal cycle for amorphous Na_3OCl : light blue line, instantaneous T values; blue line, T values sliding average with a window of 0.1 ps. The dashed vertical grey line sets the time at which optimization of the volume at $T = 300\text{K}$ and 0 GPa was implemented. Inset: final density values optimized at $T = 300\text{K}$ for the three $\text{Na}_{3-x}\text{OH}_x\text{Cl}$ models. Error bars are estimated with tests at different volume performed on several final configurations (300K) to obtain a final stress tensor close 0 GPa.

displacements (MSD) of all ions were computed according to

$$\langle r^2(t) \rangle = \left\langle \sum_{i=1}^N |r_i(t) - r_i(0)|^2 \right\rangle = \left\langle \sum_i (\Delta \mathbf{R}_i(t))^2 \right\rangle \quad (4.1)$$

where N is the number of the atoms of interest and $\left\langle \sum_i (\Delta \mathbf{R}_i(t))^2 \right\rangle$ is the MSD averaged on all realizations of Eq. (4.1) for a given value of the time t . It should be noted that in its standard definition the mean square displacement is normalized to the number of particles, say N , so as to appear as an intensive property resulting from an average over the whole system. However, for sake of convenience, we prefer to take advantage of a definition of MSD taking the form of Eq. (4.1). To assess the so-called tracer diffusive D^* behavior of the ions, MSD is

analysed in log-log plots via the slopes $\beta(t)$ as a function of time,

$$\beta(t) = \frac{d \log \langle \sum_i (\Delta \mathbf{R}_i(t))^2 \rangle}{d \log t} \quad (4.2)$$

At very short t , a value of $\beta(t)$ equal to two is expected, corresponding to a free, ideally ballistic, motion of the ions, while at very long times, $\beta(t)$ should reach a value equal to one, corresponding to a real diffusive regime, with the MSD growing linearly with time. We would like to stress here that this analysis is crucial to determine the effective achievement of diffusive behavior and identify the portion of the MSD plot that should be used to extract diffusion coefficients. This is particularly important in the case of disordered materials such as glasses,[206] ionic liquids,[207] and molten salts.[208] In the present work, the lower and upper bounds of the real diffusive regime were defined within the interval delimited by (lower boundary) the t at which $\beta(t)$ reaches a value of one up to (upper boundary) the value of t corresponding to a length of trajectory 15% shorter than the total one.[209] For the systems that reach the diffusive regime at a given temperature, the ions diffusion coefficients (e.g. tracer diffusivity) were calculated by using the Einstein relation given by:[210, 211]

$$D^* = \lim_{t \rightarrow \infty} \frac{1}{N2d} \frac{\partial \langle r^2(t) \rangle}{\partial t} \simeq \frac{\sum_i \langle \Delta \mathbf{R}_i^2 \rangle}{N2dt} \quad (4.3)$$

where d is the dimensionality factor ($d = 3$ for three dimensional systems) and we have dropped the explicit dependence on time in Eq. (4.3) as a result of the infinite t limit. When the diffusive regime is reached, the Arrhenius equation can be used to calculate the activation energy E_a barrier for diffusion (conductivity) by fitting the data of $\log D^*$ ($\log \sigma^*$) vs. $1/T$ as:

$$D^* = D_0 \exp\left(-\frac{\Delta E_a}{kT}\right) \quad (4.4)$$

From the tracer diffusivity D^* , the idealized ionic conductivity can be calculated based on the Nernst-Einstein relation:

$$\sigma^* = D^* \frac{Nq^2}{VkT} = \frac{q^2}{2dVkT} \sum_i \langle \Delta \mathbf{R}_i^2 \rangle \quad (4.5)$$

where V is the total volume of the model system, q is the charge of mobile-ion species, T is temperature, k is the Boltzmann constant. A more accurate estimation of the relevant

conductivity is instead given by the Einstein formulation of the net charge migration as:

$$\sigma_{ion} = D_{\sigma} \frac{Nq^2}{VkT} = \frac{q^2}{2dVkT} \left\langle \left(\sum_i \Delta \mathbf{R}_i \right)^2 \right\rangle \quad (4.6)$$

The charge-diffusion coefficient D_{σ} , which refers to the displacement of the center of mass of all the diffusing ions and is used here to consider possible correlation effects, is defined as:

$$D_{\sigma} = \frac{\left\langle (\sum_i \Delta \mathbf{R}_i)^2 \right\rangle}{2dNt} = \frac{\sum_i \langle \Delta \mathbf{R}_i^2 \rangle}{2dNt} + \frac{\sum_i \sum_{ii \neq i} \langle \Delta \mathbf{R}_i \Delta \mathbf{R}_{ii} \rangle}{2dNt} \quad (4.7)$$

where d is the dimension of lattice where diffusion takes place and N refers to the number of diffusing ions.[212–215] The numerator on the left-hand side was split into a self-diffusion part and a distinct-ion part, the latter accounting for correlations between the movements of distinct ions of the same type (i.e. Na ions).

The Haven ratio is a measure of the degree by which the trajectories of different atoms are correlated to each other.[212, 216] For single ion conductors, it is

$$H_R^{\sigma} = \frac{D^*}{D_{\sigma}} \quad (4.8)$$

becoming equal to one in the absence of any correlation between different diffusing atoms. This is asymptotically approached in the dilute limit, where diffusing atoms rarely encounter each other during their motion through a crystal. If distinct ions move preferentially in the same direction (positive correlation), then $H_R > 0$ and $H_R < 1$, which is usually observed for single-ion conductors.[215, 217–219] At non-dilute concentrations, as in the majority of the solid electrolytes, positive correlations between different diffusing ions become particularly relevant, resulting in $H_R < 1$, whereas negative correlations between different diffusing ions (distinct ions move preferentially in the opposite directions) give $H_R > 1$. To consider all types of ions correlations (positive and negative) involved in the system, namely cation-cation correlations (σ_{++}^{dist}), anion-anion correlations (σ_{--}^{dist}) and cation-anion correlations (σ_{+-}^{dist}) contributing to the Haven ratio, the following equation is used:

$$\begin{aligned} H_R^{tot} &= \frac{\sigma^{*tot}}{\sigma_{ion}^{tot}} = \frac{\sigma_+^{self} + \sigma_-^{self}}{\sigma_{ion}^{tot}} \\ &= \frac{\sigma_{Na}^{self} + \sigma_O^{self} + \sigma_{Cl}^{self}}{\sigma_{Na,O,Cl}^{self} + \sigma_{NaNa,OO,ClCl}^{dist} + 2\sigma_{NaCl,NaO,ClO}^{dist}} \end{aligned} \quad (4.9)$$

where

$$\sigma_{ion}^{tot} = \frac{q^2}{2dVkT} \left\langle \left(\sum_i^N z_i \Delta \mathbf{R}_i \right)^2 \right\rangle \quad (4.10)$$

$$\sigma_A^{self} = \frac{q^2 z_A^2}{2dVkT} \sum_i \langle \Delta \mathbf{R}_i^2 \rangle \quad (4.11)$$

$$\sigma_{AA}^{dist} = \frac{q^2 z_A^2}{2dVkT} \sum_{ii \neq i} \langle \Delta \mathbf{R}_i \Delta \mathbf{R}_{ii} \rangle \quad (4.12)$$

$$\sigma_{AB}^{dist} = \frac{q^2 z_A z_B}{2dVkT} \left(\sum_i \Delta \mathbf{R}_i \sum_j \Delta \mathbf{R}_j \right) \quad (4.13)$$

N is total number of ions in the electrolyte, and z_i is the charge number of ion i .^[207] The sum in Eq. (10) can be re-expressed as shown in Eqs. (11)–(13). H_R^σ is computed by considering correlation effects only promoted by Na ions whereas with H_R^{tot} the contribution of possible correlation effects due to O and Cl ions are also taken into account. These equations are an alternative to the methods based on quantifying collective correlated effects by integration of the ions velocities autocorrelation functions.^[220–222]

4.3 Result and discussion

4.3.1 Structural properties

Total X-rays and neutrons and structure factors

The total X-rays and neutrons structure factors ($S_T^X(k)$ and $S_T^N(k)$, respectively) can be directly calculated on the equilibrium trajectory in the reciprocal space.^[223, 224] Alternatively, $S_T^X(k)$ can be obtained by Fourier transform (FFT) of the real space total pair correlation function $g_{tot}(r)$. We underline that the calculation of $S_T(k)$ directly in the k -space is, generally, to be preferred over the Fourier transform (FFT) of the real-space pair distribution functions, since the former approach avoids the effects of the finite range of integration. However, the FFT procedure is currently adopted in the literature to smooth out the noise affecting the structure factors computed directly in reciprocal space, especially in the case of glassy configurations at room temperature. In the present work, we employed the FFT method and the calculated $S_T^X(k)$ and $S_T^N(k)$ are shown in Fig. 2.

In the following, we analyze X-rays and neutrons FFT $S_T(k)$ in terms of peaks positions and intensities comparing the three $\text{Na}_{3-x}\text{OH}_x\text{Cl}$ systems. We remark that $S_T^X(k)$ of Na_3OCl features a first peak at about $k \sim 2.5 \text{ \AA}^{-1}$ with a shoulder at $k \sim 2.0 \text{ \AA}^{-1}$ and a second peak

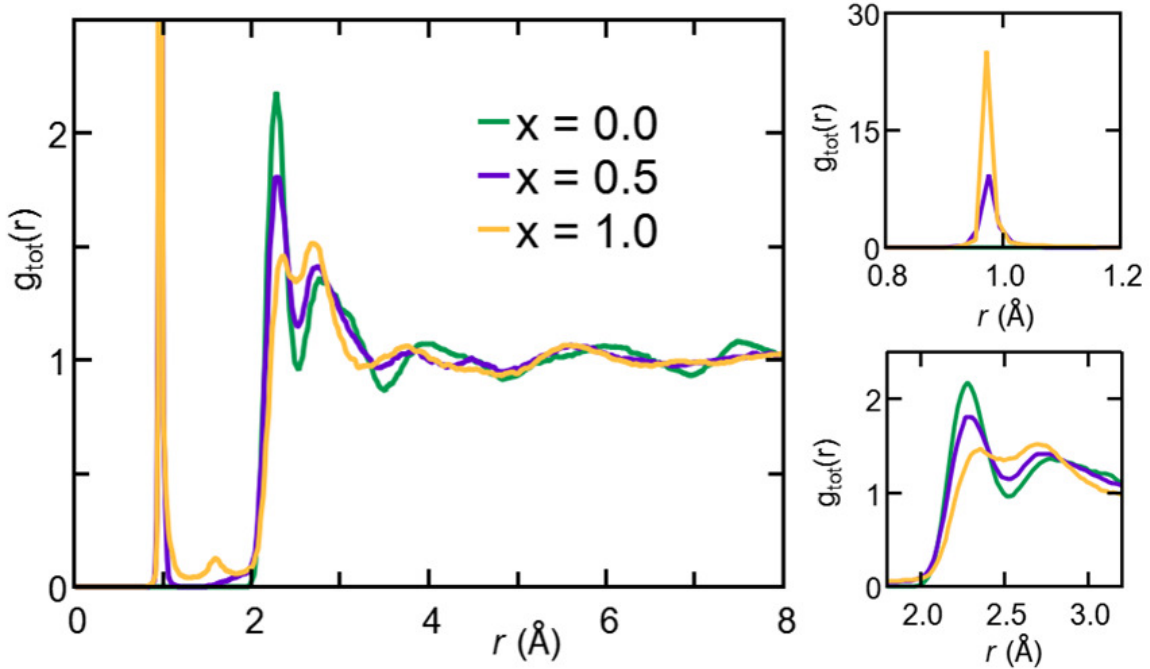


Figure 4.2: Left: Total pair correlation functions for amorphous $\text{Na}_{3-x}\text{OH}_x\text{Cl}$ ($x=0$, $x=0.5$, $x=1$) obtained at $T = 300$ K. Right: Zoom-in into the $0.8\text{-}1.2$ Å (top) and $1.8\text{-}3.2$ Å (bottom) ranges.

at $k \sim 3.5$ Å⁻¹. These first two peaks are followed by much broader maxima and minima and rapidly damped oscillations up to $k \sim 8.0$ Å⁻¹. $\text{Na}_{2.5}\text{OH}_{0.5}\text{Cl}$ and Na_2OHCl $S_T^X(k)$ have very similar profiles and minor differences with respect to pristine Na_3OCl . In contrast, while the X-rays structure factor $S_T^X(k)$ exhibits similarities across all three cases, the neutron structure factor $S_T^N(k)$ displays significant distinctions, indicating that it may be a better diagnostic tool for discerning models containing varying amounts of hydrogen. Higher intensities are found in $S_T^N(k)$ for Na_3OCl . By increasing x , maxima and minima are reduced and different profiles appear in between $k \sim 2$ Å⁻¹ and $k \sim 4$ Å⁻¹ to signify a lower degree of structural organization. The relatively small peak at about $k \sim 1$ Å⁻¹ reveal that the intermediate range order is very limited in these amorphous systems. Overall, Fig. 2 is indicative of modifications taking place within the networks affecting an ordered structural sequence made of distinct shells of neighbors.

Table 4.1: Upper part: nearest-neighbour interatomic distances r_{ij} (in Å) identified by the position of the first maximum of the pair correlation functions $g_{ij}(r)$. We also give the first peak full width at half maximum (FWHM). For comparison, we report the values of the crystalline Na_3OCl phase obtained by experiments.[203, 225] Lower part: total and pair coordination numbers as defined by taking different cutoff radii for the definition of a total or a “cation-anion” shell of interactions (see Sec. 4.3.1). Values in parenthesis correspond to the statistical uncertainty on the last reported digits.

	Exp.[203, 225]	FPMD, this work		
	Crystal	Na_3OCl	$\text{Na}_{2.5}\text{OH}_{0.5}\text{Cl}$	Na_2OHCl
r_{NaO}	2.25	2.28(2)	2.27(2)	2.32(2)
FWHM		0.28	0.31	0.33
r_{NaCl}	3.18	2.75(2)	2.75(3)	2.74(4)
FWHM		0.47	0.46	0.52
r_{NaNa}	3.18	3.14(3)	3.22(4)	3.34(4)
FWHM		0.92	1.01	1.02
r_{OO}	4.50	3.85(1)	3.72(4)	3.61(4)
FWHM		0.86	0.77	0.72
r_{OCl}	3.89	4.00(4)	3.91(2)	3.78(4)
FWHM		0.79	1.00	0.93
r_{ClCl}	4.50	4.06(3)	3.87(3)	4.05(3)
FWHM		0.82	1.04	1.01
r_{OH}	-	-	0.98(2)	0.97(2)
FWHM	-	-	0.02	0.02
n_{Na}^t	14	8.01(3)	7.26(2)	6.04(2)
n_{Na}^p	6	4.0(1)	4.30(1)	4.58(2)
n_{O}^t	6	6.30 (2)	6.44(2)	6.09(4)
n_{O}^p	6	6.29 (3)	5.94(2)	5.40(2)
n_{Cl}^t	12	5.73(3)	5.45(2)	4.93(3)
n_{Cl}^p	12	5.72(1)	5.37(1)	4.78(3)
n_{H}^t	-	-	1.00(2)	1.02(3)

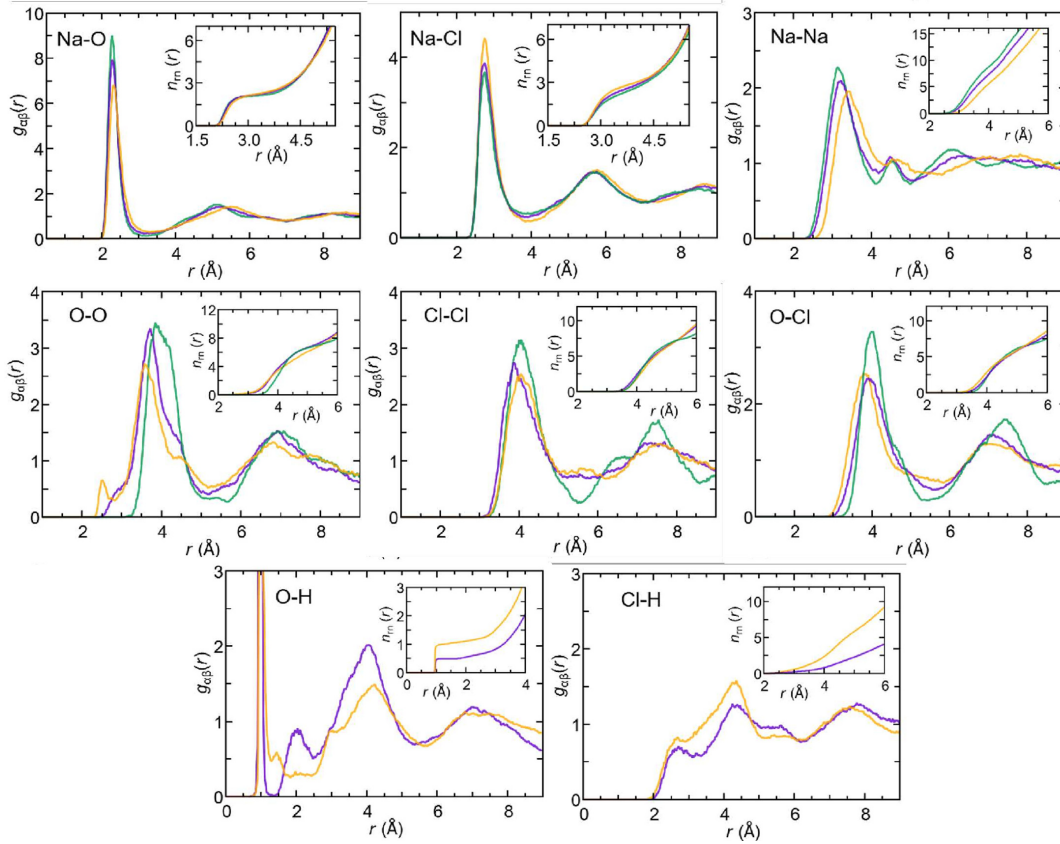


Figure 4.3: Partial pair correlation functions $g_{\alpha\beta}(r)$ for amorphous $\text{Na}_{3-x}\text{OH}_x\text{Cl}$ ($x=0$, $x=0.5$, $x=1$) at $T = 300$ K relative to the pairs Na-O, Na-Cl, Na-Na, O-O, Cl-Cl, O-Cl, O-H, and Cl-H. The running integrals over the interatomic distance are shown.

Total and partial pair-correlation functions

The total and partial pair correlation functions for the $\text{Na}_{3-x}\text{OH}_x\text{Cl}$ ($x=0$, $x=0.5$, $x=1$) systems are shown in Fig. 3 and 4, respectively. In terms of total pair correlation functions, the H-free Na_3OCl one shows a first narrow peak centered at ~ 2.28 Å (with a full width at half maximum (FWHM) of 0.28 Å) and a broader second peak at a lower intensity at ~ 2.77 Å (FWHM of 0.47 Å). These two peaks are present also in the hydroxylated systems, although with a lower ratio between the intensities for $\text{Na}_{2.5}\text{OH}_{0.5}\text{Cl}$, whereas similar values are observed in Na_2OHCl . As expected, the presence of H leads to a very sharp peak at about ~ 0.98 Å, with FWHM of 0.02 Å. In addition, there is a very small maximum in Na_2OHCl at ~ 1.5 Å. Analyzing the partial pair correlation functions $g_{\alpha\beta}(r)$ (Fig. 4) allows us to trace back the role of each individual pair contribution with respect to the total one. In Tab. 1 we report the nearest-neighbor distances r_{ij} identified by the position of the first maximum of the $g_{\alpha\beta}(r)$ for the three $\text{Na}_{3-x}\text{OH}_x\text{Cl}$ systems. For comparison, we also report the nearest-neighbor

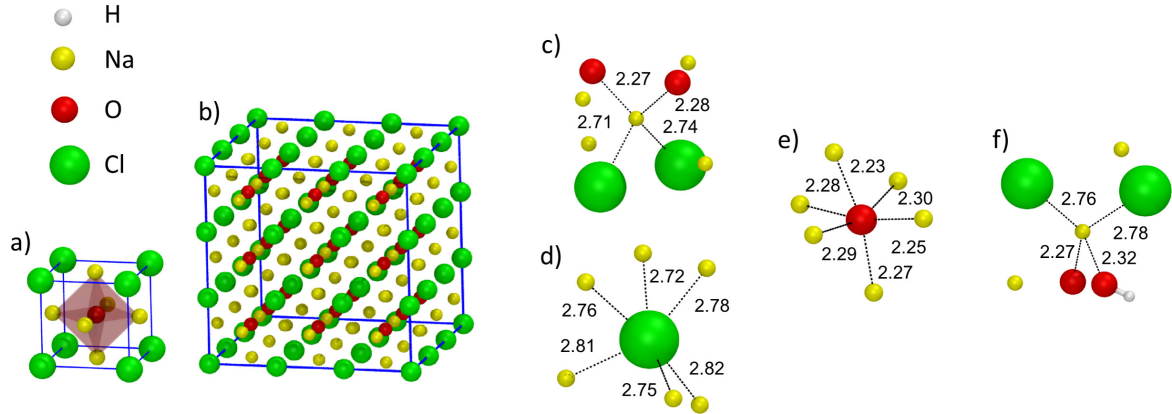


Figure 4.4: a) Representation of the unit cell of crystalline Na_3OCl . The red polyhedra identify the octahedron O site. b) Crystalline supercell of 135 atoms (unit cell replicated $3 \times 3 \times 3$). c-e) Coordination units for Na, O, and Cl found in amorphous Na_3OCl at $T = 300$ K: a fourfold Na atom (O_2Cl_2) (c), a sixfold Cl atom (d), a sixfold O atom (e). f) A Na atom found in amorphous $\text{Na}_{2.5}\text{OH}_{0.5}\text{Cl}$ coordinated by at least an O atom as a hydroxyl group. Counterions interatomic bonds are identified by a dashed line with the corresponding values. We show the atoms within a radial cutoff of 3.3 \AA . Color legend: Na, yellow; O, red; Cl, green; H, white.

distances found in synthesized pure crystalline Na_3OCl .^[174, 225] The first peak of $g_{\text{tot}}(r)$ for amorphous Na_3OCl can be ascribed entirely to the Na-O pair ($\sim 2.28 \text{ \AA}$), whereas the second peak is mainly attributed to the Na-Cl pair ($\sim 2.75 \text{ \AA}$) and only partially to Na-O and Na-Na ($\sim 3.14 \text{ \AA}$) $g_{\alpha\beta}(r)$ contributions. The first peak of $g_{\text{NaNa}}(r)$ is responsible for the shoulder occurring after the second peak ($\sim 2.8\text{-}3.1 \text{ \AA}$) found in the total pair correlation function. Analyzing the peak positions of $g_{\text{NaO}}(r)$ for amorphous Na_3OCl , the Na-O bond distance is found slightly larger than the typical ionic bond reported for crystalline Na_3OCl ($\sim 2.25 \text{ \AA}$), whereas the Na-Cl ionic bond distance is shorter than that of crystalline one ($\sim 3.18 \text{ \AA}$). The partial pair correlation functions $g_{\text{NaO}}(r)$, $g_{\text{NaCl}}(r)$ and $g_{\text{NaNa}}(r)$ of the two hydroxylated systems are quite similar to those of Na_3OCl . However, the intensities of the first peaks in $g_{\text{NaO}}(r)$ and $g_{\text{NaNa}}(r)$ are reduced in accordance with the lower content of Na atoms (in favor of H atoms) whereas the corresponding intensity in $g_{\text{NaCl}}(r)$ is increased. Replacing part of Na atoms with H atoms causes an elongation of the Na-O distance in Na_2OHCl ($\sim 2.32 \text{ \AA}$ for $\sim 33\%$ of Na atoms replaced) while no effect is found in the Na-O distance for $\text{Na}_{2.5}\text{OH}_{0.5}\text{Cl}$ ($\sim 2.27 \text{ \AA}$ for $\sim 17\%$ of Na atoms replaced). On the contrary, Na-Cl bond distances found in $\text{Na}_{2.5}\text{OH}_{0.5}\text{Cl}$ and Na_2OHCl are the same as in Na_3OCl ($\sim 2.75 \text{ \AA}$). $g_{\text{NaNa}}(r)$ shows a slight increase of the Na-Na nearest-neighbour interatomic distances with increasing H content (up to $\sim 3.34 \text{ \AA}$ when $\sim 33\%$ of Na is substituted). The two hydroxylated systems are affected by

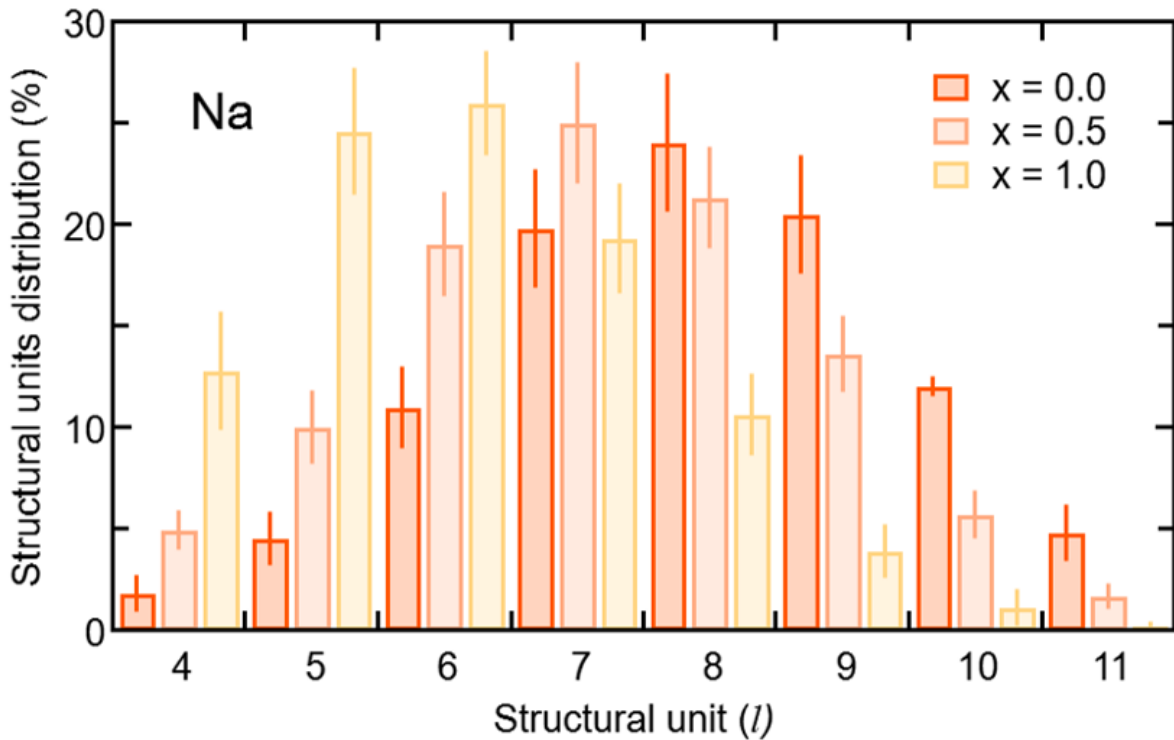


Figure 4.5: Distributions of the structural units for Na of amorphous $\text{Na}_{3-x}\text{OH}_x\text{Cl}$ ($x=0$, $x=0.5$, $x=1$) as a function of the number of neighbors in each unit (l). Values obtained by using the definition of "total" coordination n_{ij}^t , given in Sec. 4.3.1.

a greater degree of disorder in comparison with Na_3OCl as confirmed by a less pronounced minimum separating the peaks in $g_{\text{NaNa}}(r)$.

The $g_{\text{OH}}(r)$ partial pair correlations functions of $\text{Na}_{2.5}\text{OH}_{0.5}\text{Cl}$ and Na_2OHCl show that all H atoms are bonded to O atoms, forming OH hydroxyl groups with typical O–H bond distance equal to ~ 0.98 Å. This observation is further supported by the analysis of $g_{\text{ClH}}(r)$, for which the Cl–H interatomic distance lies at values higher than ~ 2.0 Å for both the hydroxylated phases, much larger than typical Cl–H bond distance, i.e. ~ 1.3 Å. For what concerns $g_{\text{OH}}(r)$, a few differences can be pointed out between the two hydroxylated phases. In $\text{Na}_{2.5}\text{OH}_{0.5}\text{Cl}$, a second peak exists at about ~ 2.0 Å which reflects the presence of a H-bonding network promoted between neighboring hydroxyl groups or free oxygen atoms in the form of $\text{OH}\cdots\text{OH}$ and $\text{OH}\cdots\text{O}$ interactions, respectively. In Na_2OHCl , such a peak is minimally visible but a small peak at a shorter distance (~ 1.5 Å) is discernible. This latter peak is the one that generally identifies H atoms (or protons) hopping between neighboring hydroxyl groups and giving rise to stable or metastable water molecules.[226–231] In terms of

anion-anion pair correlation functions, all three $g_{\text{OO}}(r)$, $g_{\text{ClCl}}(r)$ and $g_{\text{OCl}}(r)$ are characterized by a first main peak centered at around $\sim 3.7\text{-}4.0$ Å. There are interesting differences to be pointed out when comparing $g_{\text{OO}}(r)$ for the three $\text{Na}_{3-x}\text{OH}_x\text{Cl}$ models. In particular, Na_3OCl exhibits a relatively broad first peak at ~ 3.85 Å (FWHM of ~ 0.86 Å) whereas the two hydroxylated models feature intense peaks at ~ 3.72 Å and ~ 3.61 Å (FWHM of ~ 0.77 Å and ~ 0.72 Å, respectively) followed by a shoulder centered at about ~ 4.5 Å. Also, worth of notice is a small peak at ~ 2.5 Å for $\text{Na}_{2.5}\text{OH}_{0.5}\text{Cl}$ and a shoulder at about ~ 2.9 Å for $\text{Na}_{3-x}\text{OH}_x\text{Cl}$ while in the case of Na_3OCl $g_{\text{OO}}(r)$ goes to zero for distances < 3.2 Å. In terms of $g_{\text{ClCl}}(r)$ and $g_{\text{OCl}}(r)$, the three models show very similar profiles, although the intensity of the main peak of the two hydroxylated systems is smaller for a higher degree of disorder with respect to Na_3OCl .

Total and partial coordination numbers

More insights into the $\text{Na}_{3-x}\text{OH}_x\text{Cl}$ networks can be obtained by looking at the total and partial coordination numbers (n_i and n_{ij} , respectively), obtained by relying on the pair correlation functions. More precisely, n_{ij} is obtained by integrating the first peak of $g_{ij}(r)$ up to a given cutoff distance corresponding to the position of the first minimum. The total Na, O, Cl, and H coordination numbers are then obtained as follows: $n_{\text{Na}} = n_{\text{NaO}} + n_{\text{NaCl}} + n_{\text{NaNa}} + n_{\text{NaH}}$, $n_{\text{O}} = n_{\text{ONa}} + n_{\text{OH}} + n_{\text{OCl}} + n_{\text{OO}}$, $n_{\text{Cl}} = n_{\text{ClNa}} + n_{\text{ClH}} + n_{\text{OCl}} + n_{\text{ClCl}}$ and $n_{\text{H}} = n_{\text{HO}} + n_{\text{HCl}} + n_{\text{HNa}} + n_{\text{HH}}$. When the first peak of the corresponding $g_{ij}(r)$ is followed by a clear minimum well separated from a second maximum, n_{ij} does not suffer from any ambiguities for its definition, since the running coordination number exhibits a clear plateau (see the behavior in the case of Na-O interactions, inset of Fig. 4). In the opposite case, the determination of n_{ij} is less clearcut (see the Na-Na case in the inset of Fig. 4) and n_{ij} is much more sensitive to the choice of the cutoff. For these reasons, in addition to the individual pair cutoffs taken as the minima after the first peak of $g_{ij}(r)$, we adopted a second cutoff (a "total" one) defined by the minimum after the second peak of $g_{\text{tot}}(r)$. The value found (3.3 Å) is determined as the average between the three amorphous models and it allows us to consider within the first coordination shell of Na atoms all the counter-ions (O and Cl) and a number of neighboring Na atoms. With this procedure, we can compare the coordination numbers of amorphous $\text{Na}_{3-x}\text{OH}_x\text{Cl}$ models to those of the crystalline phase of Na_3OCl . We remind that crystalline Na_3OCl (cubic phase, stable at $T = 300\text{K}$ [174, 203, 225]) is characterized by Na atoms coordinated by six counter-ions (two oxygen and four chlorine atoms) within the nearest-neighbor shell, O atoms are coordinated by six Na atoms and Cl atoms are coordinated by twelve Na atoms. Within the cutoff employed above (3.3 Å) each Na atom has also eight neighboring Na atoms, leading to a "total" Na coordination of 14.[203, 225] Therefore, the local environment of Na in crystalline Na_3OC

can be thought of as made by a total of 14 neighboring atoms, with neighboring Na interacting through O atoms via Na-O-Na linkages (see Fig. 5a). On the basis of these considerations, we performed the analysis of the coordination numbers n_{ij} of amorphous $\text{Na}_{3-x}\text{OH}_x\text{Cl}$ systems by considering the “partial” coordination number n_{ij}^p (definition 1) well adapted to describe the so-called “cation-anion” (i.e. counter-ions) interactions and the “total” coordination number n_{ij}^t (definition 2) that is most appropriate to describe the whole set of Na neighbors. The same distinction has been introduced to obtain the distribution of the structural coordination units characterizing the environment of each atom. For a given number of neighbors l and a given atomic species, one can extract from each configuration the chemical nature of the neighbors, providing a detailed description of the network organization. It is important to underline that a coordination number gives an average behavior stemming from all neighbors with no insight into the detailed chemical nature of bonding, while the information provided by the coordination structural units shows how each atomic species organizes itself when connecting to atoms of the same or of a different kind. To help understanding these definitions, Fig. 5 contains snapshots of the local coordinations of the Na, O, and Cl atoms found in crystalline Na_3OCl as well as typical structural units in amorphous $\text{Na}_{3-x}\text{OH}_x\text{Cl}$ systems issued from our calculations. Also, the insets of Figure 4 show the running integrals of the individual partial correlation function $g_{ij}(r)$ from which we extracted the coordination numbers n_{ij}^t and n_{ij}^p given in Tab. 1. Focusing on the structural units, Fig. 6 provides their distribution in terms of the number l neighbors for Na, on the basis of definition 2. In terms of total number of neighbours of Na atoms (within 3.3 Å), we observe that amorphous Na_3OCl exhibits a markedly distinct behavior when compared to its crystalline counterpart. Specifically, the unit distribution for Na atoms is remarkably wide (from 4 to 11) and centered at $l = 8.0$, with the number of neighboring counter-ions decreasing from six to four, and the number of Na neighbors halved from eight to four. The partial replacement of Na with H atoms induces a shift of the l units distribution surrounding Na atoms to lower values, centered at ~ 7.3 and ~ 6.0 for $\text{Na}_{2.5}\text{OH}_{0.5}\text{Cl}$ and Na_2OHCl , respectively. By using definition 1, the distributions of structural units for Na, O, and Cl that account for what we termed counter-ions interactions are reported in Tab. 2, together with the breakdown of the chemical composition of each structural unit for a given l .

Chemical identification of the structural units for the three compositions

In the case of Na_3OCl , the coordination units given in Tab. 2 are indicative of a first coordination shell for Na essentially fourfold ($\sim 70.0\%$) in terms of cation-anions (i.e. counterions) according to definition 1 (see Sec. 4.3.1). The decomposition in terms of chemical species gives in decreasing order of importance the following units: O_2Cl_2

Table 4.2: Distribution of the individual cation-anion $n_{\alpha}(l)$ structural units where an atom of species α (Na, Cl or O) is l -fold coordinated to a counter ion computed for glassy Na₃OCl (see definition 1, Sec. “Total and partial coordination numbers”). In bold are reported the total percentages determined for each l -fold coordination. These quantities have been calculated including neighbours separated by a cutoff corresponding to the first minimum in the $g_{\alpha\beta}(r)$. For the present work, the individual pair cutoffs used are 3.16, 3.94, 4.10, 5.06, 5.51, and 5.39 Å for, respectively, the Na-O, Na-Cl, Na-Na, O-O, Cl-Cl and O-Cl distances. A total cutoff of 3.30 Å was defined from the total $g(r)$. Error bars are given in parenthesis.

		Proportions $\bar{n}_{\alpha}(l)$ (%)		
		x = 0	x = 0.5	x = 1
Na				
$l=3$		14.6(1.9)	8.4(1.0)	3.5(1.0)
	O ₂ Cl ₁	10.4	4.4	1.3
	O ₃	3.6	2.5	0.6
$l=4$		70.0(2.9)	56.9(2.2)	43.8(2.1)
	O ₂ Cl ₂	36.6	23.8	13.1
	O ₃ Cl ₁	18.1	13.9	14.5
	O ₁ Cl ₃	9.9	11.8	11.0
	O ₄	3.7	5.7	2.6
$l=5$		13.8(1.5)	30.4(1.6)	43.7(2.3)
	O ₂ Cl ₃	5.4	9.7	10.7
	O ₁ Cl ₄	4.4	6.7	11.6
	O ₃ Cl ₂	0.4	7.1	13.2
	Cl ₅	1.5	2.5	1.5
$l=6$		3.3(0.5)	5.5(0.7)	11.1(1.2)
	O ₄ Cl ₂	-	0.3	2.3
	O ₃ Cl ₃	-	1.3	2.3
	O ₂ Cl ₄	0.5	1.0	1.8
	O ₁ Cl ₅	0.2	1.1	1.7
O				
$l=4$		-	<0.5	8.6(1.8)
	Na ₂ H ₂	-	-	2.0
	Na ₃ H ₁	-	0.4	6.6
$l=5$		2.1(2.0)	20.8(3.9)	44.4(6.6)
	Na ₃ H ₂	-	-	5.7
	Na ₄ H ₁	-	16.5	38.6
	Na ₅	1.9	4.3	0.1
$l=6$		69.1(6.6)	63.6(4.9)	44.7(6.9)
	Na ₅ H ₁	-	24.9	36.0
	Na ₆	69.1	38.6	7.3
$l=7$		27.6(6.1)	15.0(3.8)	2.1(1.9)
	Na ₆ H ₁	-	6.1	2.0
	Na ₇	27.6	8.9	-
Cl				
$l=3$	Na ₃ H ₀	-	1.2(1.0)	4.8(3.8)
$l=4$	Na ₄ H ₀	8.2(4.6)	14.2(8.7)	31.5(7.3)
$l=5$	Na ₅ H ₀	31.6(8.0)	40.0(8.6)	45.4(7.4)
$l=6$	Na ₆ H ₀	39.8(9.0)	36.4(7.7)	16.9(6.1)
$l=7$	Na ₇ H ₀	17.1(6.4)	7.7(4.4)	-
$l=8$	Na ₈ H ₀	2.4(1.9)	-	-

($\sim 36.6\%$), O_3Cl_1 ($\sim 18.1\%$), O_1Cl_3 ($\sim 9.9\%$) and O_4 ($\sim 3.7\%$). Threefold and fivefold units correspond to $\sim 14.6\%$ and $\sim 13.8\%$, respectively, with a larger presence of two or one oxygen atoms ($O_2Cl_1 \sim 10.4\%$, $O_2Cl_3 \sim 5.4\%$ and $O_1Cl_4 \sim 4.4\%$). Our results demonstrate that the structure of amorphous Na_3OCl is significantly different from the molecular dynamics model conjectured for glassy Li_3OCl , based on nanophase segregation of regions rich in Li_2O and $LiCl$.^[182] Indeed, by looking at Na atoms fourfold or even fivefold coordinated, in amorphous Na_3OCl only $\sim 7.3\%$ of them are exclusively coordinated to O atoms (O_3 and O_4) and $\sim 1.5\%$ exclusively coordinated to Cl atoms (Cl_5). The value of n_O^t in amorphous Na_3OCl is about ~ 6.3 (Tab. 1), close to the one in crystalline Na_3OCl .^[174, 203, 225] We find $\sim 69.1\%$ of O atoms coordinated by six Na atoms and $\sim 27.6\%$ by seven Na atoms (Tab. 2). For Cl, n_{Cl}^t is equal to ~ 5.7 , almost half of that found in the crystalline phase (12). Several structural units connected to Cl are noticeable in Tab. 2. In fact, $\sim 39.8\%$ of Cl atoms are coordinated by six, $\sim 31.6\%$ by five, $\sim 17.1\%$ by seven and $\sim 8.2\%$ by four Na atoms. Having established the main features of the structural units in Na_3OCl , we can turn to the analogous description for the case of the hydroxylated amorphous materials. In $Na_{3-x}OH_xCl$ we remark a decrease of n_{Na}^t (from ~ 8.0 to ~ 6.0) from the value in Na_3OCl . However, n_{Na}^p does the opposite (from ~ 4.0 to ~ 4.6). The decrease in n_{Na}^t is due to the partial substitution of Na by H, with all the H atoms found coordinated to O atoms, forming in majority hydroxyl OH groups ($n_H^t \sim 1.0$). This is confirmed by the visual inspection of the snapshots relative to $Na_{2.5}OH_{0.5}Cl$ (Figure 4e) where H is bonded to O atoms in the form of a hydroxyl group (O-H bonding distance $\sim 0.98 \text{ \AA}$), with no H-Na bond formation.

In terms of the cation-anion partial coordination, we observe a slight increase of n_{Na}^p , the values being ~ 4.0 for Na_3OCl , ~ 4.3 for $Na_{2.5}OH_{0.5}Cl$ and ~ 4.6 for Na_2OHCl . Correspondingly, the distribution of the structural units given in Tab. 2 reveals that the percentage of Na atoms fourfold coordinated decreases (from $\sim 70.0\%$ to $\sim 56.9\%$ and $\sim 43.8\%$, respectively) with a concomitant increase of the fivefold ones (from $\sim 13.8\%$ up to $\sim 30.4\%$ and $\sim 43.7\%$). The larger amount of fivefold Na-centered units at the expenses of fourfold ones can be traced back to a concomitant decrease of the number of O_2Cl_2 units (from $\sim 36.6\%$ to $\sim 23.8\%$ and $\sim 13.1\%$) and a net increase of the O_2Cl_3 , O_1Cl_4 and O_3Cl_2 units (the latter from $\sim 0.4\%$ to $\sim 7.1\%$ and $\sim 13.2\%$).

Worth of notice is the behavior of the total and partial coordination numbers of O atoms. n_O^p decreases from ~ 6.3 in Na_3OCl to ~ 5.9 and ~ 5.4 for $Na_{2.5}OH_{0.5}Cl$ and Na_2OHCl , respectively. This decrease is due to a clear increase of lower coordinated units of O at the expenses of the higher-coordinated units. Na_2OHCl shows a minimal content of $l = 7$ units and a comparable content of $l = 5$ and $l = 6$ units ($\sim 44\%$ versus $\sim 45\%$). The trend in the local environment of O in the hydroxylated phases results from the fact that in $Na_{2.5}OH_{0.5}Cl \sim 52\%$

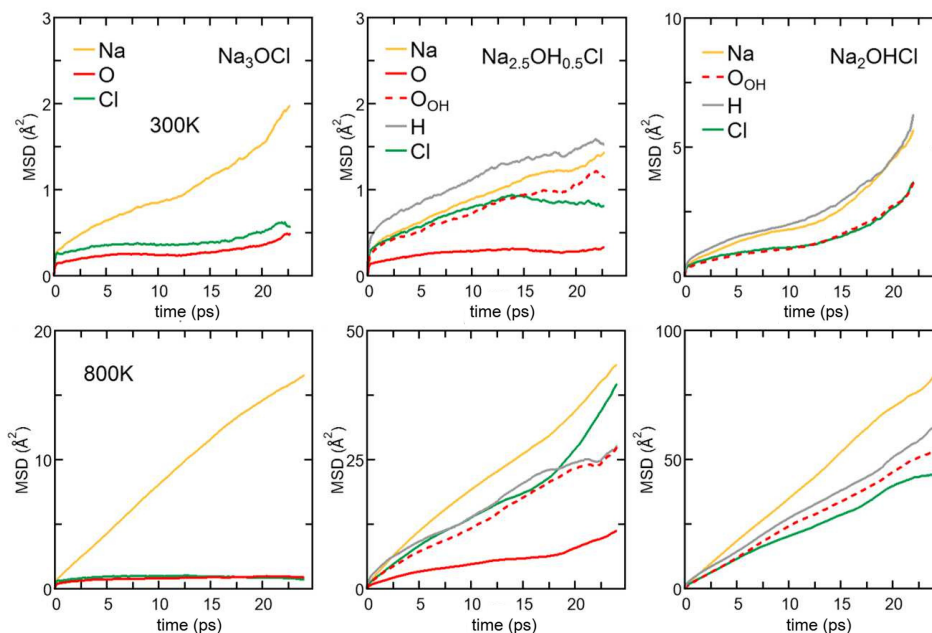


Figure 4.6: MSD versus time for each element in amorphous $\text{Na}_{3-x}\text{OH}_x\text{Cl}$ ($x=0$, $x=0.5$, $x=1$) at $T = 300$ K (top) and $T = 800$ K (bottom). Colors legend: Na, yellow; O non-bonded to H atoms, red (solid line); O bonded to H atoms, red (dashed line); H, grey; Cl, green. Note that the MSD calculated at the temperatures $T=300$ K, $T=450$ K, $T=600$ K, $T=800$ K, $T=1000$ K are reported in the ESI, (Fig. S1).

of O atoms are coordinated only by Na atoms with the remaining having, in addition to Na, one H atom as neighbor within hydroxyl OH groups. These percentages change in Na_2OHCl to accommodate more H atoms. Regarding Cl atoms the behavior is similar to the one of O atoms after partial replacement of Na by H atoms. In particular, n_{Cl}^p decreases from ~ 5.7 in Na_3OHCl to ~ 5.4 and ~ 4.8 , for $\text{Na}_{2.5}\text{OH}_{0.5}\text{Cl}$ and Na_2OHCl , respectively. The amorphous nature of the network favors relatively short Na-Cl distances (~ 2.75 Å) when compared to those found in the crystalline phase, where each Cl atom is surrounded by twelve Na atoms at a distance of ~ 3.18 Å.

4.3.2 Dynamical properties

Mean square displacements

A first insight into the dynamical properties of amorphous $\text{Na}_{3-x}\text{OH}_x\text{Cl}$ is provided by the mean square displacement (defined in Sec. 4.2.2 and labeled MSD) of the different ions shown in Fig. 7 at $T = 300$ K and 800 K. Additional details can be found in Fig. S2 of the ESI. At $T = 300$ K, Na ions in Na_3OCl are mobile, while the MSD of both Cl and O remains very

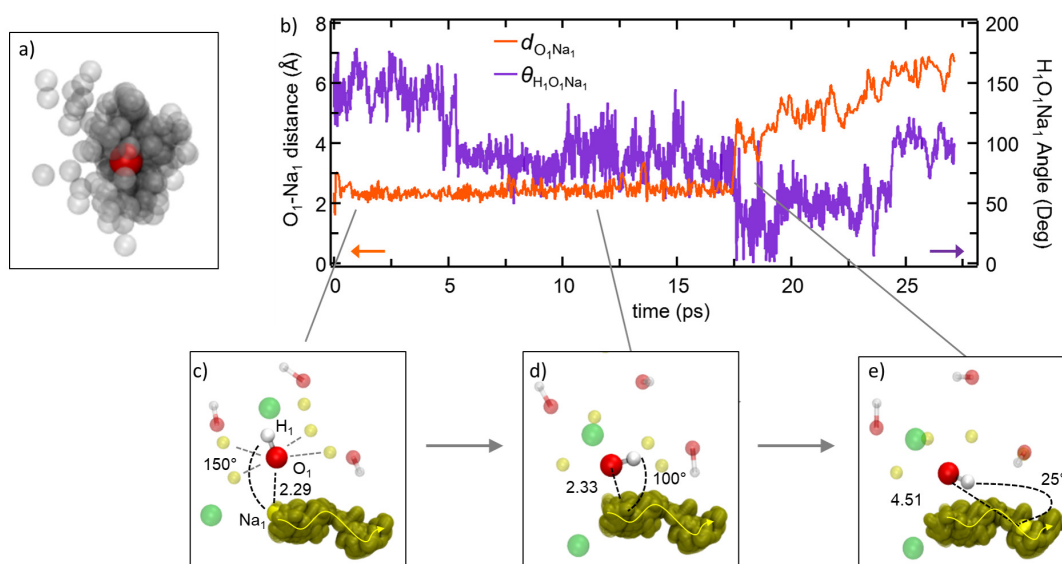


Figure 4.7: a) Rotational dynamical disorder of a given H atom (grey transparent sphere) around one O atom (red opaque sphere) of one hydroxyl OH group in amorphous $\text{Na}_{2.5}\text{OH}_{0.5}\text{Cl}$ over a time span of ~ 30 ps. b) Temporal evolutions of: (a) the interatomic distance between the O_1 atom of one hydroxyl group and a coordinated Na_1 atom, (b) the $\text{H}_1\text{O}_1\text{Na}_1$ angle. c-e) Proposed paddlewheel dynamics found in amorphous $\text{Na}_{2.5}\text{OH}_{0.5}\text{Cl}$ and Na_2OHCl . c) Between 0 and 5.2 ps, a sixfold coordinated O_1 atom of one hydroxyl group shows a bonding distance of 2.29 Å with the Na atom labelled Na_1 . In between 5.2 ps and 17.5 ps, the hydroxyl OH bond is rotating with respect to Na_1 (from $\sim 150^\circ$ to $\sim 100^\circ$) while maintaining a distance $\text{O}_1\text{-Na}_1$ equal to 2.33 Å. e) After 17.5 ps a further rotation of the OH group bringing the corresponding angle from $\sim 100^\circ$ to $\sim 25^\circ$ induces the displacement of Na_1 atom to a larger distance (>4.5 Å) escaping the first coordination shell of O_1 atom. The surrounding atoms of O_1 at a distance lower than >5 Å are shown in transparent color. Dashed lines indicate the atoms coordinated within the first coordination shell of O_1 (<3.3 Å). The concerted migration pathway of Na_1 atom along the ~ 30 ps is shown in transparent dark yellow. As a guide, an arrow is added to indicate the direction of the pathway. Color legend: Na atoms, yellow; O atoms, red; Cl atoms, green; and H atoms, white.

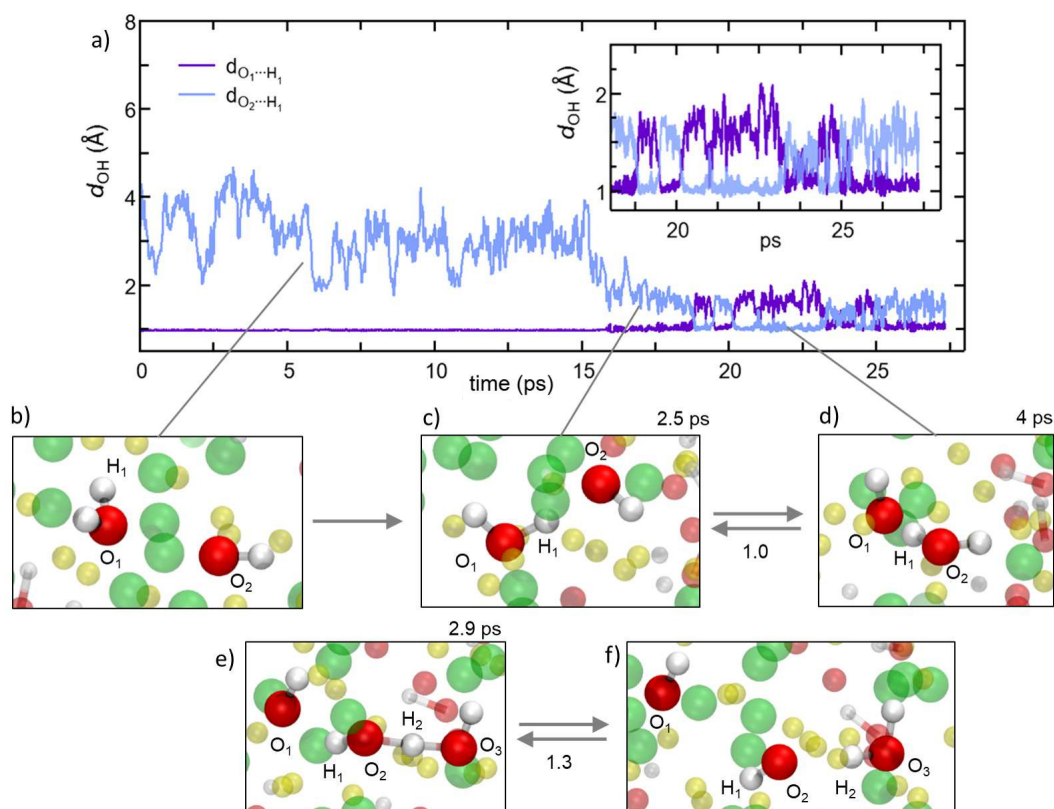


Figure 4.8: For the Na_2OHCl system: proton hopping process by which H atoms migrate through a dynamical switch between σ - and hydrogen-bonds giving rise to the formation of metastable water molecules (i.e. Grotthuss-like mechanism).[226–231] a) Temporal evolution of the interatomic distance between one H atom labelled H_1 atom, belonging to a water molecule initially formed, and its bonded O atom labelled O_1 . Also shown is the temporal evolution of the distance between H_1 and a second O atom labelled O_2 that is part of a neighboring hydroxyl group. Inset: zoom-in on the temporal window along which H_1 is shared between two O_1 and O_2 , leading to the transient formation and breaking of OH bond and water molecules. b-f) Inter-unit transitions between structural units in amorphous Na_2OHCl at 300 K. Indicatively, the mean lifetimes of the transient H-bonds and water molecules are reported on top of the panels whereas the transition rates are reported between the panels. Here, the transition rate is defined as the number of inter-unit transitions per ps observed within a given process (H-bond or water molecules formation). Color legend: Na, yellow; O, red, and Cl green.

low. This trend holds at higher temperatures (Fig. 7 and Fig. S1 of the ESI), with Na ions reaching over the span of ~ 25 ps MSD values $\sim 2.0 \text{ \AA}^2$ at $T = 300 \text{ K}$ and 450 K , $\sim 6.0 \text{ \AA}^2$ at $T = 600 \text{ K}$, $\sim 18 \text{ \AA}^2$ at $T = 800 \text{ K}$, $\sim 61 \text{ \AA}^2$ at $T = 1000 \text{ K}$ and $\sim 115 \text{ \AA}^2$ at $T = 1200 \text{ K}$. These results indicate that amorphous Na_3OCl behaves differently from its corresponding defect-free crystalline phase, where Na/Li diffusion is absent due to the lack of disorder induced by the presence of vacancies, as found in crystalline antiperovskites via Schottky defect pairs.[232, 233] Regarding Cl and O ions, the mobility for both ions at $T = 300$ and 800 K is lower than $\sim 1 \text{ \AA}^2$, and increases significantly only at higher temperature indicating a motion beyond a mere local rearrangement. Heenen and coworkers [182] obtained analogous results for both Cl and O ions; yet, the Cl higher mobility was interpreted as not-negligible and, later also termed 'sluggish'. [234]

Different behaviors are recorded in the case of the hydroxylated systems. By keeping in mind that about $\sim 50\%$ of oxygen atoms are present as OH^- hydroxyl groups in $\text{Na}_{2.5}\text{OH}_{0.5}\text{Cl}$, we reported the MSD data of individual oxygen atoms and those bonded to H atoms (as OH^- anions) separately. At $T = 300 \text{ K}$, we found that Na and individual O ions in $\text{Na}_{2.5}\text{OH}_{0.5}\text{Cl}$ have MSD values similar to those found in Na_3OCl . The MSD of Cl reaches $\sim 0.9 \text{ \AA}^2$ over ~ 14 ps followed by stabilization, whereas there is a steady time increase of MSD for O atoms involved in OH groups as well as H atoms, following the same rate of increase of Na ions. The enhanced mobility of H atoms can be ascribed to the high rotational dynamical disorder of H atoms around an O atom of a hydroxyl group (see Fig. 8a) and to the high mobility of O atoms involved in OH groups. This trend is clearly supported by the MSD of $\text{Na}_{2.5}\text{OH}_{0.5}\text{Cl}$ as a function of temperature. Focusing on Na ions at $T = 800 \text{ K}$, their MSD after ~ 25 ps is ~ 2.5 times larger than the one found in Na_3OCl . Therefore, it appears that the presence of H atoms promotes an increase in Na ions mobility at temperatures higher than $T = 300 \text{ K}$. This occurs also for Cl ions and both O and H involved in OH groups. In contrast, individual O ions (i.e. non bonded to H) are found somewhat less mobile (Fig. 7, lower part, $T = 800 \text{ K}$).

To complete our case study and extract a global picture from the behaviour of the mean square displacement, we focus on Na_2OHCl . A first observation from Fig. 7 (rightmost part) reveals that similar trends for the MSD are found. However, OH^- anions boost the MSD of the other species significantly already at room temperature. This effect can be fully appreciated by noting that in Na_2OHCl $\sim 92\%$ of O atoms binds at least one H atom either as OH^- anions or in water molecules. At $T = 300 \text{ K}$ and after ~ 25 ps, Na ions in Na_2OHCl reached a value of MSD ~ 3 times larger than the one found in Na_3OCl , H, Cl, and O atoms are equally highly mobile concurring to confirm that the MSDs, although lower than for Na ions, are by all means larger than the one obtained in Na_3OCl . At $T = 800 \text{ K}$, the mobility of Na ions is further boosted by the presence of H atoms, approaching 100 \AA^2 after ~ 25 ps. This value is remarkably larger

than the one reported by Dawson et al. [171] for crystalline Li_2OHCl ($\sim 6 \text{ \AA}^2$ after $\sim 50 \text{ ps}$ at $T = 800 \text{ K}$). What we found for Na_2OHCl differs drastically from what has been reported in crystalline Li_2OHCl antiperovskites, where only rotational dynamics were highlighted for the hydroxyl OH^- groups and no long-range mobility.[171] In this crystalline phase, H atoms are characterized by a constant MSD of $\sim 2 \text{ \AA}^2$ at $T = 600 \text{ K}$ on a time scale of $\sim 50 \text{ ps}$, whereas the present Na_2OHCl model features an increase of the MSD to a value of $\sim 28 \text{ \AA}^2$ after $\sim 25 \text{ ps}$ at $T = 600 \text{ K}$ (Fig. S1 in ESI).

The paddlewheel effect

We have found that the mobility of Na ions in $\text{Na}_{3-x}\text{OH}_x\text{Cl}$ is strictly related to the presence of hydroxyl OH^- anions. An important relationship between the Na-ion transport mechanism and O–H rotation effects in these systems has been reported by Song et al.[235] and Howard et al.[236] These studies demonstrate that the rapid rotation of O–H bonds leads to the creation of empty space promoting the formation of defects, which, in turn, are crucial for achieving fast, correlated Na-ion transport. The rotational disorder due to the hydroxyl OH^- anions, along with other anions such as BH_4^- and NH_2^- , is a feature common to other solid electrolytes, such as crystalline Na_3OCl [172] and $\text{Na}_{3-x}\text{O}_{1-x}(\text{NH}_2)_x(\text{BH}_4)$.[237] Ions migration occurs via a mechanism that combines the concerted motion of ions with large quasi-permanent reorientations of the surrounding hydroxyl groups. This latter effect, known as the *paddlewheel* mechanism,[185, 238, 239] is typically observed in high-temperature crystalline polymorphs.[240]

Unlike in crystalline materials, the paddlewheel dynamics in glassy matrices can contribute to the ion mobility also at room temperature,[185] via the strong coupling between the rotational motion of the anions and the translational motion of the alkaline cations.[185, 238, 240] Based on the above analyses, we propose that H-containing amorphous $\text{Na}_{3-x}\text{OH}_x\text{Cl}$ show three distinct features that facilitate the occurrence of paddlewheel dynamics. The degree to which these dynamics manifest themselves is temperature-dependent. First, these systems contain hydroxyl groups which are free to rotate, impacting the neighbouring cations. Second, the amorphous matrix has a lower density than its crystalline counterpart that makes available additional free volume for O–H rotations, facilitating anion reorientations. Third, while it is typical for most glasses to exhibit a lower density compared to their crystalline form, amorphous $\text{Na}_{3-x}\text{OH}_x\text{Cl}$ systems have a potentially unusual characteristic - the absence of covalent bonding in their atomic structure. These features are found in strong accordance with the features of paddlewheel dynamics reported for glass.[185]

A more detailed view of the dynamical mechanism is shown in Figure 8b-e. These panels illustrate the rotation of one hydroxyl (OH) group nearest neighbor to one sodium (Na)

ion during Na migration. Throughout the entire process, O(OH) and Na maintain their coordination of six cations and four-to-five anions, respectively. The coordination of Na is preserved by means of rotational displacements of the anion through a paddlewheel-type mechanism. Another salient feature observed in these migration events is the dissociation or *undocking* of Na from a subset of its neighboring anions at the onset of the process, followed by its association or *docking* to new anions towards the end.[185]

Former experimental and computational results have also stirred a debate about the formation of water molecules in antiperovskites. Based on analysis presented above, $\text{Na}_{2.5}\text{OH}_{0.5}\text{Cl}$ appears not to show any water formation since all H atoms are bound in OH groups, while our Na_2OHCl model system does, with $\sim 9.3\%$ of O atoms involved in H_2O molecules. The formation of these water molecules can be elucidated by following, as done in Fig. 9a, a typical H hopping process involving OH groups in Na_2OHCl at $T = 300\text{ K}$. We first show the temporal evolution of two representative distances. The first is the one between the H atom termed H_1 belonging to a water molecule, previously formed, and the O atom termed O_1 atom to which it is bonded ($d_{\text{O}_1\text{H}_1}$, initially at $\sim 0.98\text{ \AA}$). The second one concerns the same H_1 atom and a second O atom termed O_2 atom belonging to a neighbouring OH group ($d_{\text{O}_2\text{H}_1}$, initially at $\sim 3.8\text{ \AA}$; Figure 9b). After about $\sim 15\text{ ps}$, H_1 starts forming a strong hydrogen bond (H-bond) with the neighbouring O_2 atom of one OH hydroxyl group at a distance of $\sim 1.9\text{ \AA}$. The mean lifetime of this transient H-bond is $\sim 2.5\text{ ps}$. Then, H_1 is shared between O_1 and O_2 via forming and breaking O-H bonds showing an average $d_{\text{O}_{1,2}\text{H}_1}$ distance of $\sim 1.6\text{ \AA}$ and forming eventually a water molecule upon H transfer (Fig. 9c-d). Its transition rate, defined as the number of inter-unit transitions per ps observed within a given process (H-bond or water molecules formation), is of about 1.0 before the formation of a stable new H_2O molecule. In Fig. 9 panels e-f exemplify the dynamical evolution of the previous environment toward H transfer to a third hydroxyl group (from O_2 to O_3), resulting in the formation of a new water molecule. The presented mechanism is very similar to the known Grotthuss one [226–231] in which the H atom switches between a σ -bond and a hydrogen bond to propagate and eventually stabilize in a newly formed water molecule, as in proton-conducting solid-oxide materials.

Ions diffusion

The long-range mobility of alkaline ions in a solid-state electrolyte can be assessed by considering the log-log plot of the MSD (Eq. (4.2) vs t for the temperatures of interest (see Fig. 4.10). Several regimes are noticeable as a function of time, especially at not too high temperatures ($T = 300\text{ K}$ and $T = 450\text{ K}$ in our case). The initial part consists of a ballistic regime with the MSD taking a quadratic dependence with time. With increasing t , a plateau is

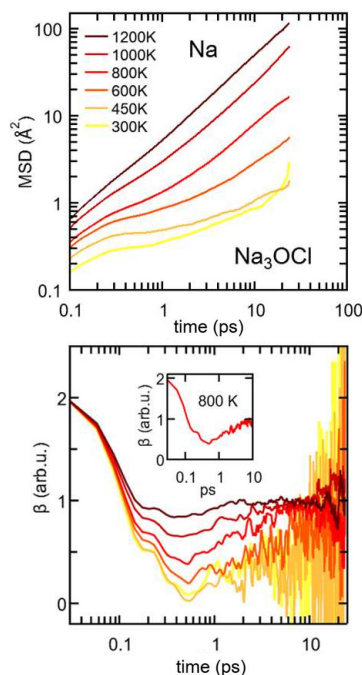


Figure 4.9: Top: Log-log plot of MSD vs time for Na in Na_3OCl at temperatures in between $T = 300\text{ K}$ and 1200 K . Bottom: corresponding values of β . Inset: β value as a function of time at $T = 800\text{ K}$.

attained corresponding to the so-called caging regime with Na ions trapped in a very limited portion of space by the nearest neighbors. In Na_3OCl , the cage regime clearly persists up to a few ps at $T = 300\text{ K}$ and $T = 450\text{ K}$, while at $T = 600\text{ K}$ it lasts no longer than $\sim 1\text{ ps}$ and does not manifest itself at higher temperatures. Then, the diffusive regime for Na atoms sets in at longer times with Na ions moving along preferential paths. Under these conditions, the MSD takes a linear dependence on time and the ion self-diffusion coefficients (D^*) can be obtained via the Einstein equation (Eq. (3)) at the different temperatures.

The onset of the diffusive regime can be monitored via the time behaviour of β (Eq. (2)), given in Fig. 11 for Na_3OCl . As expected, the higher the temperature the faster β approaches ~ 1 , i.e. at $T = 800\text{ K}$, 1000 K , and 1200 K this target value is reached after $\sim 6\text{ ps}$, $\sim 4.6\text{ ps}$, and $\sim 1.5\text{ ps}$, respectively. At lower temperatures, the diffusive regime is not reached within $\sim 25\text{ ps}$, the behaviour of β being affected by statistical noise for increasing time. Analogous information on the MSD of the two hydroxylated systems is given in Fig. S1, ESI (linear plot) and Fig. S2, ESI (log-log plot, as in Fig. 10). Remarkably, for T lower than 450 K , the cage regime is shorter ($\sim 1\text{ ps}$) for $\text{Na}_{2.5}\text{OH}_{0.5}\text{Cl}$ and it disappears for Na_2OHCl . This is consistent with the boosted Na ions dynamics due to OH anions rotational mechanism discussed before. Also, the MSD trend of H atoms features high values at short times ($< \sim 1\text{ ps}$) for any given

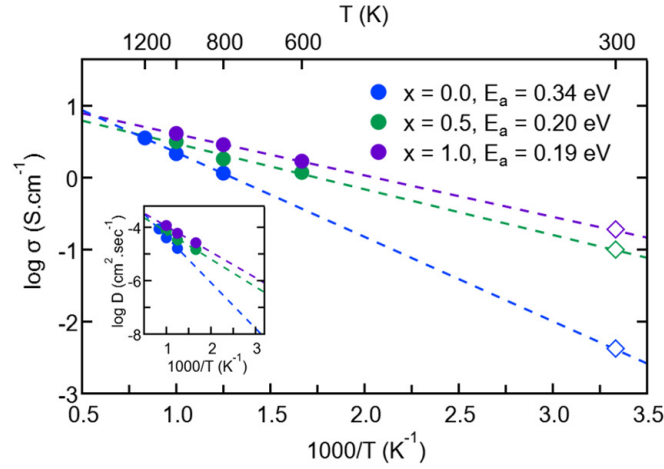


Figure 4.10: Na-ion self-diffusion coefficients (inset) and conductivities of amorphous $\text{Na}_{3-x}\text{OH}_x\text{Cl}$ ($x=0$, $x=0.5$, $x=1$). We also report the activation energies of Na ionic conduction obtained via a linear Arrhenius fit. Closed circles correspond to FPMD data and open circles correspond to data at $T = 300$ K extrapolated by using the linear Arrhenius fit.

temperature, again due to the rotational disorder of OH anions. At longer times MSD profiles of H and Na atoms do superpose as a result of a fully enhanced diffusive behavior concerning all Na and OH groups.

Having identified the temperatures at which Na ions reached the diffusive regime, we calculated for the three systems the self-diffusion coefficients (tracer, D^*) for Na by using the Einstein equation (Eq. (3)) and then converted it into Na-ion conductivities with Eq. (5). By plotting these data according to the relationship $\log D^*$ vs $1000/T$ (Fig. 11) and fitting it in the Arrhenius form, we obtain by extrapolation the uncorrelated tracer conductivity σ^* of Na ions at $T = 300$ K, as customarily done for crystalline solid-state electrolytes.[166, 171] D^* and σ^* values are reported in Table 3, together with the calculated activation energy (E_a) of Na ions transport. In the case of amorphous Na_3OCl E_a is equal to 0.34 eV, a value close to the one calculated for defected crystalline Na_3OCl .[160, 176]

Ionic conductivity and correlation effects

In terms of conductivity σ^* , we obtained a value ~ 0.8 mS.cm^{-1} for Na_3OCl close to ~ 0.2 mS.cm^{-1} obtained by Dawson et al. at 500 K.[166] We obtained $E_a = 0.20$ eV, $E_a = 0.19$ eV and a tracer conductivity equal to ~ 44 mS.cm^{-1} and ~ 83 mS.cm^{-1} for $\text{Na}_{2.5}\text{OH}_{0.5}\text{Cl}$ and Na_2OHCl , respectively. These data demonstrate that Na ions transport is promoted by the addition of H atoms. These values correspond to the ideal case where no collective effects are taken into account, as those due to alike-Na ions or different ions. However, since these effects

Table 4.3: Na tracer diffusion coefficients (D^*), Na ions tracer (σ^*), charge (σ^σ) and total conductivities (σ^{tot}), activation energies (E_a) and Haven ratio ($H_R^{J,tot}$) extrapolated at $T = 300$ K and directly computed at $T = 800$ K on the basis of FPMD simulations. We report the values for the three $\text{Na}_{3-x}\text{OH}_x\text{Cl}$ ($x = 0, x=0.5, x=1$) models.

	T (K)	x = 0	x = 0.5	x = 1.0
D^* ($\text{cm}^2 \cdot \text{s}^{-1}$)	300K ^a	$4.29 \cdot 10^{-9}$	$2.63 \cdot 10^{-7}$	$6.23 \cdot 10^{-7}$
σ^* ($\text{S} \cdot \text{cm}^{-1}$)	300K ^a	0.0008	0.044	0.083
E_a (eV)	300K	0.34	0.20	0.19
D^* ($\text{cm}^2 \cdot \text{s}^{-1}$)	800K	$1.64 \cdot 10^{-5}$	$3.25 \cdot 10^{-5}$	$6.00 \cdot 10^{-5}$
σ^* ($\text{S} \cdot \text{cm}^{-1}$)	800K	1.14	1.84	2.84
σ_{ion} ($\text{S} \cdot \text{cm}^{-1}$)	800K	0.27	0.66	1.33
σ_{ion}^{tot} ($\text{S} \cdot \text{cm}^{-1}$)	800K	1.17	1.97	3.96
H_R^σ	800K	4.18	2.79	2.14
H_R^{tot}	800K	1.33	2.02	2.03

^a Data extrapolated at $T = 300$ K.

are present in experiments, it is appropriate to account for them by considering the so-called Haven ratio (H_R) which can be obtained via Eqs. (7-8) in order to quantify the contribution of alike-Na ions (H_R^σ)[212–214, 217] or a total contribution coming from all positive and negative ions (H_R^{tot} , Eq. 9).[207]

Often, previous studies on crystalline Li/Na antiperovskites assumed a Haven ratio equal to 1 disregarding collective effects.[166, 171] While single-ion conducting glasses typically exhibit Haven ratios of ~ 0.1 - 0.6 indicative of positive correlating effects,[206, 241] ionic liquids[207] and molten salts[208] behave oppositely with H_R values larger than 1. For comparison, in Tab. 3 we report the values of H_R^σ , H_R^{tot} and the corresponding Na and total conductivities obtained at $T = 800$ K. We obtained H_R^σ values larger than 1, indicating a strong negative effect of the collective correlations of alike-Na ions. Therefore, at this temperature, the behaviour of amorphous $\text{Na}_{3-x}\text{OH}_x\text{Cl}$ systems in terms of conductivity is closer to ionic liquids and molten salts than to a glassy matrix. We also remark that this specific effect is less important when Na is partially replaced by H (from 4.2 for Na_3OCl to 2.8 and 2.1 for the two hydroxylated phases). Finally, the resulting Na charge conductivities (σ_{ion}) are lower than the uncorrelated Na tracer conductivity σ^* for the three systems.

In terms of H_R^{tot} , we obtained for Na_3OCl a much lower value than H_R^σ (1.33 vs 4.18) which indicates close contributions of positive and negative collective correlated effects when the mobility of all ions is taken into consideration. This is not the case for the two hydroxylated models, as shown by close values of H_R^{tot} and H_R^σ meaning that in the presence of H (OH hydroxyl groups) negative effects are more important. The corresponding final total ionic conductivities (σ_{ion}^{tot}) are very close to the Na ions uncorrelated σ^* estimation for Na_3OCl

(1.17 vs 1.14 S.cm⁻¹), moderately larger for Na_{2.5}OH_{0.5}Cl (1.97 vs 1.84 S.cm⁻¹) and sizeably higher for Na₂OHCl (3.96 vs 2.84 S.cm⁻¹). Therefore, Na ionic conductivity of disordered Na_{3-x}OH_xCl systems can be a viable, effective alternative to the crystalline counterparts, the partial replacement of Na with H enhancing ion transport. However, the mobility of the other ions (Cl, O, and H) is concomitantly boosted which might be detrimental to practical electrolyte applications.

4.4 Summary

X₃OA-based antiperovskites have shown promising potential as solid-state electrolytes for ion batteries due to their structural and dynamical properties. However, while the structure and ion dynamics mechanisms of crystalline X₃OA compounds are well-known, there is a lack of quantitative structural characterizations for amorphous antiperovskites. In this study, we used first-principles molecular dynamics to quantitatively assess the structure and ion dynamics mechanisms of three amorphous Na_{3-x}OH_xCl (with x=0, 0.5, 1) Na-rich antiperovskites. We found that amorphous Na₃OCl shows a substantially different structure compared to its crystalline counterpart, with a disordered structure exhibiting limited intermediate range order and short-range order driven by a majority of four-fold Na atoms (~70%), in terms of counter-ions coordination by means of ionic bonds. Na-O bond distances are close to those reported in the crystalline phase, while Na-Cl distances are significantly shorter. As a result, a reduced number of neighboring counter-ions and Na atoms are favored in the local surrounding of Na atoms in the amorphous phase. Na is found primarily coordinated to both anions (O and Cl), with only a small percentage of Na atoms coordinated exclusively to O or Cl atoms. These results unveil contrasting differences in the structure of amorphous Na₃OCl compared to previous models conjectured for glassy Li₃OCl, which was based on the segregation of Li₂O and LiCl-rich regions.

The partial replacement of Na atoms with H in the two hydroxylated phases studied (Na_{2.5}OH_{0.5}Cl and Na₂OHCl) gives rise to a lower degree of structural organization when compared to H-free Na₃OCl, with all H atoms bonded to O atoms. Amorphous Na₃OCl has a unique microscopic structure that enables remarkable Na ion dynamics and ionic conductivity, challenging that of defective crystalline phases. The presence of hydroxyl OH⁻ anions in the hydroxylated models is crucial for the mobility of Na ions, which is enhanced by rapid rotation of O-H bonds and paddlewheel-type mechanisms. This promotes the formation of available space, which is essential for achieving fast Na-ion transport. Interestingly, the paddlewheel dynamics in the hydroxylated models glassy matrices can contribute to ion mobility even at room temperature, owing to the strong coupling between the rotational motion of the anions

and the translational motion of the alkaline cations. In terms of correlated dynamical effects, the behaviour of amorphous $\text{Na}_{3-x}\text{OH}_x\text{Cl}$ is found closer to ionic liquids and molten salts than to a glassy matrix. We also remark a net balance of positive and negative correlated effects for Na_3OCl , whereas for the two hydroxilated phases negative effects are more important.

Concerning the presence of water molecules in antiperovskites, our study proves that the presence of H atoms promotes the formation of H-bonds in $\text{Na}_{2.5}\text{OH}_{0.5}\text{Cl}$ while only in the case of Na_2OHCl formation of a small amount of water is observed.

Overall, the results obtained in this work adds to the growing evidence that disordered Na-rich antiperovskites provide a viable and effective alternative to their crystalline counterparts as solid state electrolytes. Our results underscore the significance of conducting quantitative structural assessments to better comprehend the impact of structure on the performances of these systems.

Chapter 5

First quantitative assessment of the structure of amorphous antiperovskite Na_3OCl by first-principles and machine learning molecular dynamics

5.1 Introduction

Solid-state electrolytes have attracted much attention in the field of electrochemical energy storage due to their potential to overcome safety and performance limitations associated with traditional liquid electrolytes. Among them, amorphous antiperovskite electrolytes have emerged as a promising class of materials due to their high ionic conductivity and excellent stability. However, the complex nature of these disordered materials has made their understanding and characterization challenging. In recent years, ab initio molecular dynamics and machine learning molecular dynamics have become powerful tools for simulating the structural and transport properties of materials, including amorphous electrolytes. A recent review, on the use and exploitation of anti-perovskites for solid-state batteries, underlined the limited nature of the structural characterization reported so far in literature and also pointed out the severe need of quantitative structural assessment for X_3OA systems to avoid any misinterpretation of their structure/performance correlations.[160] M-ion-based oxyhalide materials (M= Li-, Na-, and K-) have been synthesized in the form of mixed amorphous/crystalline phases and characterized by a set of experimental techniques (neutron and X-ray diffractometry, Raman spectroscopy, thermal analysis, and transmission electron microscopy) combined with reverse Monte Carlo (rMC) simulations. The ionic conductivity

was determined to be in the range of $1.1\text{-}6.1\cdot 10^{-6}$ S·cm⁻¹ for all Li-, Na-, and K-based samples at room temperature.[242]

A detailed understanding of the atomic structure is a key step to further capture the details of the transport mechanisms behind its conductivity performance. Recent reviews on the use of anti-perovskites for solid-state batteries underlined the limited nature of the available structural characterization and pointed out the severe need of a quantitative structural assessment to avoid any misinterpretation of the correlations between structure and performances.[160, 186] The structure and ion dynamics mechanisms for amorphous antiperovskites are still under debate. The capability to deal with length and time scales for a complex systems which are beyond the reach of any ab initio technique. For this reason, empirical interatomic potentials have been studied, fitted typically to an ab initio data, that are capable of simulating systems containing thousands or millions of atoms for thousands or millions of time steps.

In this work, we follow an alternative approach, generating a Gaussian approximation potential (GAP)[86] for the amorphous antiperovskite Na₃OCl. GAP is a highly flexible machine-learning model that allows to fit directly and accurately first-principles potential energy surfaces (PES). Transferability is ensured by regular and smooth basis functions (kernels, in the language of machine learning), and by an extended training database which covers here roughly 600 000 local atomic environments (LAEs). Similar machine-learning approaches, such as neural networks, have been successful recently in modeling materials where previous, more empirical strategies have run out of steam.[85, 243, 244] GAP uses Gaussian process regression, whose advantages are that (i) its hyperparameters (that control the kernel function and linear algebra regularization) make physical sense and rarely need adjusting, (ii) the fit itself is determined by simple linear algebra, rather than iterative nonlinear optimization of a highly multimodal function as in the case of neural networks, and (iii) input data such as energies, forces, and stresses are treated in a consistent manner, with appropriate error estimates that allow the inclusion of variable accuracy data. In the machine-learning literature, Gaussian process regression is often thought of as scaling poorly (cubically) with the size of the input data, the well-known heuristics allow us to limit the number of basis functions to be much smaller than the number of input configurations, and to prediction costs similar to that of neural networkbased potentials.[245] The key to the success of Gaussian process regression is an appropriate kernel function that captures the symmetries and describes the spatial correlation structure of the target function. We use the “smooth overlap of atomic positions” (SOAP) kernel[246] that has been shown previously to lead to excellent results for other materials[247–250]

5.2 Computational methodology and models

5.2.1 First-principles molecular dynamic simulations

We make use of FPMD in the Car-Parrinello scheme (CPMD) [187]. The XC exchange-correlation functional adopted is the Perdew-Burke-Ernzerhof (PBE) together with the generalized gradient approximation (GGA). [188] The valence-core interaction was modeled by norm-conserving Troullier-Martins (TM) [189] pseudopotentials for O and Cl whereas in the case of Na, the use of semi-core states was found to be essential for a good description of both the structure and the energetics. The electrons of Na 2s, 2p, 3s; O: 2s, 2p; Cl 3s, 3p were treated explicitly as valence electrons and expanded in a plane-wave basis set with an energy cutoff of 80 Ry, with the sampling of the Brillouin restricted to the Γ point. A fictitious electron mass of 600 a.u. and a time step of 0.12 fs guaranteed optimal conservation of the constant of motion.

FPMD simulations were performed in the canonical ensemble with the ionic temperature controlled with a Nosé-Hoover [190–192] thermostat chain [193] and for the simulations performed at high temperature (>1000 K) to control the fictitious electronic kinetic energy we used a Blochl-Parrinello thermostat [194] with a target kinetic energy of 0.1 a.u. The Na_3OCl glass model was generated by quenching from the melt. The initial configuration consisted of the Na_3OCl crystal unit cell replicated $3 \times 3 \times 3$ times to obtain a 135 atoms (81 Na, 27 O and 27 Cl) in a cubic simulation cell of side 13.6148 Å. The initial box was expanded of 15% with respect to crystal density in order to facilitate the melting at high temperature corresponding to an atomic number density of 0.05349 \AA^{-3} . A similar approach was used also for the case of glassy Li_3OCl . [182] Periodic boundary conditions were applied throughout the FPMD simulations.

The model underwent a thermal cycle via canonical NVT simulations, according to the following protocol: 1.3 ps at $T=300$ K, 1.2 ps at $T=1200$ K, 70 ps at $T=1500$ K, 46.5 ps at $T=1800$ K, 38.6 ps at $T=1000$ K, 33.7 ps at $T=750$ K and 35 ps at $T=300$ K. We remark that at 1800 K the system melts and it is characterized by pair correlation functions reminiscent of the liquid state. At 300 K the density of the system was set to 2.0378 g/cm^3 in order to have a final model at close to 0 GPa pressure. Along the thermal cycle 80 Ryd was used as plane wave cut-off, whereas at 300 K 160 Ryd with a time step of 0.07 fs was used in order to converge the assessment of the system pressure within 20 ps. In what follows, the results are presented as time-average values over the last part (15 ps) of the thermal cycles at $T=300$ K.

5.2.2 DFT-FPMD database composition

We build a database made of reference configurations on the desired regions of phase space and associated quantum mechanical data (energies, forces and virials) by extracting a certain numbers of representative configurations from the FPMD trajectories obtained at different temperatures. In a first attempt, we build a database made only of 100 configurations extracted from the trajectories simulated at high and room temperature (1200 and 300 K) in GAPA. In a second attempt, we extracted a total of 200 configurations from the trajectories produced at 1200, 800, 450 and 300 K. This amounts to a total of 27000 energy values, 81000 force components and 1200 virial components. In order to achieve a good accuracy of the database, we recomputed DFT energies, forces, and virials for all the configurations at an energy cutoff of 160 Ry

5.2.3 MLP-GAP molecular dynamics simulations

Finally, we exploit the fitted GAP potential to produce new models of Na₃OCl glass by following a thermal cycle via canonical NVT simulations, according to the following protocol: from 1200K to 300K with a cooling rate of 4 K/ps. The equations of motion were integrated by using a timestep of 1 fs and NH thermostat was used as implemented in the LAMMPS code.^[251] With such procedure we produced MLP-GAP models with the same density (2.04 g/cm³) for following sizes: 135 atoms model (hereafter denoted as GAP1 model), 405 (GAP1.4), 810 (GAP1.8), 1080 (GAP2) and 3645 (GAP3) atoms model (hereafter denoted as GAP1, GAP1.4, GAP1.8, GAP2 and GAP3, respectively. GAP1 was averaged over 11 replica run, whereas GAP2, and GAP3 were averaged over 2 runs; the other MLP-GAP models were averaged over 3 runs. The obtained glassy model is used to consolidate the FPMD structural model of Na₃OCl by relaying on a large size system obtained at the DFT accuracy. When useful, the results of the GAP models are presented and discussed throughout the paper.

5.3 Results and discussion

5.3.1 Machine learning interatomic potential: model fitting and training database

We resort to a kernel-based ML method that adopts a Gaussian approximation potential (GAP) approach allowing to learn and reproduce smooth highly dimensional potential energy surfaces by interpolating DFT data.^[252–254] This ML approach has been successfully applied to

many liquids and crystalline phases,[81, 245, 250, 255] several mono[247–250] and binary glasses[81, 256] systems but only a few ternary amorphous systems so far.

Values for the GAP hyperparameters as used in this work are given in Table 1. Furthermore, the regularization parameters of the Gaussian process corresponding to the expected errors were as follows. For liquid and amorphous structures we set 0.008 eV (energies), 0.05 eV/Å (forces) and 0.05 eV (virials). Sparsification was done with the CUR method[257] for the SOAP kernel, whereas a simple uniform grid of basis function locations was used for the 2b terms.

5.3.2 MLP-GAP model performance assessment: errors for testing versus training set

We here assess the validation of the accuracy of our GAP model based on the DFT-FPMD reference data. The training and testing datasets contain 81000 atomistic reference force components each. As shown in Fig. 1, the total energies, atomic forces and virial as predicted by our model are compared with those from DFT. It is observed that the energies are well reproduced by our GAP with a low mean-averaged-error (MAE) of 0.93 meV/atom for the testing datasets. Forces in the testing datasets are predicted with a MAE of 0.04 eV/Å whereas virials are predicted with a MAE of 2.44 meV/atom. The results demonstrate that our GAP model is a good representative of the first-principles PES. It is noted that the test error is much higher than the training error for those configurations with higher energy. Figure 5.1 shows the errors as cumulative distributions: the curves move left (toward lower errors) and up (to a higher degree of confidence) comparing the training and testing predicted quantities.

Hyperparameters	GAPA	GAPB	GAPC	GAPD	GAPE	GAPF	GAPM	GAPN	GAPQ
2b Descriptor									
Cutoff	4.0	4.0	5.0	5.0	5.0	5.5	5.0	5.0	5.0
δ	0.1	0.1	0.1	0.1	0.1	0.1	0.1	0.1	0.1
θ	1.0								
Spare method	uniform								
Covariance	Gaussian								
Sparse points	50								
SOAP Descriptor									
Cutoff	4.0	4.0	5.0	5.0	5.5	5.5	6.0	5.5	5.5
Cutoff width	1.0								
δ	1.0								
σ_{all}	0.7								
sparse method	CUR								
sparse points	600	600	800	800	600	600	600	800	800
lmax	8.0	8.0	8.0	8.0	8.0	8.0	8.0	8.0	8.0
nmax	8.0	8.0	8.0	8.0	12.0	12.0	10.0	10.0	10.0
ζ	4.0								
Regularisation									
σ_e (eV)	0.001	0.001	0.001	0.005	0.005	0.005	0.008	0.005	0.008
σ_f	0.05								
σ_v	0.05								
Database Size ^a (cell,atoms)									
1200K	100,135	100,135							
800K		100,135							
450K		100,135							
300K	100,135	100,135							
Error (TR,TE) ^b									
MAE _e (meV/atom)	0.13,1.53	0.16,1.45	0.04,0.97	0.60,1.24	0.50,1.12	0.52,1.12	0.87,1.20	0.46,1.20	0.93,1.59
MAE _f (eV/Å)	0.07,0.07	0.06,0.07	0.04,0.05	0.04,0.04	0.04,0.04	0.04,0.04	0.04,0.04	0.04,0.04	0.04,0.04
MAE _v (meV/atom)	5.17,6.27	4.58,5.35	2.68,4.03	2.63,3.92	2.53,3.89	2.55,3.75	2.50,3.71	2.43,3.87	2.44,3.64

^a The total number of cells and atoms is split 50:50 in the training and testing sets.

^b TR: training; TE: testing.

Table 5.1: Hyperparameters of the GAP Model. Note that modified values for energy, force and virial are used for a number of sets of configurations.

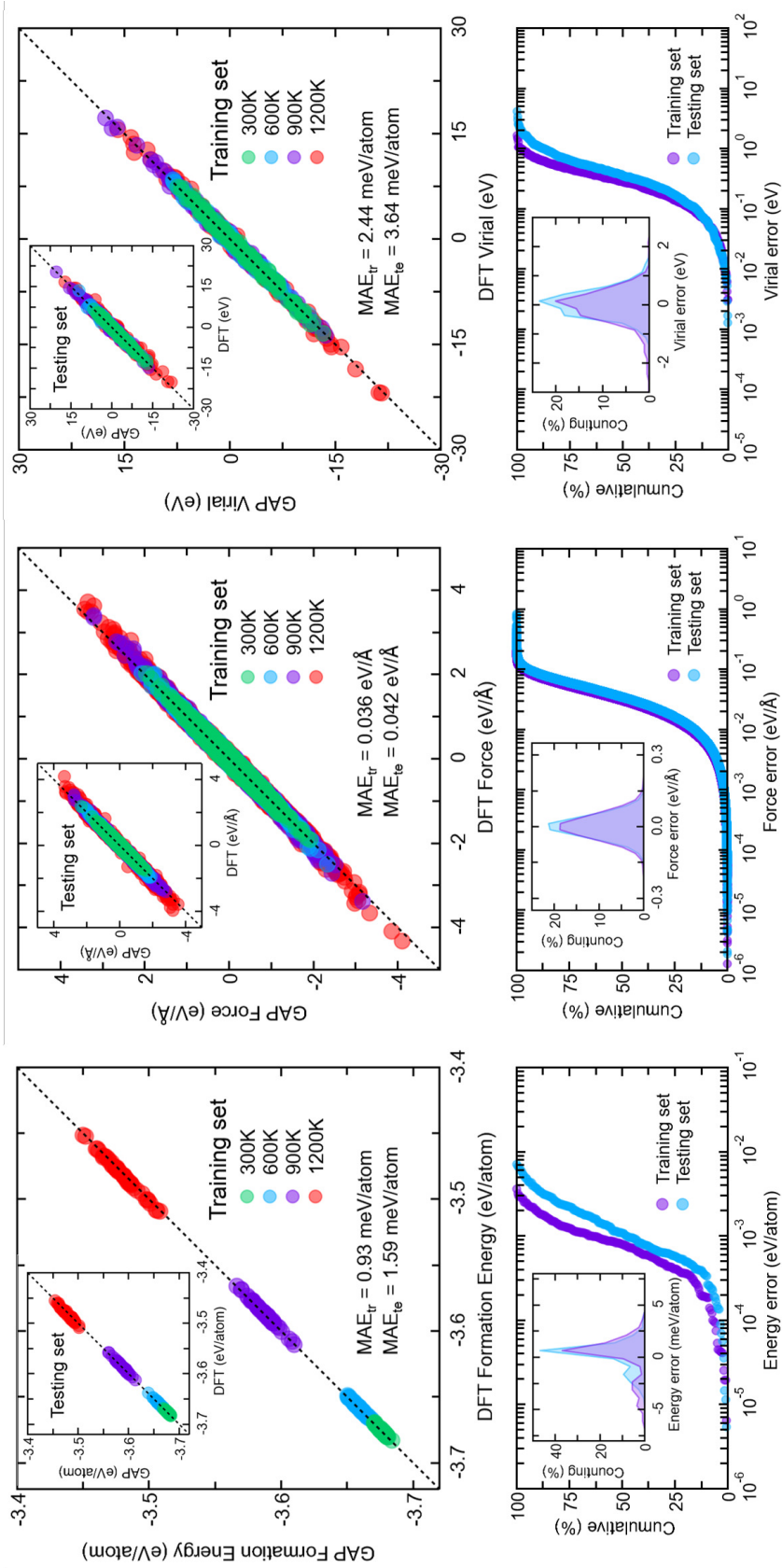


Figure 5.1: Top: Scatter plots of DFT-computed and GAP-predicted total energies (left), forces (centre) and virials (right) for the training and testing (insets) sets of 200 configurations in total. Bottom: Cumulative error distributions: a given point (x,y) on the curve indicates that y percent of all structures have an error equal to or below x. Insets: Absolute errors distributions of the respective quantities obtained for the training and testing sets.

5.3.3 Total X-rays and Neutrons structure factors

The calculated total X-ray and neutron structure factors $S_T^x(k)$ and $S_T^N(k)$ of the glassy Na₃OCl 135 atoms system simulated by means of FPMD at 300 K are shown in Fig. 5.2. Due to the large statistical noise obtained for the structure factors computed directly in the k-space in Fig. 5.2 we show the $S_T(k)$ computed by FFT of the real-space computed pair distribution functions. We remark that $S_T^x(k)$ obtained by FPMD features a first peak at about 2.5 \AA^{-1} and a second peak at about 3.2 \AA^{-1} . These first two peaks are then followed by much broader peaks and rapidly damped oscillations corresponding to a structural correlation length of about 8 \AA^{-1} . The $S_T^N(k)$ obtained by FPMD presents three peaks at $k < 4 \text{ \AA}^{-1}$, the first ($\sim 2.0 \text{ \AA}^{-1}$) and the third ($\sim 3.8 \text{ \AA}^{-1}$) one at higher intensity whereas the second one ($\sim 2.8 \text{ \AA}^{-1}$) at lower intensity. At $k < 4 \text{ \AA}^{-1}$, S_T^N shows much broader peaks and rapidly damped oscillations. The $S_T(k)$ computed for the 135 atoms FPMD model is also compared with the structure factors simulated by MLP by using GAP1, GAP2 GAP3 and GAP4 model sizes (135, 405, 1080 and 3645 atoms). For GAP1, we show both the FFT $S_T(k)$ obtained by one simulation as well as obtained by averaging over 11 replica runs performed starting from a different initial configuration and following the same thermal cycle. For GAP2, GAP3 and GAP4 models, we show both the FFT $S_T(k)$ and the $S_T(k)$ computed by the direct method, averaged over three different independent runs. Our results show very good agreement for both $S_T^x(k)$ and $S_T^N(k)$ between FPMD and GAP1 models over the entire range of k . In particular, the positions and intensities of the main peaks ($k < 4 \text{ \AA}^{-1}$) are very well reproduced. Very small discrepancies occur for larger values of k . We remark a slightly more intense peak for the GAP1 model averaged over 11 runs with respect to the individual GAP1 run and the FPMD data. The $S_T^x(k)$ result of FPMD of 135 systems is not clearly show a shoulder at 2 \AA^{-1} while the GAP results for larger systems (GAP2, GAP3, GAP4) clearly show the peak. Therefore, a FPMD simulation of system containing 405 atoms is calculated. We remark that $S_T^x(k)$ obtained by FPMD features a first peak at about 2.5 \AA^{-1} preceded by a shoulder at about 2.0 \AA^{-1} and a second peak at about 3.2 \AA^{-1} that shows agreement to results of GAP2, GAP3 and GAP4. The shoulder peak is well defined by increasing the system size as shown in Fig 5.2. $S_T^x(k)$ of the glassy Na₃OCl 405 atoms system simulated by means of FPMD has higher first peak intensity following with a lower second peak, and a similar oscillations at higher range as compared to one of 135 atoms. While $S_T^N(k)$ between FPMD and GAP1 models of systems containing 135 atoms are very good consistent the one of 405 atoms system simulated by means of FPMD show agreement of the first peak, following by a higher intensity second peak at a shorter distance in k-space, as consequence with a smaller third peak, and a shoulder at $\sim 3.8 \text{ \AA}^{-1}$. The result are very good agreement to GAP results of larger systems. We remark a slightly less intense for FPMD 405 atoms model compared to GAP3 and GAP4. Very small discrepancies

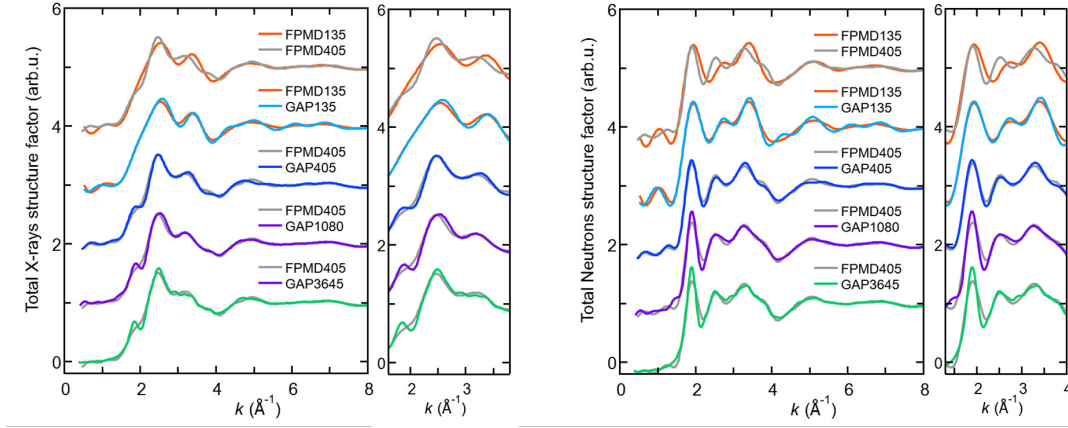


Figure 5.2: Total X-rays and neutrons structure factors for glassy Na_3OCl at $T = 300$ K. The FPMD results (dark grey lines) are compared to the $S_T(k)$ in the reciprocal space (light color) or obtained through Fourier transform of the pair correlation functions with a cutoff value $k_{\text{max}} = 25$ (red lines) for the models at different sizes obtained with MLP-GAP

occur for larger values of k . Overall, $S_T^x(k)$ and $S_T^N(k)$ of the glassy Na_3OCl 405 atoms system simulated by means of FPMD at 300 K show well agreement to ones of GAP2, GAP3, and GAP4.

5.3.4 Total and partial pair correlation functions

In terms of total pair correlation functions, the Na_3OCl one shows a first narrow peak centered at ~ 2.28 Å (with a full width at half maximum (FWHM) of 0.28 Å) and a broader second peak at a lower intensity at ~ 2.77 Å (FWHM of 0.47 Å). Analyzing the partial pair correlation functions $g_{\alpha\beta}(r)$ (Fig. 5.4) allows us to trace back the role of each individual pair contribution with respect to the total one. In Tab. 5.2 we report the nearest-neighbor distances r_{ij} identified by the position of the first maximum of the $g_{\alpha\beta}(r)$ for the three $\text{Na}_{3-x}\text{OH}_x\text{Cl}$ systems. For comparison, we also report the nearest-neighbor distances found in synthesized pure crystalline Na_3OCl . [174, 225] The first peak of $g_{\text{tot}}(r)$ for amorphous Na_3OCl can be ascribed entirely to the Na-O pair (~ 2.28 Å), whereas the second peak is mainly attributed to the Na-Cl pair (~ 2.75 Å) and only partially to Na-O and Na-Na (~ 3.14 Å) $g_{\alpha\beta}(r)$ contributions. The first peak of $g_{\text{NaNa}}(r)$ is responsible for the shoulder occurring after the second peak (~ 2.8 - 3.1 Å) found in the total pair correlation function. Analyzing the peak positions of $g_{\text{NaO}}(r)$ for amorphous Na_3OCl , the Na-O bond distance is found slightly larger than the typical ionic bond reported for crystalline Na_3OCl (~ 2.25 Å), whereas the Na-Cl ionic bond distance is shorter than that of crystalline one (~ 3.18 Å).

The $g_{\text{tot}}(r)$ as obtained from the FPMD and ML-GAP models shows an excellent agreement

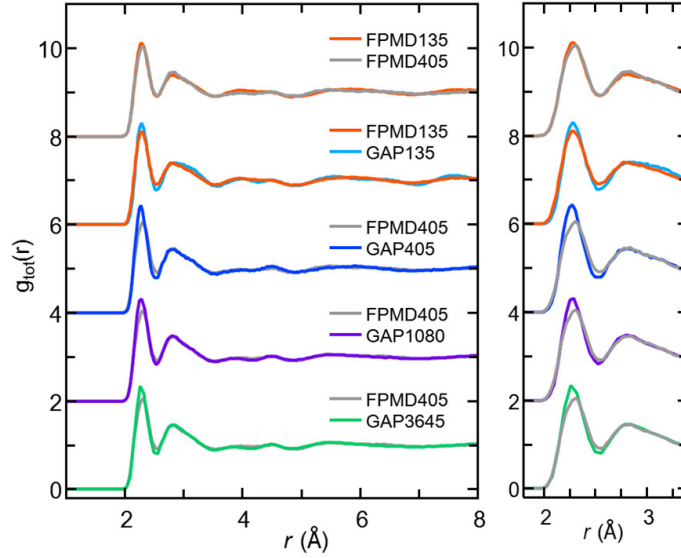


Figure 5.3: Total pair correlation function for amorphous Na_3OCl at $T = 300$ K. The FPMD results (orange black lines) are compared to the MLP calculated for GAP1 (black dashed lines) models and GAP3 (red dashed lines) mode

over the entire real space range. For $r < 3$ Å, the measured first peak shows a slightly lower intensity compared to the modelled one, while the similar intensity case occurs when looking at the second peak for systems having the same size. The measured $g_{\text{tot}}(r)$ are consistent for different cell size systems. While a shoulder peak at around 3.8 Å in $g_{\text{OO}}(r)$, and a higher intensity of first peak in $g_{\text{NaO}}(r)$ are observed when the size of system increasing to 405 atoms in modeled systems as well as measured systems. This discrepancies are typical of cell size effect. Therefore, the system containing 405 atoms is refer as a reference structure for this study. For larger systems size the $g_{\text{tot}}(r)$ show agreements as the measured systems of 405 atoms.

For $r > 5.4$ Å, the FPMD and ML-GAP models reproduce the positions and intensities of the peaks occurring at medium range distances. Overall, these results provide evidences that our models allow for a very good description of the topology of glassy Na_3OCl in comparison to measured results of FPMD. We note also a small reduction of the intensity of the first peak in the ML-GAP model.

Interestingly, the ML-GAP model provides a better description of the O-O correlations in real space where peaks representative of first (around 3.4 Å) and second (around 4.2 Å) coordination shells are well distinguished in comparison to the FPMD model.

	exp	FPMD			GAP			
		Crystal	Amorphous ^a	Amorphous	Amorphous ^b	Amorphous ^c	Amorphous ^d	Amorphous ^e
number of atoms	-	135	135	405	135	405	1080	3645
d (g/cm ³)	2.00	2.14	2.04	2.04	2.04	2.04	2.01	2.02
r_{NaO}	2.25	2.262	2.28	2.30	2.28	2.27	2.27	2.26
r_{NaCl}	3.18	3.206	2.77	2.75	2.75	2.76	2.78	2.79
r_{NaNa}	3.18	3.206	3.20	3.17	3.16	3.15	3.13	3.14
r_{OO}	4.50	4.534	3.83	3.71	3.81	3.72	3.74	3.73
r_{OCl}	3.89	3.937	3.90	3.94	3.95	3.95	3.95	3.90
r_{ClCl}	4.50	4.534	3.96	3.99	4.0	3.86	3.93	3.90
n_{Na}^i	14	14	10.02	9.87	10.08	10.04	10.01	10.02
n_{Na}^p	6	6	4.26	4.28	4.30	4.28	4.30	4.31
n_O^i	6	6	6.68	6.89	6.51	6.93	6.94	6.90
n_O^p	6	6	6.32	6.37	6.03	6.39	6.43	6.40
n_{Cl}^i	12	12	6.70	6.79	6.71	6.74	6.77	6.82
n_{Cl}^p	12	12	6.48	6.47	6.61	6.44	6.49	6.53

^aData averaged over 2 replica runs

^bData averaged over 11 replica runs

^cData averaged over 3 replica runs

^dData averaged over 3 replica runs

^eData averaged over 2 replica runs

Table 5.2: Bond lengths r_{ij} (in Å) in terms of position of the first maximum of the pair correlation functions $g_{ij}(r)$ and average coordination number n obtained by FPMD and MLP models GAP1 and GAP3, respectively. For completeness, we also report the values of the crystalline phase obtained by experiments or previous DFT works.

		FPMD		GAP			
		Amorphous ^a	Amorphous	Amorphous ^b	Amorphous ^c	Amorphous ^d	Amorphous ^e
atoms		135	405	135	405	1080	3645
Na							
l=3		7.56	10.80	5.97	8.20	7.18	7.61
	O ₃	1.95	4.98	2.68	3.34	2.84	3.32
	Cl ₁ O ₂	5.37	5.15	3.13	4.48	4.01	3.95
	Cl ₂ O ₁	0.24	0.67	0.16	0.37	0.38	0.34
l=4		62.97	55.54	62.25	59.49	58.96	57.97
	O ₄	3.96	3.43	2.66	3.74	3.60	3.56
	Cl ₁ O ₃	15.52	17.49	17.51	16.85	17.39	16.94
	Cl ₂ O ₂	34.63	25.86	31.61	28.91	28.32	28.14
	Cl ₃ O ₁	8.12	8.52	10.17	9.64	9.41	9.22
	Cl ₄	0.74	0.24	0.31	0.34	0.24	0.11
l=5		26.66	28.30	27.44	28.51	30.03	30.22
	Cl ₁ O ₄	1.26	0.85	0.79	1.00	1.02	1.02
	Cl ₂ O ₃	3.50	4.93	4.57	5.37	6.03	5.24
	Cl ₃ O ₂	12.83	11.33	12.55	12.38	12.97	13.25
	Cl ₄ O ₁	7.77	9.78	8.68	9.03	9.22	10.29
	Cl ₅	1.31	1.41	0.78	0.71	0.67	0.32
l=6		1.86	4.11	3.71	3.14	2.85	3.22
	Cl ₄ O ₂	1.08	2.75	1.73	1.51	1.64	1.52
	Cl ₅ O ₁	0.78	1.36	1.98	1.63	1.22	1.70
O							
l=5	Na ₅	1.33	3.03	1.31	0.87	0.92	1.13
l=6	Na ₆	68.83	59.45	69.82	62.94	59.32	62.20
l=7	Na ₇	28.15	38.84	26.44	32.25	36.20	32.60
l=8	Na ₈	1.67	2.64	2.38	3.92	3.43	4.05
Cl							
l=4	Na ₄	1.39	1.29	0.71	1.28	1.22	1.12
l=5	Na ₅	13.85	14.26	10.53	13.19	13.50	12.34
l=6	Na ₆	38.34	30.39	35.46	39.11	36.62	36.64
l=7	Na ₇	34.00	32.88	36.04	34.24	34.25	34.52
l=8	Na ₈	11.21	13.34	14.55	10.60	12.63	13.09
l=9	Na ₉	1.15	1.29	2.48	1.57	1.67	2.11

Table 5.3: Distribution of the individual cation-anion $n_{\alpha}(l)$ structural units where an atom of species α (Na, Cl or O) is l -fold coordinated to a counter ion computed for glassy Na₃OCl. In bold are reported the total percentages determined for each l -fold coordination. These quantities have been calculated including neighbours separated by a cutoff corresponding to the first minimum in the $g_{\alpha\beta}(r)$. For the present work, the individual pair cutoffs used are 3.16, 3.94, 4.10, 5.06, 5.51, and 5.39 Å for, respectively, the Na-O, Na-Cl, Na-Na, O-O, Cl-Cl and O-Cl distances. A total cutoff of 3.50 Å was defined from the total $g(r)$.

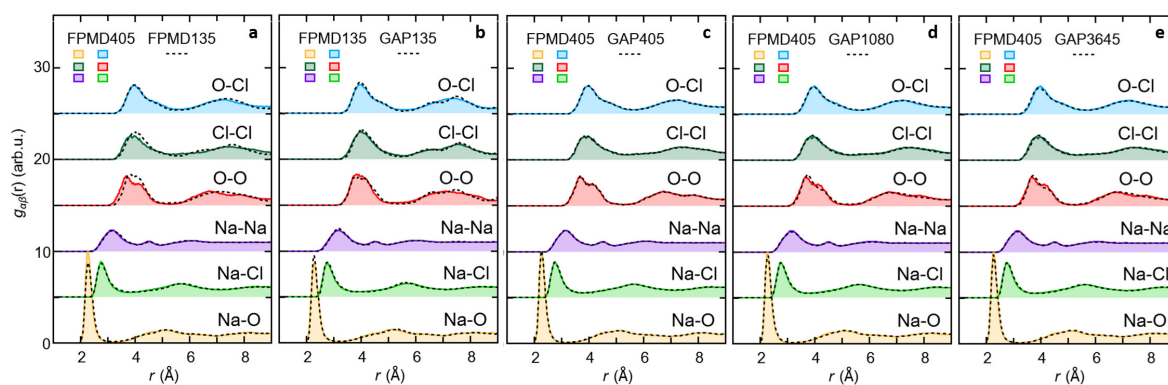


Figure 5.4: The partial pair correlation functions $g_{NaO}(r)$, $g_{NaCl}(r)$, $g_{NaNa}(r)$, $g_{OO}(r)$, $g_{OCl}(r)$ and $g_{ClCl}(r)$ for amorphous Na_3OCl at $T = 300$ K obtained from FPMD (fullfilled profiles) and GAP (dashed lines: black for GAP1 and red for GAP3). The curves are shifted vertically for clarity.

Chapter 6

General conclusions and future perspectives

6.1 Conclusions

We have applied advanced computational methods to assess and comprehend a series of structural and transport properties of Na₃OCl-based systems.

In Chapter 3, we reported and discussed the phase transitions of antiperovskite Na₃OCl through two types of phonon calculations. Quasiharmonic phonon calculations using the quasi-harmonic approximation (QHA) determine the Gibbs free energies of 14 polymorphs, revealing a phase diagram with three stable phases under finite temperature and pressure conditions. At ambient pressure, the high-symmetry cubic phase (Pm $\bar{3}$ m) is stable above 205 K, while the monoclinic phase (P2₁/m) becomes stable below 135 K. In the temperature range of 135 K to 205 K, the Bmmb structure is expected to be the most stable. The second type of phonon calculation incorporates anharmonic terms by utilizing quartic and cubic interatomic force constants (IFCs). Phase-transition temperatures (T_C) are determined using self-consistent phonon calculations and temperature-dependent phonon band structures with the inclusion of the bubble self-energy term (QP-NL). The QP-NL method, which corrects the overestimation of the soft-mode frequency, predicts phase-transition temperatures more than twice as high as those obtained from the SC1 method (54 - 86 K vs 166 - 195 K). Thermal expansion has a negligible effect on T_C in cubic Na₃OCl; however, the study highlights the significance of the soft mode's behavior under lattice constant changes in understanding the thermal expansion effects on T_C . These findings are consistent with previous computational research on other halide perovskites and the experimentally observed room-temperature stability of cubic Na₃OCl. The migration energy barriers of the Na migration are

calculated for the three vibrationally stable phases, revealing similar energy barriers ranging from 0.30 to 0.34 eV across the phases.

In Chapter 4, a quantitative structural characterizations for amorphous antiperovskites in terms of X-ray and neutrons structure factors, pair correlation functions, coordination numbers and chemical identification of the structural units is presented. Our results underscore the significance of conducting quantitative structural assessments to better comprehend the impact of structure on the performances of these systems. Moreover, ion dynamics mechanisms of three amorphous $\text{Na}_{3-x}\text{OH}_x\text{Cl}$ (with $x=0, 0.5, 1$) Na-rich antiperovskites are quantitatively assessed by first-principles molecular dynamics. Amorphous Na_3OCl has a unique microscopic structure that enables remarkable Na ion dynamics and ionic conductivity, challenging that of defective crystalline phases. The presence of hydroxyl OH^- anions in the hydroxylated models is crucial for the mobility of Na ions, which is enhanced by rapid rotation of O-H bonds and paddlewheel-type mechanisms. This promotes the formation of available space, which is essential for achieving fast Na-ion transport. Overall, the study highlights the significance of quantitative structural assessments and sheds light on the ion dynamics mechanisms in amorphous $\text{Na}_{3-x}\text{OH}_x\text{Cl}$ antiperovskites. The findings underscore the potential of these materials for high-performance Na-ion transport and provide insights for further research and development in the field.

In Chapter 5, a more extensive investigation of amorphous Na_3OCl was conducted using first-principles molecular dynamics, enhanced by the development of a machine learning interatomic potential (MLIP). This MLIP enabled us to extend the size and time scales of our simulations, achieving simulations with up to 3645 atoms for durations of up to 100s ps at a given temperature. The MLIP was developed to provide first-principles accuracy, with an energy and forces mean absolute error (MAE) of 0.93 meV/atom and 0.04 eV/Å, respectively. The successful implementation of the MLIP allowed us to establish a critical model size of around 400 atoms for obtaining well-defined X-ray and neutrons structure factors, as well as partial pair correlation functions. Overall, amorphous Na_3OCl was found to exhibit a significantly different structure compared to its crystalline counterpart. It displayed a disordered structure with limited intermediate range order and short-range order, primarily driven by a majority of four-fold coordinated Na atoms (approximately 60%), through ionic bonds with counter-ions. The Na-O bond distances were close to those observed in the crystalline phase, while the Na-Cl distances were notably shorter. Consequently, the local environment surrounding Na atoms in the amorphous phase favored a reduced number of neighboring counter-ions and Na atoms. The majority of Na atoms were coordinated to both O and Cl anions, with only a small percentage exclusively coordinated to O or Cl atoms. These findings reveal contrasting differences in the structure of amorphous Na_3OCl compared

to previously proposed models for glassy Li_3OCl , which were based on the segregation of Li_2O and LiCl -rich regions. The developed MLIP also proved useful for modeling crystalline Na_3OCl , demonstrating an error in the predicted density of approximately 5%.

In conclusion, the results obtained in this study contribute to the growing body of evidence indicating that disordered Na-rich antiperovskites offer a viable and effective alternative to their crystalline counterparts as solid-state electrolytes. The improved understanding of the structural properties of amorphous Na_3OCl , facilitated by the MLIP approach, contributes to the ongoing exploration of materials for advanced energy storage and conversion devices.

6.2 Future perspectives

To achieve high performance in solid-state batteries, the discovery of solid electrolytes with desirable properties is essential. However, the current search for high-performance solid electrolytes is mostly empirical and time-consuming. There is a clear need for new approaches that can accelerate the identification of solid electrolytes with high ionic conductivity, low electronic conductivity, good stability, and compatibility with electrode materials. In this regard, computational studies can play a crucial role in screening and predicting the properties of potential solid electrolytes. The combination of computational modeling and machine learning techniques is driven on one hand to allow a better and detailed comprehension of complex materials such as crystalline and amorphous Na-rich antiperovskites, and on the other hand, expedite the discovery process and reduce the reliance on extensive experimental trials. In line with this perspective, future computational studies can be conducted to investigate the stability and compatibility of solid Na-rich antiperovskite electrolytes with various electrode materials for Na solid-state batteries. The development of MLIP models that accurately predict the behavior of the electrolyte/electrode interface in these batteries can be a valuable tool. These models can be trained on large datasets that capture the complex relationships between materials, their structures, and the electrochemical processes involved in battery operation. With respect to the GAP-MLIP developed in this PhD thesis, two possible future steps might be undertaken in order to develop a MLIP able to model also the electrolyte/electrode interface: i. enrich the existing DFT database of metallic Na phases as well as DFT-modelled $\text{Na}_3\text{OCl}@Na$ interface models and exploit the same GAP fitting scheme and ii. develop a GAP-type MLIP by fitting to the energy and force differences that Na ions induce in at the $\text{Na}_3\text{OCl}@Na$ interface by following the recent scheme proposed by Fujikake et al. [258].

Furthermore, by incorporating a broad range of experimental and simulation data, including information on electrode materials, solid electrolyte properties, interface characteristics, and battery performance metrics, such as energy density, power density, and

cycling stability, these models can provide insights and predictions that guide the design and optimization of Na solid-state batteries.

An second important aspect to explore is the role of defects in the performance of Na solid-state electrolytes and their interfaces with electrodes. Defects can significantly impact the ionic conductivity and stability of solid electrolytes, as well as influence the interfacial behavior between the electrolyte and electrode. Computational investigations can delve into the effects of different defect types, concentrations, and distributions on the overall performance of the battery system. This knowledge can guide the design and engineering of defect-controlled solid electrolytes with enhanced properties and improved interface behavior, ultimately leading to the development of more efficient and reliable sodium solid-state batteries.

In conclusion, the combination of computational modeling, machine learning techniques, and thorough investigations into the role of defects holds great promise for accelerating the discovery and optimization of high-performance solid electrolytes for sodium solid-state batteries. These approaches can provide valuable insights into the structure-property relationships, stability, and compatibility of solid electrolytes and their interfaces, thereby facilitating the development of next-generation energy storage technologies. By reducing the reliance on empirical approaches and enabling more targeted material design, computational studies can contribute to the advancement of solid-state battery technology and the realization of sustainable and efficient energy storage systems.

References

- [1] J.-M. Tarascon and M. Armand. Issues and challenges facing rechargeable lithium batteries. *Nature*, 414(6861):359–367, November 2001.
- [2] Wei Xia, Yang Zhao, Feipeng Zhao, Keegan Adair, Ruo Zhao, Shuai Li, Ruqiang Zou, Yusheng Zhao, and Xueliang Sun. Antiperovskite Electrolytes for Solid-State Batteries. *Chemical Reviews*, 122(3):3763–3819, 2022.
- [3] Noriaki Kamaya, Kenji Homma, Yuichiro Yamakawa, Masaaki Hirayama, Ryoji Kanno, Masao Yonemura, Takashi Kamiyama, Yuki Kato, Shigenori Hama, Koji Kawamoto, and Akio Mitsui. A lithium superionic conductor. *Nature Materials*, 10(9):682–686, September 2011.
- [4] P. Padma Kumar and S. Yashonath. Ionic conduction in the solid state. *Journal of Chemical Sciences*, 118(1):135–154, January 2006.
- [5] Hans-Jorg Deiseroth, Shiao-Tong Kong, Hellmut Eckert, Julia Vannahme, Christof Reiner, Torsten Zaiss, and Marc Schlosser. Li₆PS₅X: a class of crystalline Li-rich solids with an unusually high Li⁺ mobility. *Angewandte Chemie (International Ed. in English)*, 47(4):755–758, 2008.
- [6] Chengwei Wang, Kun Fu, Sanoop Palakkathodi Kammampata, Dennis W. McOwen, Alfred Junio Samson, Lei Zhang, Gregory T. Hitz, Adelaide M. Nolan, Eric D. Wachsman, Yifei Mo, Venkataraman Thangadurai, and Liangbing Hu. Garnet-Type Solid-State Electrolytes: Materials, Interfaces, and Batteries. *Chemical Reviews*, 120(10):4257–4300, 2020.
- [7] John Christopher Bachman, Sokseiha Muy, Alexis Grimaud, Hao-Hsun Chang, Nir Pour, Simon F. Lux, Odysseas Paschos, Filippo Maglia, Saskia Lupart, Peter Lamp, Livia Giordano, and Yang Shao-Horn. Inorganic Solid-State Electrolytes for Lithium Batteries: Mechanisms and Properties Governing Ion Conduction. *Chemical Reviews*, 116(1):140–162, 2016.

- [8] Renjie Chen, Wenjie Qu, Xing Guo, Li Li, and Feng Wu. The pursuit of solid-state electrolytes for lithium batteries: from comprehensive insight to emerging horizons. *Materials Horizons*, 3(6):487–516, October 2016.
- [9] Wenjia Zhao, Jin Yi, Ping He, and Haoshen Zhou. Solid-State Electrolytes for Lithium-Ion Batteries: Fundamentals, Challenges and Perspectives. *Electrochemical Energy Reviews*, 2(4):574–605, 2019.
- [10] Yonggang Wang, Hao Zhang, Jinlong Zhu, Xujie Lu, Shuai Li, Ruqiang Zou, and Yusheng Zhao. Antiperovskites with Exceptional Functionalities. *Advanced Materials*, 32(7):1905007, 2020.
- [11] Yusheng Zhao and Luke L. Daemen. Superionic Conductivity in Lithium-Rich Anti-Perovskites. *Journal of the American Chemical Society*, 134(36):15042–15047, 2012.
- [12] Yan Wang, William Davidson Richards, Shyue Ping Ong, Lincoln J. Miara, Jae Chul Kim, Yifei Mo, and Gerbrand Ceder. Design principles for solid-state lithium superionic conductors. *Nature Materials*, 14(10):1026–1031, 2015.
- [13] Takao Inoue and Kazuhiko Mukai. Are All-Solid-State Lithium-Ion Batteries Really Safe?-Verification by Differential Scanning Calorimetry with an All-Inclusive Microcell. *ACS Applied Materials & Interfaces*, 9(2):1507–1515, 2017.
- [14] Qing Zhao, Sanjuna Stalin, Chen-Zi Zhao, and Lynden A. Archer. Designing solid-state electrolytes for safe, energy-dense batteries. *Nature Reviews Materials*, 5(3):229–252, 2020.
- [15] Teyeb Ould Ely, Dana Kamzabek, and Dhritiman Chakraborty. Batteries Safety: Recent Progress and Current Challenges. *Frontiers in Energy Research*, 7, 2019.
- [16] John A. Lewis, Jared Tippens, Francisco Javier Quintero Cortes, and Matthew T. McDowell. Chemo-Mechanical Challenges in Solid-State Batteries. *Trends in Chemistry*, 1(9):845–857, 2019.
- [17] Kelsey B. Hatzell, Xi Chelsea Chen, Corie L. Cobb, Neil P. Dasgupta, Marm B. Dixit, Lauren E. Marbella, Matthew T. McDowell, Partha P. Mukherjee, Ankit Verma, Venkatasubramanian Viswanathan, Andrew S. Westover, and Wolfgang G. Zeier. Challenges in Lithium Metal Anodes for Solid-State Batteries. *ACS Energy Letters*, 5(3):922–934, 2020.

- [18] Thorben Krauskopf, Felix H. Richter, Wolfgang G. Zeier, and Jürgen Janek. Physicochemical Concepts of the Lithium Metal Anode in Solid-State Batteries. *Chemical Reviews*, 120(15):7745–7794, 2020.
- [19] Yuming Chen, Ziqiang Wang, Xiaoyan Li, Xiahui Yao, Chao Wang, Yutao Li, Weijiang Xue, Daiwei Yu, So Yeon Kim, Fei Yang, Akihiro Kushima, Guoge Zhang, Haitao Huang, Nan Wu, Yiu-Wing Mai, John B. Goodenough, and Ju Li. Li metal deposition and stripping in a solid-state battery via Coble creep. *Nature*, 578(7794):251–255, 2020.
- [20] Paul Albertus, Venkataramani Anandan, Chunmei Ban, Nitash Balsara, Ilias Belharouak, Josh Buettner-Garrett, Zonghai Chen, Claus Daniel, Marca Doeff, Nancy J. Dudney, Bruce Dunn, Stephen J. Harris, Subramanya Herle, Eric Herbert, Sergiy Kalnaus, Joseph A. Libera, Dongping Lu, Steve Martin, Bryan D. McCloskey, Matthew T. McDowell, Y. Shirley Meng, Jagjit Nanda, Jeff Sakamoto, Ethan C. Self, Sanja Tepavcevic, Eric Wachsman, Chunsheng Wang, Andrew S. Westover, Jie Xiao, and Thomas Yersak. Challenges for and Pathways toward Li-Metal-Based All-Solid-State Batteries. *ACS Energy Letters*, 6(4):1399–1404, 2021.
- [21] Kian Kerman, Alan Luntz, Venkatasubramanian Viswanathan, Yet-Ming Chiang, and Zhebo Chen. Review-practical challenges hindering the development of solid state lithium batteries. *Journal of The Electrochemical Society*, 164(7):A1731–A1744, 2017.
- [22] Shuaifeng Lou, Fang Zhang, Chuankai Fu, Ming Chen, Yulin Ma, Geping Yin, and Jiajun Wang. Interface Issues and Challenges in All-Solid-State Batteries: Lithium, Sodium, and Beyond. *Advanced Materials*, 33(6):2000721, 2021.
- [23] Jun Haruyama, Keitaro Sodeyama, Liyuan Han, Kazunori Takada, and Yoshitaka Tateyama. Space charge Layer Effect at Interface between Oxide Cathode and Sulfide Electrolyte in All-Solid-State Lithium-Ion Battery. *Chemistry of Materials*, 26(14):4248–4255, July 2014.
- [24] Saskia Stegmaier, Johannes Voss, Karsten Reuter, and Alan C. Luntz. Li⁺ Defects in a Solid-State Li Ion Battery: Theoretical Insights with a Li₃OCl Electrolyte. *Chemistry of Materials*, 29(10):4330–4340, 2017. Publisher: American Chemical Society.
- [25] Yiran Xiao, Kostiantyn Turcheniuk, Aashray Narla, Ah-Young Song, Xiaolei Ren, Alexandre Magasinski, Ayush Jain, Shirley Huang, Haewon Lee, and Gleb Yushin. Electrolyte melt infiltration for scalable manufacturing of inorganic all-solid-state lithium-ion batteries. *Nature Materials*, 20(7):984–990, 2021.

- [26] M. H. Braga, N. S. Grundish, A. J. Murchison, and J. B. Goodenough. Alternative strategy for a safe rechargeable battery. *Energy & Environmental Science*, 10(1):331–336, 2017.
- [27] Bertold Reuter and Kurt Hardel. Silbersulfidbromid Ag_3SBr und Silbersulfidjodid Ag_3SJ . I. Darstellung, Eigenschaften und Phasenverhältnisse von Ag_3SBr und Ag_3SJ . *Zeitschrift für anorganische und allgemeine Chemie*, 340(3-4):158–167, 1965.
- [28] Bertold Reuter and Kurt Hardel. Silbersulfidbromid Ag_3SBr und Silbersulfidjodid Ag_3SJ . III. Die Halbleitereigenschaften von Ag_3SBr , Ag_3SJ . *Berichte der Bunsengesellschaft für physikalische Chemie*, 70(1):82–86, 1966.
- [29] Winfried Müller and Martin Jansen. $(\text{CN})\text{ONa}_3$, Kristallstruktur und Natriumionenleitfähigkeit. *Zeitschrift für anorganische und allgemeine Chemie*, 591(1):41–46, 1990.
- [30] O. Nakamura and J. B. Goodenough. Conductivity enhancement of lithium bromide monohydrate by Al_2O_3 particles. *Solid State Ionics*, 7(2):119–123, 1982.
- [31] Georg Schwing, Andreas Honnerscheid, Leo van Wüllen, and Martin Jansen. High Lithium Ionic Conductivity in the Lithium Halide Hydrates $\text{Li}_3\text{-n}(\text{OHn})\text{Cl}$ and $\text{Li}_3\text{-n}(\text{OHn})\text{Br}$ at Ambient Temperatures. *ChemPhysChem*, 4(4):343–348, 2003.
- [32] Yutao Li, Weidong Zhou, Sen Xin, Shuai Li, Jinlong Zhu, Xujie Lu, Zhiming Cui, Quanxi Jia, Jianshi Zhou, Yusheng Zhao, and John B. Goodenough. Fluorine-Doped Antiperovskite Electrolyte for All-Solid-State Lithium-Ion Batteries. *Angewandte Chemie International Edition*, 55(34):9965–9968, 2016.
- [33] G. L. Gutsev and A. I. Boldyrev. DVM-X^\pm calculations on the ionization potentials of MX_{k+1}^- complex anions and the electron affinities of MX_{k+1} superhalogens. *Chemical Physics*, 56(3):277–283, 1981.
- [34] Puru Jena and Qiang Sun. Super Atomic Clusters: Design Rules and Potential for Building Blocks of Materials. *Chemical Reviews*, 118(11):5755–5870, June 2018.
- [35] Jinlong Zhu, Shuai Li, Yi Zhang, John W. Howard, Xujie Lu, Yutao Li, Yonggang Wang, Ravhi S. Kumar, Liping Wang, and Yusheng Zhao. Enhanced ionic conductivity with $\text{Li}_7\text{O}_2\text{Br}_3$ phase in Li_3OBr anti-perovskite solid electrolyte. *Applied Physics Letters*, 109(10):101904, September 2016.

- [36] Jinlong Zhu, Yonggang Wang, Shuai Li, John W. Howard, Jorg Neufeind, Yang Ren, Hui Wang, Chengdu Liang, Wenge Yang, Ruqiang Zou, Changqing Jin, and Yusheng Zhao. Sodium Ion Transport Mechanisms in Antiperovskite Electrolytes Na_3OBr and Na_4OI_2 : An *in Situ* Neutron Diffraction Study. *Inorganic Chemistry*, 55(12):5993–5998, June 2016.
- [37] Yuran Yu, Zhuo Wang, and Guosheng Shao. Theoretical tuning of Ruddlesden-Popper type anti-perovskite phases as superb ion conductors and cathodes for solid sodium ion batteries. *Journal of Materials Chemistry A*, 7(17):10483–10493, 2019.
- [38] M. H. Braga, J. A. Ferreira, V. Stockhausen, J. E. Oliveira, and A. El-Azab. Novel Li_3ClO based glasses with superionic properties for lithium batteries. *Journal of Materials Chemistry A*, 2(15):5470–5480, 2014.
- [39] M. Helena Braga, Andrew J. Murchison, Jorge A. Ferreira, Preetam Singh, and John B. Goodenough. Glass-amorphous alkali-ion solid electrolytes and their performance in symmetrical cells. *Energy & Environmental Science*, 9(3):948–954, 2016.
- [40] Fudong Han, Andrew S. Westover, Jie Yue, Xiulin Fan, Fei Wang, Miaofang Chi, Donovan N. Leonard, Nancy J. Dudney, Howard Wang, and Chunsheng Wang. High electronic conductivity as the origin of lithium dendrite formation within solid electrolytes. *Nature Energy*, 4(3):187–196, March 2019.
- [41] Maria Helena Braga, Chandrasekar M Subramaniam, Andrew J. Murchison, and John B. Goodenough. Nontraditional, Safe, High Voltage Rechargeable Cells of Long Cycle Life. *Journal of the American Chemical Society*, 140(20):6343–6352, May 2018.
- [42] James A. Dawson, Theodosios Famprikis, and Karen E. Johnston. Anti-perovskites for solid-state batteries: recent developments, current challenges and future prospects. *Journal of Materials Chemistry A*, 9(35):18746–18772, 2021.
- [43] Jingfeng Zheng, Brian Perry, and Yiyang Wu. Antiperovskite Superionic Conductors: A Critical Review. *ACS Materials Au*, 1(2):92–106, 2021.
- [44] Isabel Hanghofer, Gunther J. Redhammer, Sebastian Rohde, Ilie Hanzu, Anatoliy Senyshyn, H. Martin R. Wilkening, and Daniel Rettenwander. Untangling the Structure and Dynamics of Lithium-Rich Anti-Perovskites Envisaged as Solid Electrolytes for Batteries. *Chemistry of Materials*, 30(22):8134–8144, November 2018.

- [45] Yijun Tian, Fei Ding, Hai Zhong, Cheng Liu, Yan-Bing He, Jiaquan Liu, Xingjiang Liu, and Qiang Xu. $\text{Li}_{6.75}\text{La}_3\text{Zr}_{1.75}\text{Ta}_{0.25}\text{O}_{12}$ amorphous Li_3OCl composite electrolyte for solid state lithium-metal batteries. *Energy Storage Mater.*, 14:49–57, sep 2018.
- [46] Ashim Gurung, Jyotshna Pokharel, Abiral Baniya, Rajesh Pathak, Ke Chen, Buddhi Sagar Lamsal, Nabin Ghimire, Wen-Hua Zhang, Yue Zhou, and Qiquan Qiao. A review on strategies addressing interface incompatibilities in inorganic all-solid-state lithium batteries. *Sustainable Energy & Fuels*, 3(12):3279–3309, November 2019.
- [47] Edgar D. Zotto and John C. Mauro. The glassy state of matter: Its definition and ultimate fate. *Journal of Non-Crystalline Solids*, 471:490–495, September 2017.
- [48] Arun K. Varshneya and John C. Mauro. Comment on misconceived ASTM definition of Glass by A. C. wright. *Glass Technology*, 51(1):28–30, 2010.
- [49] Juraj Mavracic, Felix C. Mocanu, Volker L. Deringer, Gabor Csanyi, and Stephen R. Elliott. Similarity Between Amorphous and Crystalline Phases: The Case of TiO_2 . *The Journal of Physical Chemistry Letters*, 9(11):2985–2990, 2018.
- [50] K. Hippler, S. Sitta, P. Vogt, and H. Sabrowsky. Structure of Na_3OCl . *Acta Crystallogr. C*, 46(5):736–738, 1990.
- [51] Ernest Ahiavi, James Dawson, Ulaş Kudu, Matthieu Courty, M. Saiful Islam, Oliver Clemens, Christian Masquelier, and Theodosios Famprikis. Mechanochemical synthesis and ion transport properties of Na_3OX ($X = \text{Cl}, \text{Br}, \text{I}$ and BH_4) antiperovskite solid electrolytes. *Journal of Power Sources*, 471:228489, 2020.
- [52] Alexei A. Maradudin, George H. Weiss, and E. W. Montroll. *Theory of lattice dynamics in the harmonic approximation*. Solid state physics. Academic Press, New York, 1963.
- [53] Kerson Huang. *Statistical Mechanics, 2nd Edition*. Wiley, New York, 2nd edition edition, January 1991.
- [54] Martin T. Dove. *Introduction to Lattice Dynamics*. Cambridge University Press, Cambridge ; New York, 1 edition edition, November 1993.
- [55] A. A. Maradudin and A. E. Fein. Scattering of Neutrons by an Anharmonic Crystal. *Physical Review*, 128(6), December 1962.
- [56] Terumasa Tadano and Shinji Tsuneyuki. Self-consistent phonon calculations of lattice dynamical properties in cubic SrTiO_3 with first-principles anharmonic force constants. *Physical Review B*, 92(5), August 2015.

- [57] Martin T. Dove. Theory of displacive phase transitions in minerals. *American Mineralogist*, 82(3-4):213–244, April 1997.
- [58] A. D. Bruce and R. A. Cowley. *Structural Phase Transitions*. Taylor & Francis, 1981.
- [59] S. Kurth, M. A. L. Marques, and E. K. U. Gross. Density-Functional Theory. In *Encyclopedia of Condensed Matter Physics*, pages 395–402. Elsevier, Oxford, 2005.
- [60] Karl Whittle. *Nuclear Materials Science (Second Edition)*. IOP Publishing, nov 2020.
- [61] P. Hohenberg and W. Kohn. Inhomogeneous Electron Gas. *Physical Review*, 136(3B), November 1964.
- [62] W. Kohn and L. J. Sham. Self-Consistent Equations Including Exchange and Correlation Effects. *Physical Review*, 140(4A), November 1965.
- [63] H. Toulhoat. Heterogeneous Catalysis: Use of Density Functional Theory. In K. H. Jurgen Buschow, Robert W. Cahn, Merton C. Flemings, Bernhard Ilschner, Edward J. Kramer, Subhash Mahajan, and Patrick Veysseyre, editors, *Encyclopedia of Materials: Science and Technology*, pages 1–7. Elsevier, Oxford, January 2010.
- [64] Robert G. Parr and Yang Weitao. *Density-Functional Theory of Atoms and Molecules*. Oxford University Press, New York, NY, May 1994.
- [65] M. Born and R. Oppenheimer. Zur Quantentheorie der Molekeln. *Annalen der Physik*, 389(20):457–484, January 1927.
- [66] D. R. Hartree. The Wave Mechanics of an Atom with a Non-Coulomb Central Field. Part I. Theory and Methods. *Mathematical Proceedings of the Cambridge Philosophical Society*, 24(1), January 1928.
- [67] L. H. Thomas. The calculation of atomic fields. *Mathematical Proceedings of the Cambridge Philosophical Society*, 23(5):542–548, January 1927.
- [68] Yayun Hu, G. Murthy, Sumathi Rao, and J. K. Jain. Kohn-Sham density functional theory of Abelian anyons. *Physical Review B*, 103(3), January 2021.
- [69] J. P. Perdew and Alex Zunger. Self-interaction correction to density-functional approximations for many-electron systems. *Physical Review B*, 23(10), May 1981.
- [70] John P. Perdew and Yue Wang. Accurate and simple analytic representation of the electron-gas correlation energy. *Physical Review B*, 45(23):13244–13249, June 1992.

- [71] John P. Perdew, Kieron Burke, and Matthias Ernzerhof. Generalized Gradient Approximation Made Simple. *Physical Review Letters*, 77(18):3865–3868, October 1996.
- [72] P. J. Stephens, F. J. Devlin, C. F. Chabalowski, and M. J. Frisch. Ab Initio Calculation of Vibrational Absorption and Circular Dichroism Spectra Using Density Functional Force Fields. *The Journal of Physical Chemistry*, 98(45), November 1994.
- [73] John P. Perdew, Matthias Ernzerhof, and Kieron Burke. Rationale for mixing exact exchange with density functional approximations. *The Journal of Chemical Physics*, 105(22), 1996.
- [74] Yingkai Zhang and Weitao Yang. Generalized Gradient Approximation Made Simple. *Physical Review Letters*, 80(4):890–890, January 1998. Publisher: American Physical Society.
- [75] John P. Perdew, Adrienn Ruzsinszky, Gábor I. Csonka, Oleg A. Vydrov, Gustavo E. Scuseria, Lucian A. Constantin, Xiaolan Zhou, and Kieron Burke. Restoring the Density-Gradient Expansion for Exchange in Solids and Surfaces. *Physical Review Letters*, 100(13):136406, April 2008.
- [76] Peter Schwerdtfeger. The Pseudopotential Approximation in Electronic Structure Theory. *ChemPhysChem*, 12(17):3143–3155, 2011.
- [77] G. Kresse and D. Joubert. From Ultrasoft Pseudopotentials to the Projector Augmented-Wave Method. *Physical Review B*, 59(3):1758, January 1999.
- [78] R. Car and M. Parrinello. Unified Approach for Molecular Dynamics and Density-Functional Theory. *Physical Review Letters*, 55(22):2471–2474, November 1985.
- [79] Mauro Boero, Assil Bouzid, Sebastien Le Roux, Burak Ozdamar, and Carlo Massobrio. First-Principles Molecular Dynamics Methods: An Overview. In *Molecular Dynamics Simulations of Disordered Materials: From Network Glasses to Phase-Change Memory Alloys*, Springer Series in Materials Science, pages 33–55. Springer International Publishing, Cham, 2015.
- [80] Yuan-Bin Liu, Jia-Yue Yang, Gong-Ming Xin, Lin-Hua Liu, Gábor Csányi, and Bing-Yang Cao. Machine learning interatomic potential developed for molecular simulations on thermal properties of β - Ga_2O_3 . *The Journal of Chemical Physics*, 153(14):144501, October 2020.

- [81] Ganesh Sivaraman, Anand Narayanan Krishnamoorthy, Matthias Baur, Christian Holm, Marius Stan, Gábor Csányi, Chris Benmore, and Álvaro Vázquez-Mayagoitia. Machine-learned interatomic potentials by active learning: amorphous and liquid hafnium dioxide. *npj Computational Materials*, 6(1):1–8, July 2020.
- [82] Y. Mishin. Machine-learning interatomic potentials for materials science. *Acta Materialia*, 214:116980, August 2021.
- [83] Volker L. Deringer, Miguel A. Caro, and Gábor Csányi. Machine Learning Interatomic Potentials as Emerging Tools for Materials Science. *Advanced Materials*, 31(46):1902765, 2019.
- [84] Volker L Deringer. Modelling and understanding battery materials with machine-learning-driven atomistic simulations. *Journal of Physics: Energy*, 2(4):041003, October 2020.
- [85] Jorg Behler and Michele Parrinello. Generalized Neural-Network Representation of High-Dimensional Potential-Energy Surfaces. *Physical Review Letters*, 98(14):146401, April 2007.
- [86] Albert P. Bartók, Mike C. Payne, Risi Kondor, and Gábor Csányi. Gaussian Approximation Potentials: The Accuracy of Quantum Mechanics, without the Electrons. *Physical Review Letters*, 104(13), April 2010.
- [87] Volker L. Deringer, Albert P. Bartók, Noam Bernstein, David M. Wilkins, Michele Ceriotti, and Gábor Csányi. Gaussian Process Regression for Materials and Molecules. *Chemical Reviews*, 121(16):10073–10141, August 2021.
- [88] T. He, Q. Huang, A. P. Ramirez, Y. Wang, K. A. Regan, N. Rogado, M. A. Hayward, M. K. Haas, J. S. Slusky, K. Inumara, H. W. Zandbergen, N. P. Ong, and R. J. Cava. Superconductivity in the non-oxide perovskite MgCNi₃. *Nature*, 411(6833):54–56, may 2001.
- [89] Ying Sun, Cong Wang, Lihua Chu, Yongchun Wen, Man Nie, and Fusheng Liu. Low temperature coefficient of resistivity induced by magnetic transition and lattice contraction in Mn₃in compound. *Scr. Mater.*, 62(9):686–689, May 2010.
- [90] P. Tong and Y. P. Sun. Research Progress on Ni-Based Antiperovskite Compounds. *Adv. Cond. Matter Phys.*, 2012, 2012.

- [91] Alexandra Emly, Emmanouil Kioupakis, and Anton Van der Ven. Phase Stability and Transport Mechanisms in Antiperovskite Li_3OCl and Li_3OBr Superionic Conductors. *Chem. Mater.*, 25:4663–4670, December 2013.
- [92] M. Bilal, S. Jalali-Asadabadi, Rashid Ahmad, and Iftikhar Ahmad. Electronic Properties of antiperovskite Materials from State-of-the-Art Density Functional Theory. *J. Chem.*, 2015:e495131, March 2015.
- [93] Daichi Matsunami, Asaya Fujita, Koshi Takenaka, and Mika Kano. Giant barocaloric effect enhanced by the frustration of the antiferromagnetic phase in Mn_3GaN . *Nat. Mater.*, 14(1):73–78, October 2014.
- [94] Abdus Samad, Mohammad Noor-A-Alam, and Young-Han Shin. First principles study of a $\text{SnS}_2/\text{graphene}$ heterostructure: a promising anode material for rechargeable Na ion batteries. *J. Mater. Chem. A*, 4:14316–14323, sep 2016.
- [95] Abdus Samad, Aamir Shafique, and Young-Han Shin. Adsorption and diffusion of mono, di, and trivalent ions on two-dimensional TiS_2 . *Nanotechnology*, 28:175401, 2017.
- [96] Abdus Samad, Aamir Shafique, Hye Jung Kim, and Young-Han Shin. Superionic and electronic conductivity in monolayer W_2C : ab initio predictions. *J. Mater. Chem. A*, 5:11094–11099, June 2017.
- [97] Abdus Samad and Young-Han Shin. $\text{MoS}_2@ \text{VS}_2$ Nanocomposite as a Superior Hybrid Anode Material. *ACS Appl. Mater. Interfaces*, 9:29942–29949, September 2017.
- [98] Han Nguyen, Sunny Hy, Erik Wu, Zhi Deng, Mojtaba Samiee, Thomas Yersak, Jian Luo, Shyue Ping Ong, and Ying Shirley Meng. Experimental and Computational Evaluation of a Sodium-Rich Anti-Perovskite for Solid State Electrolytes. *J. Electrochem. Soc.*, 163(10):A2165–A2171, 2016.
- [99] Min-Hua Chen, Alexandra Emly, and Anton Van der Ven. Anharmonicity and phase stability of antiperovskite Li_3OCl . *Phys. Rev. B*, 91:214306, June 2015.
- [100] A. M. Glazer. The classification of tilted octahedra in perovskites. *Acta Crystallogr. B Struct. Crystallogr. and Crystal Chem.*, 28(11):3384–3392, 1972.
- [101] C. J. Howard and H. T. Stokes. Group-theoretical analysis of octahedral tilting in perovskites. *Acta Crystallogr. B*, 54(6):782–789, 1998.

- [102] Yi Zhang, Yusheng Zhao, and Changfeng Chen. Ab initio study of the stabilities of and mechanism of superionic transport in lithium-rich antiperovskites. *Phys. Rev. B*, 87:134303, April 2013.
- [103] V. I. Zinenko and N. G. Zamkova. Lattice dynamics of antiperovskite structure compounds a_3ox ($a=na, k; x=ci, br$). *Ferroelectrics*, 265(1):23–29, January 2002.
- [104] Shakeel Ahmad Khandy, Ishtihadah Islam, Amel Laref, Mathias Gogolin, Aurangzeb K. Hafiz, and Azher M. Siddiqui. Electronic structure, thermomechanical and phonon properties of inverse perovskite oxide (Na_3OCl): An ab initio study. *Int. J. Energy Res.*, 44(4):2594–2603, 2020.
- [105] Tan-Lien Pham, Abdus Samad, Hye Jung Kim, and Young-Han Shin. Computational predictions of stable phase for antiperovskite Na_3OCl via tilting of Na_6O octahedra. *J. Appl. Phys.*, 124(16):164106, 2018.
- [106] Terumasa Tadano and Wissam A. Saidi. First-principles phonon quasiparticle theory applied to a strongly anharmonic halide perovskite. *Phys. Rev. Lett.*, 129:185901, Oct 2022.
- [107] Terumasa Tadano and Shinji Tsuneyuki. Quartic Anharmonicity of Rattlers and Its Effect on Lattice Thermal Conductivity of Clathrates from First Principles. *Phys. Rev. Lett.*, 120(10):105901, 2018.
- [108] Ioanna Pallikara, Prakriti Kayastha, Jonathan M Skelton, and Lucy D Whalley. The physical significance of imaginary phonon modes in crystals. *Electronic Structure*, 4(3):033002, September 2022.
- [109] Marisa C. Oliveira, Renan A. P. Ribeiro, Elson Longo, Maurício R. D. Bomio, Fabiana V. Motta, and Sergio R. de Lazaro. Temperature dependence on phase evolution in the $BaTiO_3$ polytypes studied using ab initio calculations. *Int. J. Quantum Chem.*, 120(1):e26054, 2020.
- [110] Meng-Jun Zhou, Yi Wang, Yanzhou Ji, Zi-Kui Liu, Long-Qing Chen, and Ce-Wen Nan. First-principles lattice dynamics and thermodynamic properties of pre-perovskite $PbTiO_3$. *Acta Mater.*, 171:146–153, 2019.
- [111] T. Famprakis J. Dawson and K.E. Johnston. Anti-perovskites for solid-state batteries: recent developments, current challenges and future prospects. *J. Mater. Chem.*, 9:18746–18772, 2021.

- [112] G. Kresse and J. Furthmüller. Efficient Iterative Schemes for ab Initio Total Energy Calculations Using a Plane-Wave Basis Set. *Phys. Rev. B*, 54(16):11169–11186, October 1996.
- [113] Atsushi Togo and Isao Tanaka. First principles phonon calculations in materials science. *Scr. Mater.*, 108:1–5, November 2015.
- [114] Anton Kokalj. XCrySDen a new program for displaying crystalline structures and electron densities. *J. Mol. Graph. Model.*, 17(3):176–179, June 1999.
- [115] V. Krukau Aliaksandr, A. Vydrov Oleg, F. Izmaylov Artur, and E. Scuseria Gustavo. Influence of the exchange screening parameter on the performance of screened hybrid functionals. *J. Chem. Phys.*, 125(22):224106, December 2006.
- [116] Dario Alfé. PHON: A program to calculate phonons using the small displacement method. *Comput. Phys. Commun.*, 180(12):2622–2633, 2009.
- [117] Laurent Chaput, Atsushi Togo, Isao Tanaka, and Gilles Hug. Phonon-phonon interactions in transition metals. *Phys. Rev. B*, 84(9):094302, 2011.
- [118] Keivan Esfarjani and Harold T. Stokes. Method to extract anharmonic force constants from first principles calculations. *Phys. Rev. B*, 77(14):144112, 2008.
- [119] Duane C. Wallace. *Thermodynamics of Crystals*. Dover Publications, Mineola, New York, 1998.
- [120] A. Otero-de-la-Roza, David Abbasi-Piérrez, and Víctor Luaña. Gibbs2: A new version of the quasiharmonic model code. II. Models for solid-state thermodynamics, features and implementation. *Comput. Phys. Commun.*, 182(10):2232–2248, 2011.
- [121] Atsushi Togo, Laurent Chaput, Isao Tanaka, and Gilles Hug. First-principles phonon calculations of thermal expansion in Ti_3SiC_2 , Ti_3AlC_2 , and Ti_3GeC_2 . *Phys. Rev. B*, 81(17):174301, 2010.
- [122] M.A. Blanco, E. Francisco, and V. Luaña. GIBBS: isothermal-isobaric thermodynamics of solids from energy curves using a quasi-harmonic Debye model. *Comput. Phys. Commun.*, 158(1):57–72, 2004.
- [123] Yusuke Oba, Terumasa Tadano, Ryosuke Akashi, and Shinji Tsuneyuki. First-principles study of phonon anharmonicity and negative thermal expansion in ScF_3 . *Phys. Rev. Mater.*, 3(3):033601, 2019.

- [124] Wen Yu, Changqing Jin, and Axel Kohlmeyer. First principles calculation of phonon dispersion, thermodynamic properties and B 1-to- B 2 phase transition of lighter alkali hydrides. *Journal of Physics: Condensed Matter*, 19(8):086209, 2007.
- [125] Jianjun Xie, Stefano de Gironcoli, Stefano Baroni, and Matthias Scheffler. First-principles calculation of the thermal properties of silver. *Phys. Rev. B*, 59(2):965–969, January 1999.
- [126] Nicolas Mounet and Nicola Marzari. First-principles determination of the structural, vibrational and thermodynamic properties of diamond, graphite, and derivatives. *Physical Review B*, 71(20):205214, May 2005.
- [127] Tran Doan Huan, Vinit Sharma, George A. Rossetti, and Rampi Ramprasad. Pathways Towards Ferroelectricity in Hafnia. *Phys. Rev. B*, 90(6):064111, 2014.
- [128] Bao-Tian Wang, Ping Zhang, Raquel Lizárraga, Igor Di Marco, and Olle Eriksson. Phonon spectrum, thermodynamic properties, and pressure-temperature phase diagram of uranium dioxide. *Phys. Rev. B*, 88(10):104107, 2013.
- [129] Zhi Deng, Zhenbin Wang, Iek-Heng Chu, Jian Luo, and Shyue Ping Ong. Elastic Properties of Alkali Superionic Conductor Electrolytes from First Principles Calculations. *J. Electrochem. Soc.*, 163(2):A67–A74, 2016.
- [130] S. G. Jabarov, D. P. Kozlenko, S. E. Kichanov, A. V. Belushkin, A. I. Mammadov, B. N. Savenko, R. Z. Mekhtieva, and C. Lathe. Structural studies of the P-T phase diagram of sodium niobate. *J. Surf. Invest. X-ray*, 6(3):546–551, 2012.
- [131] M. Ahtee, A. M. Glazer, and H. D. Megaw. The structures of sodium niobate between 480 °C and 575 °C, and their relevance to soft-phonon modes. *Philos. Mag.*, 26(4):995–1014, 1972.
- [132] A. M. Glazer and Helen D. Megaw. The structure of sodium niobate (T2) at 600 °C, and the cubic-tetragonal transition in relation to soft-phonon modes. *Philos. Mag.*, 25(5):1119–1135, 1972.
- [133] Raquel Lizárraga, Fan Pan, Lars Bergqvist, Erik Holmstroim, Zsolt Gercsi, and Levente Vitos. First Principles Theory of the hcp-fcc Phase Transition in Cobalt. *Sci. Rep.*, 7(1):3778, 2017.
- [134] W. Kohn and L. J. Sham. Self-consistent equations including exchange and correlation effects. *Phys. Rev.*, 140(4A):A1133–A1138, 1965.

- [135] R. Car and M. Parrinello. Unified approach for molecular dynamics and density-functional theory. *Phys. Rev. Lett.*, 55:2471–2474, 1985.
- [136] Carlo Massobrio, Assil Bouzid, Mauro Boero, Guido Ori, Évelyne Martin, and Sébastien Le Roux. Chalcogenide glasses for innovation in applied science: fundamental issues and new insights. *J. Phys. D Appl. Phys.*, 53(3):033002, 2019.
- [137] Guido Ori, Assil Bouzid, Évelyne Martin, Carlo Massobrio, Sébastien Le Roux, and Mauro Boero. Chalcogenide glasses as a playground for the application of first-principles molecular dynamics to disordered materials. *Solid State Sci.*, 95:105925, 2019.
- [138] M Born and Oppenheimer R. Zur quantentheorie der molekeln. *Annalen der Physik*, IV. Folge:457–484, 1927.
- [139] William G. Hoover. Canonical dynamics: Equilibrium phase-space distributions. *Phys. Rev. A*, 31:1695–1697, 1985.
- [140] N. R. Werthamer. Self-consistent phonon formulation of anharmonic lattice dynamics. *Phys. Rev. B*, 1(2):572–581, 1970.
- [141] C. Y. Fong, J. E. Pask, and L. H. Yang. *Half-metallic Materials and Their Properties*. World Scientific, 2013.
- [142] Jeffrey C. Grossman, Lubos Mitas, and Krishnan Raghavachari. Structure and Stability of Molecular Carbon: Importance of Electron Correlation. *Phys. Rev. Lett.*, 75(21):3870–3873, November 1995.
- [143] S. Baroni, S. de Gironcoli, A. Dal Corso, and P. Giannozzi. Phonons and related properties of extended systems from density-functional perturbation theory. *Rev. Mod. Phys.*, 73(2):515–562, July 2001.
- [144] Yi Wang, Shunli Shang, Zi-Kui Liu, and Long-Qing Chen. Mixed-space approach for calculation of vibration-induced dipole-dipole interactions. *Phys. Rev. B*, 85(22):224303, June 2012.
- [145] Zhen-Long Lv, Hong-Ling Cui, Hui Wang, Xiao-Hong Li, and Guang-Fu Ji. Electronic, elastic, lattice dynamic and thermal conductivity properties of Na₃OBr via first principles. *Phys. Status Solidi B*, 254:1700089, May 2017.

- [146] J. Ramanna, N. Yedukondalu, K. Ramesh Babu, and G. Vaitheeswaran. Ab initio study of electronic structure, elastic and optical properties of anti-perovskite type alkali metal oxyhalides. *Solid State Sci.*, 20:120–126, June 2013.
- [147] M. A. Carpenter and C. J. Howard. Symmetry rules and strain/order-parameter relationships for coupling between octahedral tilting and cooperative Jahn-Teller transitions in ABX₃ perovskites. I. Theory. *Acta Crystallographica Section B: Structural Science*, 65(2):134–146, April 2009.
- [148] Bo Li, Angelos Michaelides, and Matthias Scheffler. Density functional theory study of flat and stepped NaCl(001). *Phys. Rev. B*, 76(7):075401, August 2007.
- [149] R. D. Shannon. Revised effective ionic radii and systematic studies of interatomic distances in halides and chalcogenides. *Acta Crystallogr. A*, 32(5):751–767, September 1976.
- [150] Mats Johansson and Peter Lemmens. Crystallography and Chemistry of Perovskites. In *Handbook of Magnetism and Advanced Magnetic Materials*. American Cancer Society, 2007.
- [151] Raouia Ben Sadok, Dalila Hammouténe, and Neculai Plugaru. New Phase Transitions Driven by Soft Phonon Modes for CsPbBr₃: Density Functional Theory Study. *Phys. Status Solidi (B)*, 258(2):2000289, 2021.
- [152] T. Tadano, Y. Gohda, and S. Tsuneyuki. Anharmonic force constants extracted from first-principles molecular dynamics: applications to heat transfer simulations. *J. Phys. Condens. Matter*, 26(22):225402, 2014.
- [153] John P. Perdew, Adrienn Ruzsinszky, Gábor I. Csonka, Oleg A. Vydrov, Gustavo E. Scuseria, Lucian A. Constantin, Xiaolan Zhou, and Kieron Burke. Restoring the density-gradient expansion for exchange in solids and surfaces. *Phys. Rev. Lett.*, 100:136406, 2008.
- [154] Jochen Heyd and Gustavo E. Scuseria. Efficient hybrid density functional calculations in solids: Assessment of the Heyd-Scuseria-Ernzerhof screened Coulomb hybrid functional. *J. Chem. Phys.*, 121(3):1187–1192, July 2004.
- [155] Alexandra Emly, Emmanouil Kioupakis, and Anton Van der Ven. Phase Stability and Transport Mechanisms in Antiperovskite Li₃OCl and Li₃OBr Superionic Conductors. *Chem. Mater.*, 25(23):4663–4670, 2013.

- [156] Daniel Sheppard, Rye Terrell, and Graeme Henkelman. Optimization methods for finding minimum energy paths. *J. Chem. Phys.*, 128(13):134106, 2008.
- [157] Susumu Fujii, Shenghan Gao, Cédric Tassel, Tong Zhu, Thibault Broux, Koji Okada, Yuto Miyahara, Akihide Kuwabara, and Hiroshi Kageyama. Alkali-Rich Antiperovskite M₃FCh (M = Li, Na; Ch = S, Se, Te): The Role of Anions in Phase Stability and Ionic Transport. *J. Am. Chem. Soc.*, 143(28):10668–10675, 2021.
- [158] *See Supplemental Material at.*
- [159] Yonggang Wang, Qingfei Wang, Zhenpu Liu, Zhengyang Zhou, Shuai Li, Jinlong Zhu, Ruqiang Zou, Yingxia Wang, Jianhua Lin, and Yusheng Zhao. Structural manipulation approaches towards enhanced sodium ionic conductivity in Na-rich antiperovskites. *J. Power Sources*, 293:735–740, October 2015.
- [160] J.Dawson, T. Famprakis, and K.E.Johnston. Anti-perovskites for solid-state batteries: recent developments, current challenges and future prospects. *J. Mater. Chem.*, 9:18746–18772, 2021.
- [161] Wei Xia, Zhao Yang, Zhao Feipeng, Adair Keegan, Zhao Ruo, Li Shuai, Zou Ruqiang, Zhao Yusheng, and Sun Xueliang. Antiperovskite electrolytes for solid-state batteries. *Chem. Rev.*, 122:3763–3819, 2022.
- [162] T. Shao, C. Liu, W. Deng, C. Li, X. Wang, M. Xue, and R. Li. Recent research on strategies to improve ion conduction in alkali metal ion batteries. *Batteries and Supercaps*, 2(5):403–427, 2019.
- [163] K. Kim, Y. Li, P.C. Tsai, F. Wang, S.B. Son, Y.M. Chiang, and D.J. Siegel. Exploring the synthesis of alkali metal anti-perovskites. *Chem. Mater.*, 34(3):947–958, 2022.
- [164] K. Yang, D. Liu, Z. Qian, D. Jiang, and R. Wang. Computational auxiliary for the progress of sodium-ion solid-state electrolytes. *ACS Nano*, 15(11):17232–17246, 2021.
- [165] Yusheng Zhao and Luke L. Daemen. Superionic Conductivity in Lithium-Rich Anti-Perovskites. *J. Am. Chem. Soc.*, 134(36):15042–15047, September 2012.
- [166] B.A. Goldmann, M.J. Clarke, J.A. Dawson, and M.S. Islam. Atomic-scale investigation of cation doping and defect clustering in the anti-perovskite Na₃OCl sodium-ion conductor. *J. Mater. Chem. A*, 10:2249–2255, 2022.
- [167] H. Fang and P. Jena. Li-rich antiperovskite superionic conductors based on cluster ions. *Proc. Natl. Acad. Sci. U.S.A.*, 114:11046–11051, 2017.

- [168] Zhi Deng, Dixing Ni, Diancheng Chen, Ying Bian, Shuai Li, Zhaoxiang Wang, and Yusheng Zhao. Anti-perovskite materials for energy storage batteries. *InfoMat*, 4:2567–3165, 2022.
- [169] Wang Yonggang, Qingfei Wang, Zhenpu Liu, Zhengyang Zhou, Shuai Li, Jinlong Zhu, Ruqiang Zou, Yingxia Wang, Jianhua Lin, and Yusheng Zhao. Structural manipulation approaches towards enhanced sodium ionic conductivity in na-rich antiperovskites. *J. Power Sources*, 293:735–740, 2015.
- [170] J.A.S. Oh, L. He, B. Chua, K. Zeng, and L. Lu. Inorganic sodium solid-state electrolyte and interface with sodium metal for room-temperature metal solid-state batteries. *Energy Storage Materials*, 34:28–44, 2021.
- [171] J.A. Dawson, H. Chen, and M.S. Islam. Composition screening of lithium-and sodium-rich anti-perovskites for fast-conducting solid electrolytes. *J. Phys. Chem. C*, 122(42):23978–23984, 2020.
- [172] E. Ahiavi, J.A. Dawson, U. Kudu, M. Courty, M.S. Islam, O. Clemens, C. Masquelier, and T. Famprakis. Mechanochemical synthesis and ion transport properties of Na_3Ox ($x = \text{Cl}, \text{Br}, \text{I}$ and BH_4) antiperovskite solid electrolytes. *J. Power Sources*, 471:228489, 2020.
- [173] Xiaolong Xu, Kwan San Hui, Kwun Nam Hui, Hao Wang, and Jingbing Liu. Recent advances in the interface design of solid-state electrolytes for solid-state energy storage devices. *Mater. Horizons*, 7(5):1246–1278, 2020.
- [174] Tan-Lien Pham, Woon Ih Choi, Aamir Shafique, Hye Jung Kim, Munbo Shim, Kyoungmin Min, Won-Joon Son, Inkook Jang, Dae Sin Kim, Mauro Boero, Carlo Massobrio, Guido Ori, Hyo Sug Lee, and Young-Han Shin. Structural-Stability Study of Antiperovskite Na_3OCl for Na -Rich Solid Electrolyte. *Phys. Rev. App.*, 19(3):034004, March 2023.
- [175] S. Gao, C. Tassel, S. Fujii, H. Ubukata, T. Zhu, D. Zhang, T. Broux, T. Saito, C. Zhong, E. Yoruk, and K. Yamamoto. $\text{Na}_3\text{H}(\text{ZnH}_4)$ antiperovskite: A large octahedral distortion with an off-centering hydride anion coupled to molecular hydride. *Chem. Mater.*, 34(16):6815–6823, 2022.
- [176] Jingfeng Zheng, Brian Perry, and Yiyang Wu. Antiperovskite Superionic Conductors: A Critical Review. *ACS Mater. Au*, 1(2):92–106, November 2021.

- [177] M. H. Braga, N. S. Grundish, A. J. Murchison, and J. B. Goodenough. Alternative strategy for a safe rechargeable battery. *Energy & Environ. Sci.*, 10(1):331–336, January 2017.
- [178] M. H. Braga, J. A. Ferreira, V. Stockhausen, J. E. Oliveira, and A. El-Azab. Novel Li₃ClO based glasses with superionic properties for lithium batteries. *J. Mater. Chem. A*, 2(15):5470–5480, March 2014.
- [179] M. Helena Braga, Andrew J. Murchison, Jorge A. Ferreira, Preetam Singh, and John B. Goodenough. Glass-amorphous alkali-ion solid electrolytes and their performance in symmetrical cells. *Energy & Environ. Sci.*, 9(3):948–954, 2016.
- [180] M. Helena Braga, Jorge A. Ferreira, Andrew J. Murchison, and John B. Goodenough. Electric Dipoles and Ionic Conductivity in a Na⁺ Glass Electrolyte. *J. Electroch. Soc.*, 164(2):A207–A213, 2017.
- [181] Isabel Hanghofer, Gunther J. Redhammer, Sebastian Rohde, Ilie Hanzu, Anatoliy Senyshyn, H. Martin R. Wilkening, and Daniel Rettenwander. Untangling the Structure and Dynamics of Lithium-Rich Anti-Perovskites Envisaged as Solid Electrolytes for Batteries. *Chem. Mater.*, 30(22):8134–8144, November 2018.
- [182] Hendrik H. Heenen, Johannes Voss, Christoph Scheurer, Karsten Reuter, and Alan C. Luntz. Multi-ion Conduction in Li₃OCl Glass Electrolytes. *J. Phys. Chem. Lett.*, 10(9):2264–2269, May 2019.
- [183] Y. Tian, F. Ding, L. Sang, Y.B. He, X. Liu, and Q. Xu. Excellent lithium metal anode performance via in situ interfacial layer induced by li₆.₇₅la₃zr_{1.75}ta_{0.25}o₁₂ amorphous li₃ocl composite solid electrolyte. *Int. J. Electrochem. Sci*, 14:4781–4798, 2019.
- [184] Y. Gao, S. Sun, X. Zhang, Y. Liu, J. Hu, Z. Huang, M. Gao, and H. Pan. Amorphous dual layer coating: Enabling high li ion conductivity of non-sintered garnet type solid electrolyte. *Adv. Funct. Mater.*, 31(15):2009692, 2021.
- [185] Jeffrey G. Smith and Donald J. Siegel. Low-temperature paddlewheel effect in glassy solid electrolytes. *Nature Communications*, 11(1):1483, March 2020.
- [186] Wei Xia, Yang Zhao, Feipeng Zhao, Keegan Adair, Ruo Zhao, Shuai Li, Ruqiang Zou, Yusheng Zhao, and Xueliang Sun. Antiperovskite electrolytes for solid-state batteries. *Chem. Rev.*, 112(3):3763–3819, 2022.

- [187] R. Car and M. Parrinello. Unified Approach for Molecular Dynamics and Density-Functional Theory. *Phys. Rev. Lett.*, 55(22):2471–2474, November 1985.
- [188] J.P. Perdew, K. Burke, and M. Ernzerhof. Generalized gradient approximation made simple. *Phys. Rev. Lett.*, 77:3865, 1996.
- [189] N. Troullier and José Luís Martins. Efficient pseudopotentials for plane-wave calculations. *Phys. Rev. B*, 43(3):1993–2006, January 1991.
- [190] Shuichi Nosé. A molecular dynamics method for simulations in the canonical ensemble. *Mol. Phys.*, 52(2):255–268, June 1984.
- [191] Shuichi Nosé. A unified formulation of the constant temperature molecular dynamics methods. *J. Chem. Phys.*, 81(1):511–519, July 1984. Publisher: American Institute of Physics.
- [192] William G. Hoover. Canonical dynamics: Equilibrium phase-space distributions. *Phys. Rev. A*, 31(3):1695–1697, March 1985.
- [193] Glenn J. Martyna, Michael L. Klein, and Mark Tuckerman. Nosé-Hoover chains: The canonical ensemble via continuous dynamics. *J. Chem. Phys.*, 97(4):2635–2643, August 1992. Publisher: American Institute of Physics.
- [194] P.E. Blochl and M. Parrinello. Adiabaticity in first-principles molecular dynamics. *Phys. Rev. B*, 45(16):9413–9416, April 1992.
- [195] A. Bouzid, T.L. Pham, Z. Chaker, M. Boero, C. Massobrio, Y.H. Shin, and G. Ori. Quantitative assessment of the structure of ge 20 te 73 i 7 chalcogenide glass by first-principles molecular dynamics. *Phys. Rev. B*, 103(9):094204, 2021.
- [196] G. Ori, A. Bouzid, E. Martin, C. Massobrio, S. Le Roux, and M. Boero. Chalcogenide glasses as a playground for the application of first-principles molecular dynamics to disordered materials. *Solid State Sci.*, 95:105925, 2019.
- [197] G. Ori, C. Massobrio, A. Bouzid M. Boero, and B. Coasne. Surface of glassy ges 2: A model based on a first-principles approach. *Phys. Rev. B*, 90:045423, 2014.
- [198] Quentin Evrard, Zyaid Chaker, Roger M., Sevrain C.M., Emilie Delahaye, E. Gallart, M. Gilliot, P. C. Leuvrey, Rueff J.M., Rabu P., Mauro Boero, Carlo Massobrio, Guido Ori, and Guillaume Rogez. Layered simple hydroxides functionalized by fluorene phosphonic acids: Synthesis, interface theoretical insights, and magnetoelectric effect. *Adv. Funct. Mater.*, 27(41):1703576, 2017.

- [199] Z. Chaker, A. Bouzid, B. Coasne, C. Massobrio, M. Boero, and G. Ori. The structure and dipolar properties of CO_2 adsorbed in a porous glassy chalcogen: Insights from first-principles molecular dynamics. *J. Non-Cryst. Solids*, 498:288–293, 2018.
- [200] G. Cotin, C. Kiefer, F. Pertot, M. Boero, B. Ozdamar, A. Bouzid, G. Ori, C. Massobrio, D. Begin, B. Pichon, D. Mertz, and S. Begin-Colin. Evaluating the critical roles of precursor nature and water content when tailoring magnetic nanoparticles for specific applications. *ACS App. Nano Mater.*, 1(8):4306–4316, 2018.
- [201] Burak Ozdamar, Assil Bouzid, Guido Ori, Carlo Massobrio, and Mauro Boero. First-Principles Study of Dissociation Processes for the Synthesis of Fe and Co Oxide Nanoparticles. *Journal of Chemical Theory and Computation*, 14(1):225–235, January 2018.
- [202] D. Gentili and G. Ori. Reversible assembly of nanoparticles: theory, strategies and computational simulations. *Nanoscale*, pages 1–50, 2022.
- [203] K. Hippler, S. Sitta, P. Vogt, and H. Sabrowsky. Structure of Na_3OCl . *Acta Cryst.*, 463:736–738, 1990.
- [204] C. Massobrio, J. Du, M. Bernasconi, and P.S. Salmon, editors. *Molecular dynamics simulations of disordered materials*. Cham: Springer International Publishing, New York, 3 edition, 2015.
- [205] E.V. Levchenko, Y.J. Dappe, and G. Ori, editors. *Theory and Simulation in Physics for Materials Applications: Cutting-edge Techniques in Theoretical and Computational Materials Science*. Cham: Springer International Publishing, New York, 3 edition, 2020.
- [206] J. Habasaki. A molecular dynamics study of enhanced dynamics and self healing processes in nanoporous lithium metasilicate systems. *Int. J. Appl. Glass Sci.*, 11:421–431, 2020.
- [207] N.M. Vargas-Barbosa and B. Roling. Dynamic ion correlations in solid and liquid electrolytes: how do they affect charge and mass transport? *ChemElectroChem*, 7:367–385, 2020.
- [208] A.E. Gheribi, K. Machado, D. Zanghi, C. Bessada, M. Salanne, and P. P. Chartrand. On the determination of ion transport numbers in molten salts using molecular dynamics. *Electrochim. Acta*, 274:266–273, 2018.

- [209] H. Fanf and P. Jena. Argyrodite-type advanced lithium conductors and transport mechanisms beyond paddle-wheel effect. *Nature Commun.*, 13:2078, 2022.
- [210] D. Frenkel and B. Smit. *Understanding Molecular Simulation, From Algorithms to Applications*. Computational Science, From Theory to Applications (Academic), New York, 2nd ed. edition, 2001.
- [211] M. Allen and D. J. Tildesley. *Computer Simulation of Liquids*. Oxford University Press, USA, New York, 1989.
- [212] A. Van der Ven, G. Ceder, M. Asta, and P.D. Tepesch. First-principles theory of ionic diffusion with nondilute carriers. *Phys. Rev. B*, 64:184307, 2001.
- [213] L. Haarmann and K. Albe. From ionic to superionic conductivity: The influence of cation order on sodium diffusion in $\text{Na}_3\text{Zr}_2\text{Si}_2\text{P}_2\text{O}_{12}$. *Solid State Ion.*, 363:115604, 2021.
- [214] S. Sicolo, C. Kalcher, S.J. Sedlmaier, J. Janek, and K. Albe. Diffusion mechanism in the superionic conductor $\text{Li}_4\text{PS}_4\text{I}$ studied by first-principles calculations. *Solid State Ion.*, 319:83–91, 2018.
- [215] Y. Gao, A.M. Nolan, P. Du, Y. Wun, C. Yang, Q. Chen, Y. Mo, and S.H. Bo. Classical and emerging characterization techniques for investigation of ion transport mechanisms in crystalline fast ionic conductors. *Chem. Rev.*, 120:5954–6008, 2020.
- [216] G.E. Murch. The haven ratio in fast ionic conductors. *Solid State Ion.*, 7:177–198, 1982.
- [217] W.D. Richards, T. Tsujimura, L.J. Miara, Y. Wang, J.C. Kim, S.P. Ong, I. Uechi, N. Suzuki, and G. Ceder. Design and synthesis of the superionic conductor $\text{Na}_{10}\text{SnP}_2\text{S}_{11}$. *Nature. Commun.*, 7(1):1–8, 2016.
- [218] Z. Zhu, I.H. Chu, Z. Deng, and S.P. Ong. Role of Na^+ interstitials and dopants in enhancing the Na^+ conductivity of the cubic Na_3PS_4 superionic conductor. *Chem. Mater.*, 27(24):8318–8325, 2015.
- [219] Y.Y. Lin, A.X.B. Yong, W.J. Gustafson, C.N. Reedy, E. Ertekin, J.A. Krogstad, and N.H. Perry. Toward design of cation transport in solid-state battery electrolytes: structure-dynamics relationships. *Curr. Opin. Solid State Mater. Sci.*, 24:100875, 2020.
- [220] A. Marcolongo and N. Marzari. Ionic correlations and failure of nernst-einstein relation in solid-state electrolytes. *Phys. Rev. Mater.*, 1:025402, 2017.

- [221] N. Molinari, Y. Xie, I. Leifer, A. Marcolongo, M. Kornblutha, and B. Kozinsky. Spectral denoising for accelerated analysis of correlated ionic transport. *Phys. Rev Lett.*, 217:025901, 2021.
- [222] M. Mottet, A. Marcolongo, T. Laino, and I. Tavernelli. Doping in garnet-type electrolytes: Kinetic and thermodynamic effects from molecular dynamics simulations. *Phys. Rev. Mater.*, 3:035403, 2019.
- [223] P.S. Salmon and A. Zeidler. Networks under pressure: the development of in situ high-pressure neutron diffraction for glassy and liquid materials. *J. Condens. Matter Phys.*, 27(13):133201, 2015.
- [224] A. Zeidler, P.S. Salmon, T. Usuki, S. Kohara, H.E. Fischer, and M. Wilson. Structure of molten nacl and the decay of the pair-correlations. *J. Chem. Phys.*, 157:094504, 2022.
- [225] T.L. Pham, A. Samad, H.J. Kim, and Y.H. Shin. Computational predictions of stable phase for antiperovskite na₃ocl via tilting of na₆o octahedra. *J. App. Phys.*, 124(16):164106, 2018.
- [226] Dominik Marx. Proton transfer 200 years after von grotthuss: Insights from ab initio simulations. *ChemPhysChem*, 7(9):1848–1870, 2006.
- [227] Mark Tuckerman, Dominik Marx, and Michele Parrinello. The nature and transport mechanism of hydrated hydroxide ions in aqueous solution. *Nature*, 417(6892):925–929, 2002.
- [228] Mauro Boero, Tamio Ikeshoji, and Kiyoyuki Terakura. Density and temperature dependence of proton diffusion in water: A first principles molecular dynamics study. *ChemPhysChem*, 6(9):1775–1779, 2005.
- [229] Katsumasa Kamiya, Mauro Boero, Masaru Tateno, Kenji Shiraishi, and Atsushi Oshiyama. Possible mechanism of proton transfer through peptide groups in the h-pathway of the bovine cytochrome c oxidase. *J. Amer. Chem. Soc.*, 129(31):9663–9673, 2007.
- [230] Hassanali Ali, Federico Giberti, Jérôme Cuny, Thomas D. Kuhne, and Michele Parrinello. Proton transfer through the water gossamer. *Proc. Natl. Acad. Sci. U.S.A.*, 110(34):13723–13728, 2013.
- [231] Matt Hellstrom, Michele Ceriotti, and Jorg Behler. Nuclear quantum effects in sodium hydroxide solutions from neural network molecular dynamics simulations. *J. Phys. Chem. B*, 122(44):10158–10171, 2018.

- [232] Ziheng Lu, Chi Chen, Zarah Medina Baiyee, Xin Chen, Chunming Niu, and Francesco Ciucci. Defect chemistry and lithium transport in Li_3OCl anti-perovskite superionic conductors. *Physical Chemistry Chemical Physics*, 17(48):32547–32555, 2015.
- [233] Xujie Lu, John W. Howard, Aiping Chen, Jinlong Zhu, Shuai Li, Gang Wu, Paul Dowden, Hongwu Xu, Yusheng Zhao, and Quanxi Jia. Antiperovskite Li_3OCl Superionic Conductor Films for Solid-State Li-Ion Batteries. *Advanced Science*, 3(3):n/a–n/a, March 2016.
- [234] J.A.S. Serejo, J.S. Pereira, R. Mouta, and L.G.C. Rego. Sluggish anion transport provides good kinetic stability to the anhydrous anti-perovskite solid electrolyte Li_3OCl . *Phys. Chem. Chem. Phys.*, 23(11):6964–6973, 2021.
- [235] A.Y. Song, Y. Xiao, K. Turcheniuk, P. Upadhyay, A. Ramanujapuram, J. Benson, A. Magasinski, M. Olguin, L. Meda, O. Borodin, and G. Yushin. Protons enhance conductivities in lithium halide hydroxide/lithium oxyhalide solid electrolytes by forming rotating hydroxy groups. *Adv. Energy Mater.*, 8:1700971, 2018.
- [236] J. Howard, Z.D. Hood, and N.A.W. Holzwarth. Fundamental aspects of the structural and electrolyte properties of $\text{Li}_2\text{O}(\text{HCl})$ from simulations and experiment. *Phys. Rev. Mater.*, 1:075406, 2017.
- [237] Ping-Chun Tsai, Sunil Mair, Jeffrey Smith, David M. Halat, Po-Hsiu Chien, Kwangnam Kim, Duhan Zhang, Yiliang Li, Liang Yin, Jue Liu, Saul H. Lapidus, Jeffrey A. Reimer, Nitash P. Balsara, Donald J. Siegel, and Yet-Ming Chiang. Double Paddle-Wheel Enhanced Sodium Ion Conduction in an Antiperovskite Solid Electrolyte. *Advanced Energy Materials*, 13(7):2203284, 2023.
- [238] Hong Fang and Puru Jena. Argyrodite-type advanced lithium conductors and transport mechanisms beyond paddle-wheel effect. *Nature Communications*, 13(1):2078, April 2022.
- [239] F.H. Fu, X. Chen, N. Yao, X. Shen, X.X. Ma, S. Feng, S. Wang, R. Zhang, L. Zhang, and Q. Zhang. The chemical origin of temperature-dependent lithium-ion concerted diffusion in sulfide solid electrolyte $\text{Li}_{10}\text{GeP}_2\text{S}_{12}$. *J. Energy Chem.*, 70:59–66, 2022.
- [240] Z. Zhang and L.F. Nazar. Exploiting the paddle-wheel mechanism for the design of fast ion conductors. *Nature Rev. Mater.*, 7:389–405, 2022.

- [241] J. Habasaki, editor. *Molecular Dynamics of Nanostructures and Nanoionics, Simulations in Complex Systems*. eBook, Imprint Jenny Stanford Publishing; New York., 2020.
- [242] Margit Fabian, Istvan Tolnai, Atul Khanna, Zsolt Endre Horvath, Viktoria Kovacs Kis, and Zsolt Kovacs. Structural Characterization of Oxyhalide Materials for Solid-State Batteries. *Phys. Status Solidi A*, 218(17):2000682, 2021.
- [243] Atsuto Seko, Akira Takahashi, and Isao Tanaka. Sparse representation for a potential energy surface. *Physical Review B*, 90(2):024101, July 2014.
- [244] Chi Chen, Zhi Deng, Richard Tran, Hanmei Tang, Iek-Heng Chu, and Shyue Ping Ong. Accurate force field for molybdenum by machine learning large materials data. *Physical Review Materials*, 1(4):043603, September 2017.
- [245] Daniele Dragoni, Thomas D. Daff, Gábor Csányi, and Nicola Marzari. Achieving DFT accuracy with a machine-learning interatomic potential: Thermomechanics and defects in bcc ferromagnetic iron. *Physical Review Materials*, 2(1):013808, January 2018.
- [246] Albert P. Bartók, Risi Kondor, and Gábor Csányi. On representing chemical environments. *Physical Review B*, 87(18), May 2013.
- [247] Wojciech J. Szlachta, Albert P. Bartók, and Gábor Csányi. Accuracy and transferability of Gaussian approximation potential models for tungsten. *Physical Review B*, 90(10):104108, September 2014.
- [248] Albert P. Bartók, James Kermode, Noam Bernstein, and Gábor Csányi. Machine Learning a General-Purpose Interatomic Potential for Silicon. *Physical Review X*, 8(4):041048, December 2018.
- [249] Volker L. Deringer and Gábor Csányi. Machine learning based interatomic potential for amorphous carbon. *Physical Review B*, 95(9), March 2017.
- [250] Patrick Rowe, Volker L. Deringer, Piero Gasparotto, Gábor Csányi, and Angelos Michaelides. An accurate and transferable machine learning potential for carbon. *The Journal of Chemical Physics*, 153(3):034702, July 2020.
- [251] Steve Plimpton. Fast Parallel Algorithms for Short-Range Molecular Dynamics. *Journal of Computational Physics*, 117(1):1–19, March 1995.

- [252] Albert P. Bartók, Mike C. Payne, Risi Kondor, and Gábor Csányi. Gaussian Approximation Potentials: The Accuracy of Quantum Mechanics, without the Electrons. *Phys. Rev. Lett.*, 104(13), April 2010.
- [253] Wojciech J. Szlachta, Albert P. Bartók, and Gábor Csányi. Accuracy and transferability of Gaussian approximation potential models for tungsten. *Phys. Rev. B*, 90(10):104108, September 2014. Publisher: American Physical Society.
- [254] Albert P. Bartók and Gábor Csányi. Gaussian approximation potentials: A brief tutorial introduction. *Int. J. Quantum Chem.*, 115(16):1051–1057, 2015.
- [255] Felix C. Mocanu, Konstantinos Konstantinou, Tae Hoon Lee, Noam Bernstein, Volker L. Deringer, Gábor Csányi, and Stephen R. Elliott. Modeling the Phase-Change Memory Material, Ge₂Sb₂Te₅, with a Machine-Learned Interatomic Potential. *The Journal of Physical Chemistry B*, 122(38):8998–9006, September 2018.
- [256] Davis Unruh, Reza Vatan Meidanshahi, Stephen M. Goodnick, Gábor Csányi, and Gergely T. Zimányi. Gaussian approximation potential for amorphous Si : H. *Physical Review Materials*, 6(6):065603, June 2022.
- [257] Michael W. Mahoney and Petros Drineas. CUR matrix decompositions for improved data analysis. *Proceedings of the National Academy of Sciences*, 106(3):697–702, January 2009.
- [258] So Fujikake, Volker L. Deringer, Tae Hoon Lee, Marcin Krynski, Stephen R. Elliott, and Gábor Csányi. Gaussian approximation potential modeling of lithium intercalation in carbon nanostructures. *The Journal of Chemical Physics*, 148(24):241714, June 2018.

List of publications

1. **Tan-Lien Pham**, Abdus Samad, Hye Jung Kim, and Young-Han Shin, “Computational predictions of stable phase for antiperovskite Na_3OCl via tilting of Na_6O octahedra”, *Journal of Applied Physics*, **124** (2018) 1641066.
2. Assil Bouzid, **Tan-Lien Pham**, Ziyad Chaker, Mauro Boero, Carlo Massobrio, Young-Han Shin, and Guido Ori, “Quantitative assessment of the structure of $\text{Ge}_{20}\text{Te}_{73}\text{I}_7$ chalcogenide glass by first-principles molecular dynamics”, *Physical Review B*, **103** (2021) 094204.
3. **Tan-Lien Pham**, Woon Ih Choi, Aamir Shafique, Hye Jung Kim, Munbo Shim, Kyoungmin Min, Won-Joon Son, Inkook Jang, Dae Sin Kim, Mauro Boero, Carlo Massobrio, Guido Ori, Hyo Sug Lee, and Young-Han Shin, “Structural-Stability Study of Antiperovskite Na_3OCl for Na-Rich Solid Electrolyte”, *Physical Review Applied*, **19** (2023) 034004.
4. **Tan-Lien Pham**, Assil Bouzid, Mauro Boero, Carlo Massobrio, Young-Han Shin, and Guido Ori, “Unveiling the structure and ions dynamics of amorphous $\text{Na}_{3-x}\text{OH}_x\text{Cl}$ antiperovskite electrolytes by first-principles molecular dynamics”, under review.